



Master Thesis

submitted within the UNIGIS MSc programme
Interfaculty Department of Geoinformatics - Z_GIS
University of Salzburg

Variability and abrupt change events Analysing forest fires with the LIVID approach

by

Marc Schmitz MSc
105167, UNIGIS 2018

A thesis submitted in partial fulfilment of the requirements of
the degree of
Master of Science (Geographical Information Science & Systems) – MSc (GIS)

Advisors:

Assoc. Prof. Dirk Tiede, Martin Sudmanns, Hannah Augustin

Luxembourg, 23.07.2020

Master's thesis statement of originality

I hereby declare on oath [through my personal signature], that I independently composed the present work and that no other sources or auxiliary means than the stated ones were used. All paragraphs, that were adopted word-by-word or with regards to content, are distinguishable as such.

The present work was not yet submitted in equal or similar form as a bachelor's thesis/master's thesis/diploma thesis/dissertation.

Luxembourg, 23.07.2020

X

Marc Schmitz

Abstract

This thesis uses a time-series variability framework, more specifically the “Long Image Time-Series Variability Indicator Description” (short: LIVID) approach, to analyse an abrupt change event, in the form of a forest fire, which occurred in Spain in 2017. Before said case-study was conducted, a pre-existing application of the approach within eCognition was further developed and the capability of calculating spectral indices (NDVI and NBR) was added. The results of the LIVID approach and the other indices showed at first a similarity in index values per time point, but a difference in variability results: while the variability values of the LIVID approach were influenced by seasonality showing higher numbers in the areas unaffected by the fires, the other indices had the highest variability values in the damaged areas in which the one-time change event occurred. The LIVID approach does therefore not constitute a substitution for other spectral indices, but rather a further, highly customizable instrument in the world of remote sensing.

Table of Contents

1	Introduction	5
2	Research Questions	6
2.1	State of the art	6
3	Methodology	8
3.1	Object-based image analysis (OBIA) and Object-based change detection (OBCD)	8
3.2	eCognition	10
3.3	Long Image Time-Series Variability Indicator Description (LIVID) approach	12
3.3.1	Variability	13
3.3.2	The LIVID application	15
3.3.3	Implemented features	19
3.3.4	NDVI and NBR calculation	23
4	Case Study: Forest Fires in the Huelva Province, Andalusia, Spain (2017)	27
4.1	Results of EMSN-060	29
4.2	Data	30
4.3	Applying the LIVID approach	33
4.4	Variability	43
4.4.1	Processes behind the differing variability distribution of the indices	54
5	Discussion	61
5.1	Implemented features	61
5.2	Test-run of the LIVID application	62
6	Conclusion	65
7	Sources	67
8	Table of figures	69
	Appendix I – SIAM Classes	72
	Appendix II – Statistical Evaluation of NRI, NDVI and NBR	73

1 Introduction

Vegetation and other natural resources are not excluded from large-scale planetary change processes. Evermore sophisticated tools are getting developed in the nexus of remote sensing, to better reflect these temporal differences. In this thesis, such a framework, namely the “Long Image Time-Series Variability Indicator Description” (short: LIVID), is applied to an abrupt-change event, more precisely on forest fires. Through climate change and rising temperature levels, more - often man-made - forest fires occur every year with devastating consequences on the human, plant, and animal life. The main objectives are to see the results produced from the LIVID approach when handling this type of event and to develop it further for future projects.

The fires analysed in this work, took place in the year 2017, in the province of Huelva in West-Andalusia, Spain. Over 6 timesteps, and with the help of SIAM pre-classified “Sentinel-2” imagery, the aftermath of the fires will be investigated. Therefore, the areas under investigation are first divided into equal reporting units. Second, the area-wise composition by landcover classes, distinct by their assigned weights, determine the index value of an individual unit per timestep. Third, the variability of every reporting unit is calculated, with not only including the index difference between the first and the last but also of the timesteps in between into the calculation.

The goal of the thesis is to see how the approach handles such an incident, while further enhancing a pre-existing application of the LIVID approach, which was realised in eCognition. Thus, the present work has a two-sided character: the LIVID approach's application is in a first step enhanced, to be prepared to, in a second step, be applied to a specific case study. This character is also reflected in the structure of the thesis, in which first the technical improvements of the application are showcased and discussed, before going over to the case study itself.

The chapter order is as well oriented on this division: the next chapter showcases the two research questions analysed in this thesis, followed by a short review of the state of the art of the general topic. The third chapter focuses on the methodological background of the thesis. It therefore firstly gives an overview of the topics of object-based image analysis (OBIA) and object-based change detection (OBCD), before introducing eCognition, the software mainly utilized in this work. Secondly, the LIVID approach and the concepts behind it, namely the natural resource indicator and variability, are explained. Then the existing application of the LIVID approach inside of eCognition is presented, together with new features implemented throughout the thesis. The fourth chapter eventually centers around the case study involving forest fires, on which the revised LIVID application is tested. Finally, the thesis is rounded off with a discussion of the case study's results and an overall conclusion of the work.

2 Research Questions

The focus of this work was to analyse how the LIVID approach handles abrupt change events. The change events analysed in this study consisted of two forest fires in Western Andalusia, Spain, which occurred nearby to each other and in the same time frame in 2017. A second objective was to develop the already existing LIVID application, established in eCognition, to analyse the event more accurately.

1. Which functions can be added to the LIVID application to enhance its capability of analysing abrupt change events, such as a forest fire?
2. What results yields the LIVID approach (NRI, variability) on abrupt change events like a forest fire? How does the LIVID approach handle such abrupt change events in comparison to established indicators like NDVI and NBR?

As observable in the research questions, this work was divided into two main parts. The first part had a technical setting and centered around adjustments to an existing object-based approach (LIVID) and the algorithms behind it, generated in eCognition. These alterations aimed to enhance the application's usability and its results, when analysing a forest fire. The additional value of these changes was then to be tested in the second part. The focus lied first on programming and application development.

In the second part, the revised application was then put to test on a specific case study. The results taken from this experiment were further compared to results from established change detection frameworks and an earlier report on the event. The goal of this step was to see if the results from the application were plausible. If problems with the application and its handling of this specific case are discovered, the processes behind them were analysed thoroughly and suggestions for further adjustments were made.

2.1 State of the art

Change detection (CD) of remotely sensed data has been widely discussed in the literature. In 1989, Singh published his review article on the subject. CD was here described as “the process of identifying differences in the state of an object or phenomenon by observing it at different times” (Singh, 1989, p. 989). A more recent review article on CD techniques by Hussain et al. tackled the divide between pixel-based and object-based techniques. The difference in these techniques lies in their fundamental unit of analysis: pixel or object. Hussain et al. further gave an in-depth insight into different techniques of both sides, stating not only disadvantages and advantages for every technique but also case studies (Hussain et al., 2013). A more detailed look at the approach of having an object as a fundamental unit of analysis, also known as object-based image analysis (OBIA), was taken by Blaschke. The focus of the article laid on the quantification of the emergence of the topic of OBIA in the scientific literature (Blaschke, 2010).

An OBIA study with a similar approach as the one presented in this thesis is followed by Hagenlocher et al. when analysing the environmental impact of an IDP (internally displaced person) camp in Sudan. They developed an index in the form of the “Weighted Natural Resource index” (NRD_W). The study area was divided into grid cells and the indicator was calculated for every cell, based on weights relating to human security and/or ecosystem integrity, for three timesteps. (Hagenlocher et al., 2012). The same framework was applied by Braun and Hochschild when they studied landscape changes in African savannas. After calculating the NRD_W for the grid cells overlaying their study area in Chad for 8 timesteps, they began calculating the so-called variability of each cell. The variability was calculated by dividing the sum of the changes between every pair of consecutive images, by the overall change between the first and the last timestep. This approach incorporates not only the overall change in the area but also the inter-image change between the different timesteps and therefore gave a more inclusive overview of the changes in the areas of interest (Braun and Hochschild, 2017).

3 Methodology

The following chapter focuses on the methodological assumptions surrounding this work. As deducible from the research questions in chapter 2, change detection (CD) was one of the key points of this master's thesis. Several images, of different dates in time, of the same area were compared to detect the changes between them and subsequently to quantify them. The object-based CD approach was applied for this, which will be further discussed in the following subchapter.

Thereafter, the more technical side of this work is covered, with an introduction of the software used in this work, eCognition Developer. The applied functionalities of the software are then briefly detailed. The time series variability method and the concepts behind it, are explained after this. An existing application of the LIVID approach within eCognition which was designed by the supervisor team is also showcased following this theoretical background. Finally, new features that were added to this application throughout this master's thesis as a contribution to the approach are illustrated.

3.1 Object-based image analysis (OBIA) and Object-based change detection (OBCD)

The framework applied in this work can be placed in the fields of object-based image analysis (OBIA) and object-based change detection (OBCD). These can themselves be grouped under the larger field of remote sensing (RS). Other groups of change detection techniques are referred to as pixel-based change detection (PBCD) or spatial data mining (Hussain et al., 2013). A short introduction into the world of object-based techniques is therefore given at this point.

As the name suggests, OBIA is part of the image analysis techniques, which can use very-high-resolution (VHR) satellite imagery as base data. This imagery is composed of equally sized pixels, while the dimension of these pixels is depending on the imaging device. A pixel itself is a representation of the spectral profile of the area it covers. Besides OBIA, the most common framework for image analysis is, therefore, the pixel-based approach in which the pixel acts as the fundamental unit of analysis.

Yet, when basing an analysis on pixels as units, one must recognize that these are not geographical objects. OBIA itself emerged out of this critique: instead of single pixels, groups of them are analysed together, as objects, having a specific spatial context. Features existing in the real world are represented through these objects. Properties like shape, texture, and the relationships between the individual objects are important for the analysis of such imagery. Further, when analysing objects, one can calculate statistical indicators based on their spectral profiles (mean, median, quantile, etc.) to visualize or process them (Hussain et al., 2013). It is, however, also possible, to define objects as equally sized units, which divide an area into specific shapes (squares, hexagons), and which are then analysed further, as we will see in the LIVID subchapter. In the following paragraph, the OBIA process and its steps will be discussed.

To create the objects, an image must first undergo segmentation. The resulting segments can be described as areas, having a certain degree of homogeneity in one or more aspects. As a grouping of pixels, the segments or objects offer more spectral information (such as mean, median, maximum, and minimum values per band) than single pixels (Hussain et al., 2013). A piece of even more important information is, however, the already mentioned spatial context of the objects: many relations like distance, neighbourhood or topologies can be deduced from this. Four different types of algorithms for image segmentation exist: point-based, edge-based, region-based, and combined (Blaschke, 2010).

To make the concept more tangible, an example of a segmented image is presented in Figure 1. This example was generated in “eCognition Developer”, an OBIA software which will be introduced in chapter 3.2. It shows an agricultural area, in which the different fields are portioned into objects, based on the spectral profile of the pixels they consist of. A “multiresolution segmentation” algorithm was utilized, without further processing, explaining why some of the similar objects were not merged. A so-called “chessboard segmentation” would have resulted in a parcelling of the area into equally sized squares, without considering any spectral properties of the area.

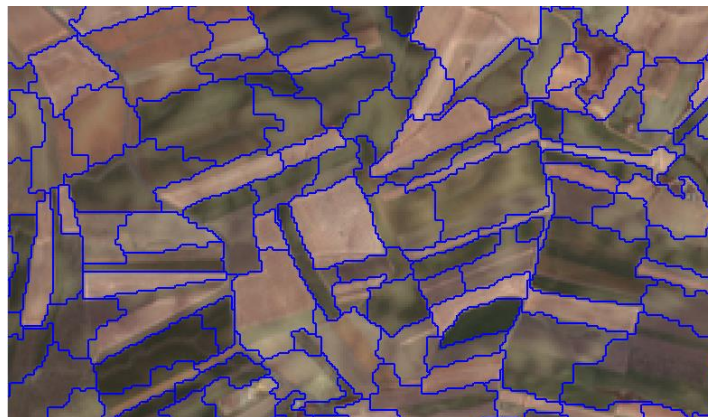


Figure 1: Segmentation of agricultural land in Andalusia, Spain (eCognition, contains Copernicus Sentinel data 2017)

After the segmentation, an object hierarchy is developed. This hierarchy is a grouping of objects on different levels. A comprehensive example is given in the “eCognition Developer User Guide”: the topmost level, in this case, “forest” (coarse), serves as a super-level to a second level, in this case, “tree type” (medium), which again has a sub-level, which is, in this case, “tree” (fine). More broadly speaking, we see a hierarchical relationship between the levels: topmost level is the forest, consisting of different tree types on a second level, which is then itself consisting of individual trees represented on a third level (Trimble, 2017).

Finally, the objects, or segments, can be classified into different categories. These results can then further be processed through OBCD. Different OBCD techniques can be found in the literature; direct object change detection (DOCD, extracting objects from one image and using the same objects on a second image for comparison), classified objects change detection (COCD, objects get extracted and classified on multiple images and are then compared) and multitemporal/multidate-object change

detection (images get stacked before extraction of objects, same objects for all images are created) (Hussain et al., 2013).

An advantage of OBIA is that the resulting data is easily applicable in geographic information system (GIS) software. Blaschke describes OBIA as “the link between the remote sensing world and GIScience” (Blaschke, 2010, p. 7). Nevertheless, the framework faces some issues. Hussain et al. outline some of them in their text: firstly, segmented objects not always correspond with reality. The resolution of the imagery can hinder to depict all real-world features accurately if they are too small. Secondly, image segmentation algorithms rely on parameters set by the user, which often entail trial-and-error methods, which can be time-consuming (Hussain et al., 2013). When it comes to change detection, factors such as unlike sensors when taking the imagery, differing atmospheric conditions, or different angles of the sunlight between the imagery, can lead to conflicting results (Singh, 1989).

3.2 eCognition

The image analysis software used in this thesis is “eCognition Developer 9.4” developed by Trimble. While other software, like “ERDAS Imagine” and “ENVI”, exists, eCognition is specifically used for OBIA and offers a multitude of tools and algorithms. A lot of papers referred to as OBIA, originally emerged from this software (Blaschke, 2010).

One key aspect of eCognition is the so-called “Process Tree” (PT). The PT allows us to design a sequence of given algorithms. These sequences are stored in “rulesets”. Different algorithms can thus be combined to generate specific workflows. An example of a basic ruleset is given in Figure 2.

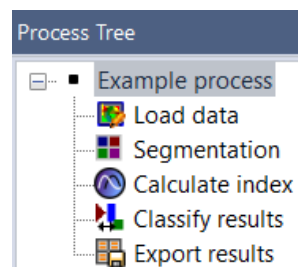


Figure 2: Example of a basic ruleset in eCognition

Figure 2 shows a ruleset loaded into eCognition. The ruleset shows up in the PT section. It has a specific structure: the parent process named “Example process” has several child processes. In this case, the parent process executes its child processes one after the other, from top to bottom. In our example a very basic workflow emerges; image data is loaded, then segmented into objects, then an index is calculated based on the data’s spectral profile, upon which the objects are classified and finally the results are exported. This basic example already shows the automation capabilities of eCognition and its PT, as this process is repeatable for multiple data sets.

The next step in making these processes more accessible to users is the creation of an “action library” (AL). An “action” in eCognition is “a predefined building block” (Trimble, 2017, p. 238), which can be configured to execute certain tasks. The AL stores “action definitions”, which are unconfigured

actions. These “action definitions” can be used to build up a user interface, where they are tied to processes in a ruleset. Widgets, such as buttons or dropdown menus, are used to visualize the “action definitions”. Pressing a button can then execute a specific parent process, as the button is tied to a process in the ruleset. Another part of this structure is the “parameter sets” (PS). The PS is used to transfer information given by the user, for example by choosing a certain value in a dropdown menu or slider widget, to the processes which are to be executed. An example would be the selection of a file through a “Select file” widget, where the PS would then deliver the path of the file to the import process (“Load Data” in Figure 2) within the ruleset. The PS thus consists of a set of variables, adjusted by the user. Every action definition can have its own PS.

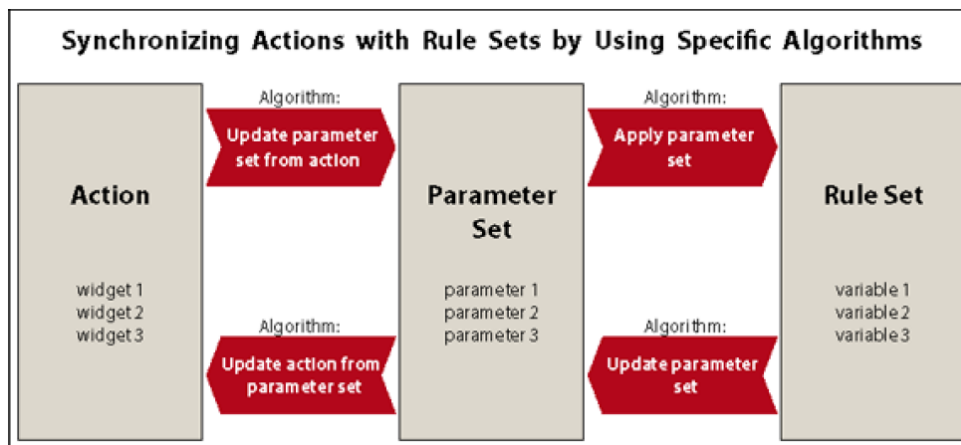


Figure 3: The communication between action and ruleset is organized by algorithms (Source: Trimble, 2017, p. 239)

Figure 3 shows the interaction between action, parameter set, and ruleset through algorithms. As observable in the figure, the action consists of widgets, by which the parameter set is updated by the “Update parameter set from action” algorithm. By applying the parameter set, the values set within the widgets are transferred to the ruleset. Yet, this works the other way around as well: variables of a ruleset can be transferred to a parameter set and then to the widgets of an action. This happens through the “Update parameter set” and “Update action from parameter set” algorithms. To make the whole concept more tangible a short example will be given over the next paragraphs.

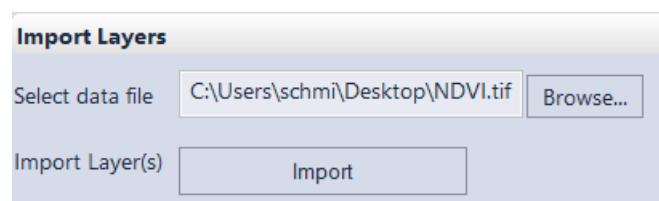


Figure 4: Example of action definition

In Figure 4, one can see a very basic example of an action definition. Its name is “Import Layers” and it has two widgets: one lets the user select a file and the other is a button to execute the process of

loading the file into the application. What the user cannot see are the PS and the ruleset behind these widgets. First, the PS is shown in Figure 5.

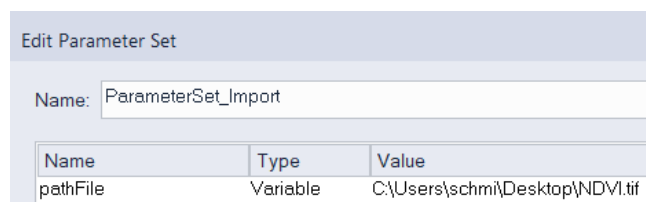


Figure 5: Parameter set example

The PS behind the “Import Layers” action definition is in this case called “ParameterSet_Import”. It only contains the variable “pathFile” which contains the path to the file selected by the user through the “Select file” widget. The last part is the ruleset, which is shown in Figure 6.

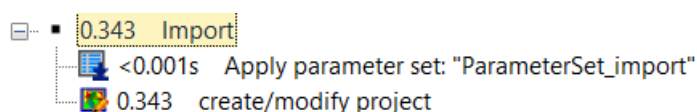


Figure 6: Ruleset example

We see the import process with its two child processes. When pressing the import button shown in Figure 4, the “Import” process in Figure 6 is executed. First, the PS “ParameterSet_import” is applied, which stores the file path of the data selected in the variable “pathFile”, which can then be used within the ruleset. This variable is subsequently used in the “create/modify project” algorithm to load the specified file into the application. The numbers before the process names are time elapsed to execute the processes. We end up with a file loaded into eCognition. This is a very basic example of how such an action library behaves in practice. Upon this foundation, more complex processes can be built and tied to other widgets and action definitions. A certain degree of automation can be achieved when working with similar data sets. We will see more on the application of the process tree and eCognition in general when the LIVID application is discussed in chapter 3.3. More information on the subjects discussed in this subchapter can be found in the “eCognition Developer User Guide” (Trimble, 2017).

3.3 Long Image Time-Series Variability Indicator Description (LIVID) approach

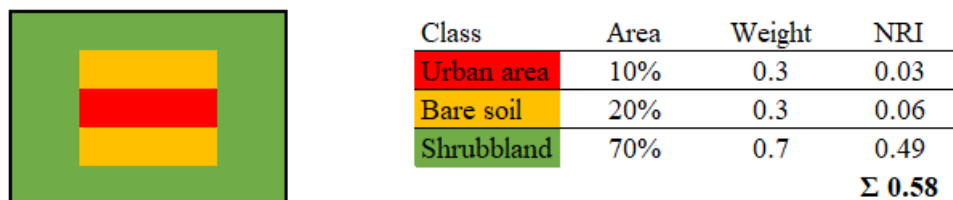
The Long Image Time-Series Variability Indicator Description (LIVID) approach quantifies landscape change in a fixed area over time. To show as much of the changes between fixed time points as possible, multiple timesteps with the corresponding imagery are used. In contrast to bi-temporal image analysis, which only displays the changes between the start and endpoint an analysis, LIVID aims at displaying the individual changes between as many as possible timepoints in a specific time series. The variability concept from Braun and Hochschild is used for the quantification of the changes between the different timesteps and will be introduced in the upcoming subchapter.

The LIVID framework follows a 4-step workflow: first, the imagery is pre-classified using an algorithm, such as SIAM (Satellite Image Automatic Mapper) or CLC (Corine Land Cover). This provides classified images in which the individual pixels are grouped into different categories, ranging from vegetation and barren land to clouds and snow. This process will be touched upon later. Second, the user can define broader classes, grouping multiple landcover classes, and weights can subsequently be assigned to these superclasses, within the application. Third, objects, in the form of equally sized reporting units, are created and the “natural resource index” (NRI) is calculated for them. Fourth, the variability is calculated based on this index. More on the last two is explained in the following subchapter. Chapter 3.3.2 illustrates how this concept was implemented as an application with a graphical user interface within eCognition. As the goal of this thesis is to further develop this application, newly implemented features by the author are showcased in chapter 3.3.3.

3.3.1 Variability

The variability concept applied in this work was already employed in the papers of Hagenlocher, Lang, and Tiede (Hagenlocher et al., 2012), and Braun and Hochschild (Braun and Hochschild, 2017). The next few paragraphs and graphics will, therefore, be based on these texts.

Before their concept of variability is described in detail, the “natural resource index” (NRI) must be introduced. The NRI was used by Braun and Hochschild to describe landscape change. A grid was first overlaid over an image, dividing it into even cells. These cells, or “reporting units” (RU) serve as the actual objects in the LIVID approach, and no other segmentation algorithms were applied. Figure 7 shows how the NRI was calculated for one cell: the relative area of a class per cell was multiplied by an assigned weight, these values were then summed up for every class, equalling the NRI. The weights were defined by the importance of the class for environmental integrity, but also for human security and were defined by regional experts (Braun and Hochschild, 2017).

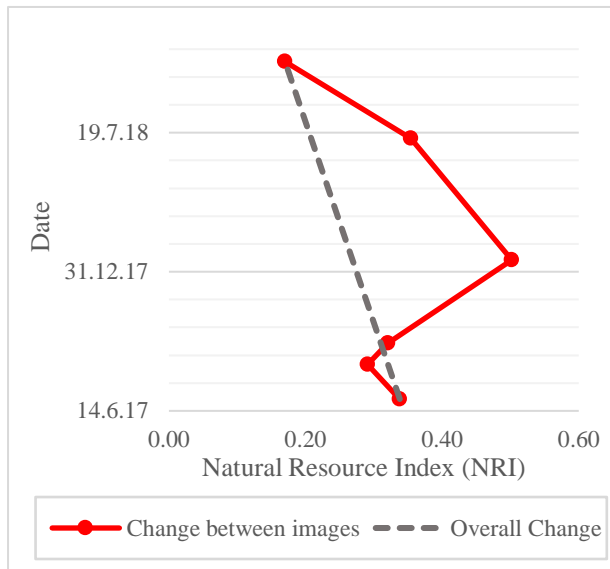


$$NRI_{cell} = \sum (\% \text{ Area of Class in cell} * \text{Weight of class})$$

Figure 7: Natural Resource Index (NRI) calculation for one grid cell (based on Braun and Hochschild, 2017, p. 9)

In contrast to bi-temporal change detection, where only two images are compared, the authors tried to include several timesteps over the period analysed. The variability approach incorporated not only the overall change between the start and endpoint of a time series but also inter-image changes (Sudmanns et al., 2019). Figure 8 shows how measuring points are plotted in a graph and how the variability was

thus calculated. The Pythagorean theorem is used to calculate the individual distances between the points.



$$\text{Variability} = \frac{\text{Change between images}}{\text{Overall Change}}$$

Figure 8: Calculation of the variability of a reporting unit (own depiction, based on Braun and Hochschild, 2017, p. 11)

In a first step, the length of the vector representing the overall change of NRI, or the change between the start and endpoint, was calculated. The second step involved calculating the sum of vectors representing the changes of NRI between every pair of time points. The third and final step was calculating the ratio between the sum of annual changes and the overall change. This ratio was finally described as variability. If the length from the start to the endpoint was the same as the distance between all points, the variability is 1. The higher the sum of distances between the individual points in comparison to the distance from the start to the endpoint, the higher the variability (Braun and Hochschild, 2017).

In more practical terms this implied that for every RU the NRI was calculated for every image included in the analysis. To put this as an example: supposed a data series with 3 images was taken, which meant that we have 3 images with differing dates of the same region. With this foundation, the difference between NRI values at the start (image 1) and endpoint (image 3) can be calculated. Simultaneously, the distance between two successive NRI data points was calculated and these values were summed up. This sum was thereby composed of the distances between points 1 and 2 and between points 2 and 3. The variability was formed again of a ratio: the overall change was the denominator and the sum of changes was the nominator. The variability per cell or reporting units can be understood as a stacking of cells corresponding to different dates of analysis, as seen in Figure 9. The higher the variability value, the more change occurred within the cell.

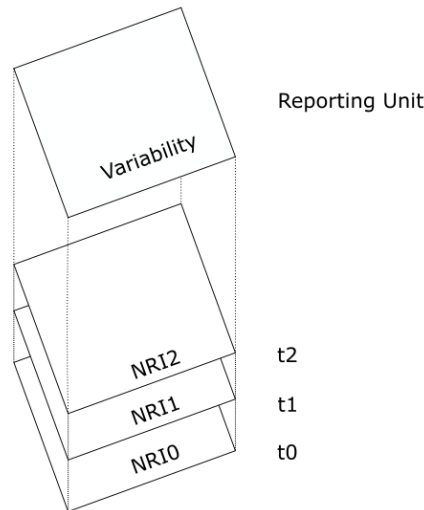


Figure 9: Variability calculation by reporting unit (based on Hagenlocher et al., 2012, p. 32)

The following chapter will illustrate how this concept is developed as an application within eCognition and will give an overview of its specific functions.

3.3.2 The LIVID application

As already mentioned, the LIVID application, which builds on the concepts of the NRI and variability, was compiled in eCognition by Dirk Tiede, Martin Sudmanns, and Hannah Augustin. In eCognition, a graphical user interface (GUI) can be created to build custom applications more accessible to users. Over the GUI, buttons, sliders, dropdown menus and other helpful widgets can be combined in groups. An example of how the LIVID GUI looks like in practice is given in Figure 10.

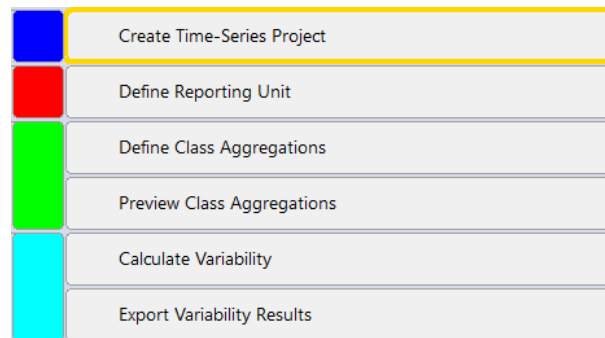


Figure 10: LIVID application GUI

The groups visible in Figure 10 consisted of different functions. The first group is called “Create Time-Series Project”. To give a better insight into the GUI and into the group itself, the functions are shown in Figure 11 below:

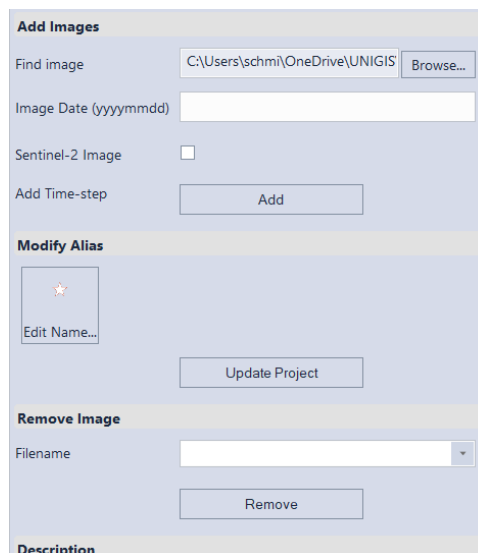


Figure 11: “Create Time-Series Project” group in the LIVID application

It is important, that the images are loaded chronologically using the “Browse...” button, with the first image being the earliest. The number of images is not restricted and can be chosen by the user. As soon as the right image is found in the file selector, the user needs to type in the image date with a “yyyymmdd” format. Alternatively, if a “Sentinel-2” image is loaded, the corresponding box can be ticked, and the image date is automatically extracted from the file name (this function was added over course of this thesis). After an image is loaded, its image date, or alias, can be modified with the “Edit Name...” button in the “Modify Alias” section. The “Update Project” button refreshes the project information. The last section in this group is titled “Remove Image”: via the dropdown menu, an image can be selected and removed with the “Remove” button. At the bottom of every group is a “Description” section, where by hovering over an element, a description of the functions behind this element appears. The user can choose between hexagons and squares as reporting units when selecting the “Define Reporting Unit” group. While the squares can be created by an existing algorithm in eCognition (“chessboard segmentation”), the algorithm for the hexagons was created by Dirk Tiede. Also, the size of the units can be defined by a scale variable trough an “edit box” widget. The unit here is pixels, which means that if the imagery has a resolution of 10m, a scale value of 100 would equal squares with sides of 1000 meters (100 pixels times 10 meters = 1000 meters). In Figure 12 we see how square and hexagon reporting units are lain over an area in practice. Finally, the reporting units can be deleted with a button with the fitting caption of “Delete Units”.

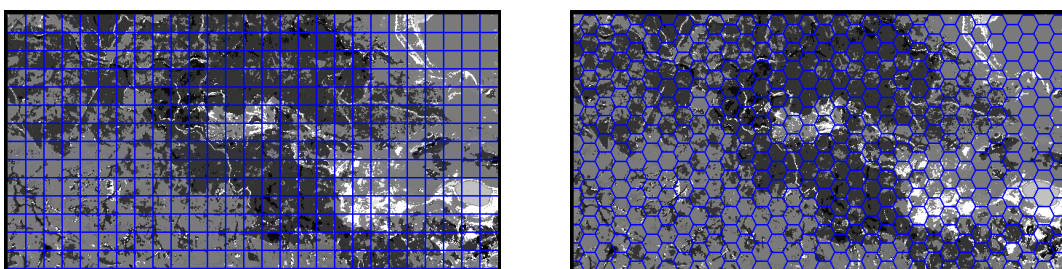


Figure 12: Reporting units (blue lines) overlaid on an image (left: squares, right: hexagons, scale 25)

Through the “Define Class Aggregations” group the user can define specific classes and choose their weights. As this procedure consists of several different steps, an overview of the GUI of this group is given in Figure 13.

Figure 13: “Define class aggregations” group in the LIVID application

The user will notice that some classes are already predefined in the dropdown menu “Class”. These classes (low LAI vegetation, high LAI vegetation, bare soil/built-up, water, and unclassified) serve as examples. With the “create new class” option in this menu, a pop-up window opens, and the user is free to create their classes. The number of classes can thus be defined by the user and has no limitation. In the “Define Semi-Concept Interval” section, the semi-concept boundaries of the specific classes can be set. As already mentioned above, the imagery used in the LIVID application is pre-classified by a landcover classification system, such as the SIAM™. For the example of the SIAM™ algorithm, an area is divided into 33 landcover classes, which are used as semi-concept values (more on the “SIAM™”-pre-classification in chapter 4.2). As soon as the right values are selected, a specific weight can be assigned to the class via a slider in the “Weighting” section. If all options are set for, or if the user wants to modify a specific class, it can be confirmed by the “Assign or Update” button. A single class can be modified by selecting it in the dropdown menu and assigning new semi-concepts or weights. If the user wants to delete all classes, the “Reset” button needs to be pressed.

Within the “Preview Class Aggregations” group, an image, or “timestep” is selected in a dropdown menu. The user can then, with a click on the “Select Area” button, select several reporting units via cursor. If the user has already predefined classes in the previous group, a click on the “OK” button in the “Generate Preview” section of this group will calculate and show a preview of the classes for the selected reporting units on the selected timestep. How this looks in practice for a set of hexagon reporting units, is depicted in Figure 14.



Figure 14: Classified hexagon units (scale: 25)

This classification, together with the defined weights, serves as the basis for the calculation of the NRI value. A “Clear” button removes the classified units.

Under the “Calculate Variability” group, the functions demanding the highest amount of calculation are found. A slider allows the user to define the amount of unclassified area a cell can have per level, to still be incorporated into the variability calculation. This feature was implemented within this work and will be further discussed in chapter 3.3.3. The variability calculation is started by pressing the “Run” button in the “Calculation” section. Beforehand, reporting units must have been defined, if not, a warning message shows up and the calculation is not executed. The variability calculation has two main steps. In the first step, the NRI value gets calculated for every reporting unit on every timestep or level. The formula for the NRI calculation of chapter 3.3.1 is stated again as a reminder:

$$NRI_{cell} = \sum (\% \text{ Area of class per cell} * \text{Weight of class})$$

The NRI per reporting unit is thus the sum of the products of the class area times their corresponding weights. The indicator value ranges from 0 to 1. The NRI values are then classified into low (< 0.3), medium (< 0.7) and high (> 0.7). Figure 15 shows how reporting units are classified.



Figure 15: classified reporting units (hexagons), based on NRI values (red: $NRI < 0.3$, yellow: $NRI < 0.7$) (Andalusia 01.07.2017)

With this database, step 2, the actual variability calculation can begin. We have seen the formula of the variability calculation in chapter 3.3.1. Now, in the application, with the appropriate variables, the variability would be calculated as follows:

$$\text{Variability (NRI)} = \frac{\sum \sqrt{(NRI_t - NRI_{t-1})^2 + \left(\frac{T_t - T_{t-1}}{T_n}\right)^2}}{\sqrt{(NRI_n - NRI_0)^2 + \left(\frac{T_n - T_0}{T_n}\right)^2}}$$

With T or “Timestamp” the number of days from the specific measurement since the first measurement is meant. In this formula, the nominator would equal to the sum of changes and the denominator to the overall change. We now not only have a variability value for every reporting unit, but also an NRI value for every level.

The last group is named “Export Variability Results”. In short, NRI and variability values, destined for further processing in GIS software, can be exported in this group. As the group was fully implemented in this work, it gets explained in more detail in the subchapter 3.3.3.

A simplified overview of the application's workflow is given in Figure 16.

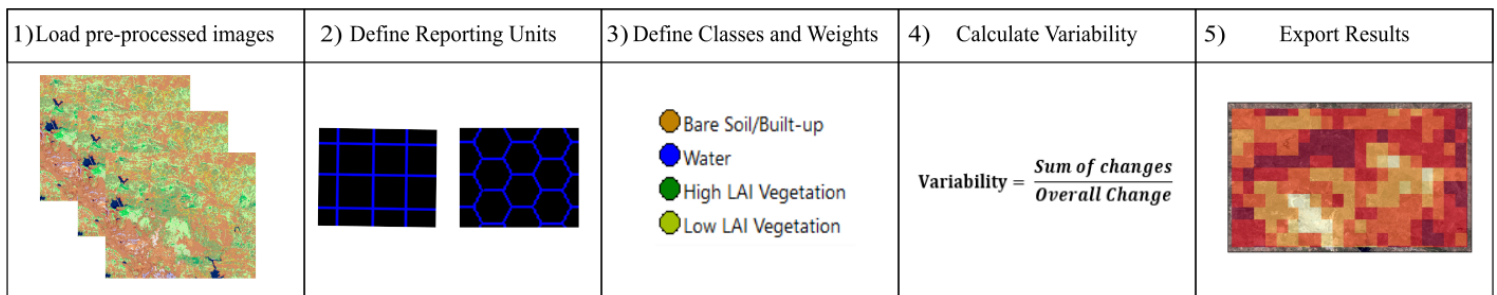


Figure 16: Simplified workflow of LIVID application

The user must take phenomena like seasonal variations into account when processing imagery with this tool. This is also the case when it comes to setting the weighting of the classes, which demands a certain background knowledge of the analysed region by the user.

3.3.3 Implemented features

While working on this project, several functions of the existing LIVID application were expanded upon. These expansions not only include smaller quality of life adjustments, but also more conceptual modifications. They were made to enhance the usability of the application. The following subchapters give an overview of these newly added functions, their implementation and they can also be inspected within the application.

A first addition consisted of a process to extract the image date from the file name when loading images into the LIVID application in eCognition. This procedure relieved the user from typing every image date into an “edit box”-widget, which was very time consuming when processing several images.

A prerequisite for the process to work is the right file name format, which is in this case “ttt_yyyymmdd” (t = days since beginning of analysis, y = year, m = month, d = day). If this condition is complied with, the user can tick a corresponding tick box, and the image date is extracted by the application. See Figure 17 for the updated GUI (Graphic User Interface).

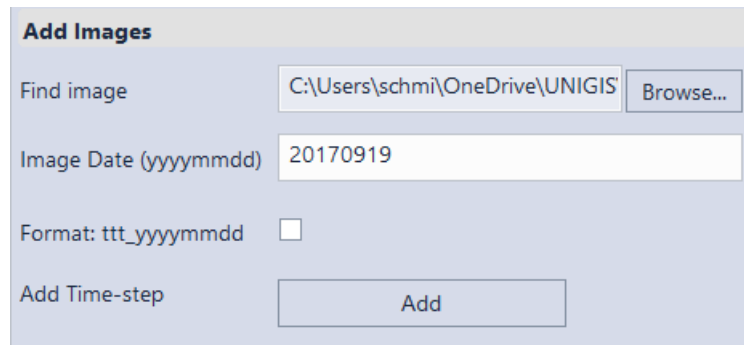


Figure 17: Updated GUI with file name format tick box

The “Setup” part of the process tree had to be altered to make this extraction work. Several variables were used to shorten the file name of the image to the requested “yyyymmdd”-format. The relevant part of the process tree can be seen in Figure 18.

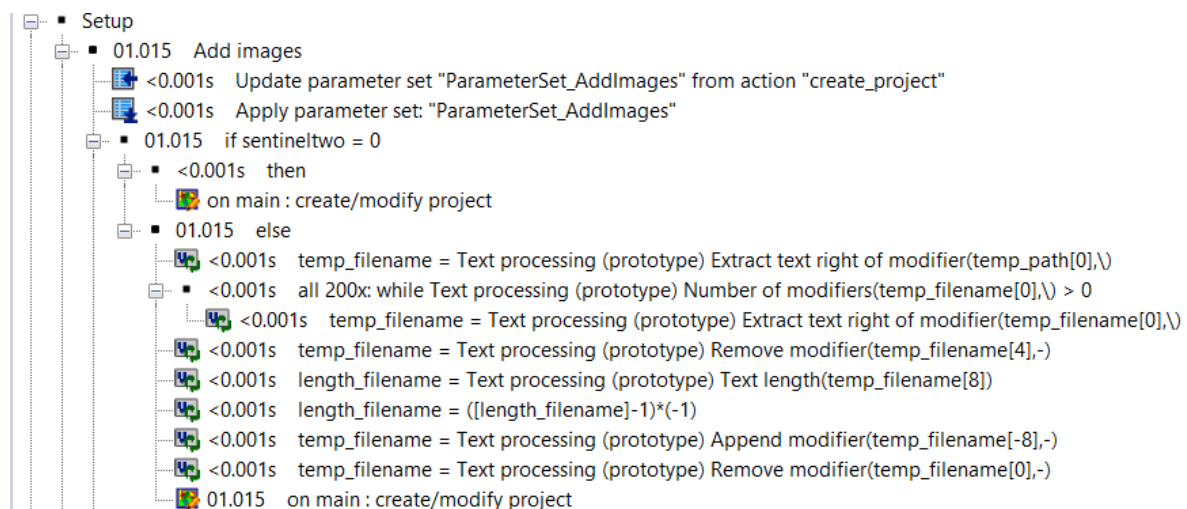


Figure 18: Updated process tree with file name extraction

To explain how these algorithms work, an example is made, by explaining the process behind extracting the image name “20170117” from the file name “000_2017-01-17-Spain.tif”. As a first step, the path of the file gets copied in the variable “temp_filename”, before cutting off the folder structure, which leaves us with “000_2017-01-17-Spain.tif”. The variable then gets shortened by its four first digits, which incorporate the imagery’s timestamp, in our example: “000_”. In the same step, the “-“ in the filename gets removed. If we follow our current example, the variable “temp_filename” would now have the value “20170117Spain.tif”. A difficulty was now to eliminate the “Spain.tif”-part of this value. Imagery loaded into the application could also be from other countries and so the length of this segment can vary between projects. Fortunately, eCognition has a function to determine the length of a variable starting from some specific point. As the date always stays in the same format (“yyyymmdd”, so 8 digits), we can start at the 8th digit and count how long the part is, which gets then stored in “length_filename”. This variable gets then subtracted by 1 and multiplied by -1. This is necessary as in the next step, a so-called modifier (in this case “-“ again), gets added before the position in which the

“country”-part begins in the “temp_filename”-variable. The “-1” is multiplied as we count from behind. The modifier “-“ gets then removed from the variable “temp_filename”, which also removes the part containing the name of the country. This leaves us with “20170117” for the variable, and this can be used as “layer alias” in the “create/modify project”-algorithm, which finally loads the file into eCognition.

Given that no export function existed in the first version of the application, different ways to export the results of the variability calculation were implemented. After choosing a specific export path for the files to be saved in, the user has the option to export a shapefile with the variability values for the different grid cells. It is however also possible to export the NIR values for the individual images. The user can choose the desired timestamp in a dropdown menu and then choose between an export as a grid, in form of a “.tif”-file, or in form of a “.csv”-file. The visual representation of these features can be seen in Figure 19. With the checkboxes, the user can export relevant files per timestamp in one click.

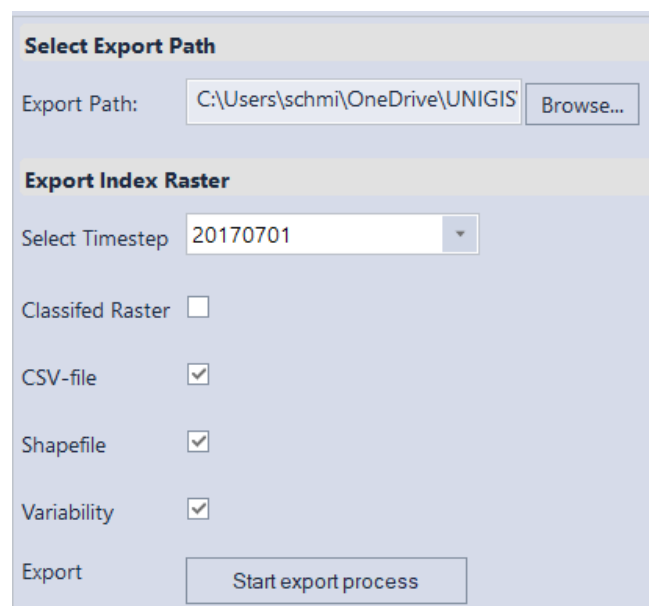


Figure 19: Implemented export GUI in LIVID application

Some grid cells can, on different timesteps, include areas that are not classified by the user, such as clouds or “no data” cells. An area is unclassified when it falls into a landcover class, which does not belong to one of the superclasses defined by the user. For example, if the user has defined three superclasses, one for all vegetation, one for all bare soil or built-up areas, and one for water surfaces, all areas not belonging to one of these three superclasses, such as clouds or snow, fall under unclassified. If a cell incorporates too much area which is unclassified, it can be excluded from the variability calculation.

A slider tool in the “Calculate Variability” section of the application allows the user to define a specific “NoData” threshold. The slider ranges from 0 to 100. 0 would be meaning that no unclassified area is

accepted per cell and 100 would be meaning that cells entirely consisting of unclassified areas are still considered in the calculation.

When calculating the NRI value per cell, the variable “obj_NoDataFlag” is set to 1, once the percentage of the unclassified area exceeds the number defined by the user on the slider. We use this variable to filter out which of the NIR values are then used for the variability calculation. The altered algorithms of the variability calculation process can be seen in Figure 20.

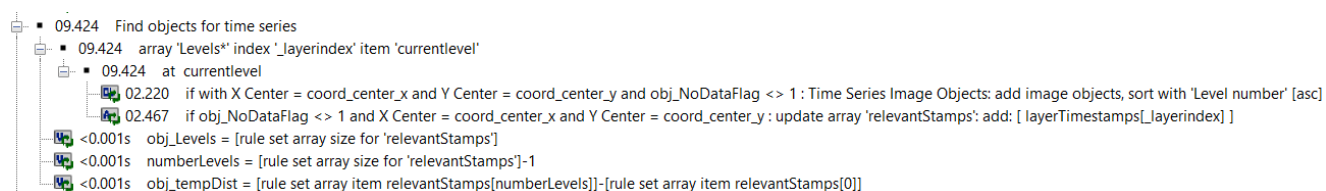


Figure 20: Altered variability calculation process with implemented "No Data"-threshold

The relevant cells/values are stored in an image object list (“Time Series Image Objects”). Within the filtering process, not only the relevant cells but also their timestamps are saved. These timestamps are important for the individual cells, as their overall temporal distance must be assessed for later calculations. This value is stored in the “obj_tempDist” variable, by subtracting the last timestamp by the first one:

$$\text{Temporal Distance} = \text{Timestamp}_n - \text{Timestamp}_0$$

To demonstrate which results can be expected with this tool, variability calculations with different thresholds were tested with the study area in Andalusia, Spain in Figure 21. The overlying polygons depict the forests, which were subject to forest fires.

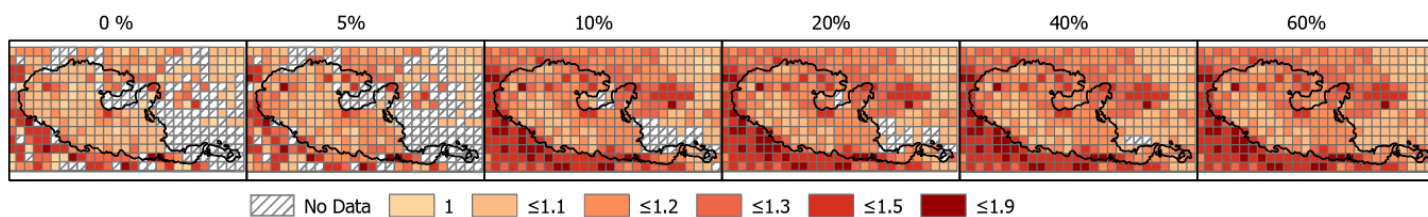


Figure 21: Variability values at differing NoData-threshold (scale: 1:150000)

The thresholds tested ranged from 0% to 60% of the unclassified area accepted per cell (time series object). We see that for 0%, the variability could only be calculated for a small number of reporting units. For reporting units classified with “No Data”, less than 2 objects complied with the threshold. If only one or no timepoint per reporting unit is eligible for the calculation, no variability can be computed for the reporting unit. As expected, with a higher threshold the number of these cells decreased. Over 60%, all objects on all reporting units are used for this specific test case.

In some cases, the variability of specific reporting units changes with a different threshold. The reason for this is, that either more or fewer objects are incorporated in the variability calculation if the threshold

changes, dependent on the percentage of the unclassified area of the objects. An example: for a specific reporting unit at a threshold of only 10% only three timesteps are incorporated into the variability calculation. If the threshold is now raised to 60%, six timesteps can now be incorporated into the calculation as now more cells comply with the new NoData-threshold. This changes the temporal and variability distances between the timesteps and leads subsequently to a different result.

This addition, however, brings some conceptual difficulties which were not resolved at this time. One issue is the comparability between the resulting variability results if they have a differing start or/and endpoint between the individual cells. This could be the case if the start or/and endpoint falls underneath the “No Data”-threshold. This issue could be resolved by fixing the “No-Data”-threshold of start and endpoint to 100%, no matter how the user fixed the value on the slider widget. Generally, a differing number of timepoints between the cells could lead to difficulties when comparing their variability values.

While using the “Preview Class Aggregations” function of the application, it appears that the layer of which the preview was calculated, didn't change when another timestep was selected in the “Select Time-step” dropdown menu. The reason for this was, that the “var_lyr” variable was not updated upon selecting another timestep in the mentioned dropdown menu. This variable is however responsible for delivering the layer on which the preview is calculated. The “Apply parameter set” algorithm, applying the “ParameterSet_Preview” was added to the “Generate Pseudo Objects”-process to resolve this circumstance, thus updating the “var_lyr” variable before calculating the preview.

3.3.4 NDVI and NBR calculation

The results from the LIVID approach are compared with variability results from other, established indicators, to see how these are depicting the occurrence of such a forest fire. The “Normalized Difference Vegetation Index” (NDVI) and the “Normalized Burn Ratio” (NBR) are selected for this task.

The NDVI is one of the most applied spectral indexes in remote sensing. Its first implementation dates back to 1973 and was executed by Rouse et al. in their paper on the Great Plains of the USA (Rouse et al., 1973). The reasons for its long and wide application are certainly the indicator's simplistic formula and its link with the photosynthetic capacity of vegetation. The indicator is calculated based on the near-infrared radiation, which is reflected by the photosynthetic pigments of leaves, while the rest of the visible light is absorbed by them, thus giving an indication the existence of green vegetation in an area (Robinson et al., 2017).

The NBR is formed similarly to the NDVI, which we will see in its formulas later. The NBR calculation compromises the two satellite bands which respond the most to a fire event. While the near-infrared band shows a negative trend after a fire, the short-wavelength infrared band shows a positive one after such an event. The combination of these bands brings the most considerable distinction between burned and unburned areas. A negative NBR is an indication for a burned area, while a positive NBR represents

an area with intact vegetation (Key and Benson, 2006). To calculate these indicators within the LIVID application, several changes had to be made. First, an adaptation to the “Add images” group in the “Create Time-Series Project” section was made. Figure 22 shows the updated GUI.

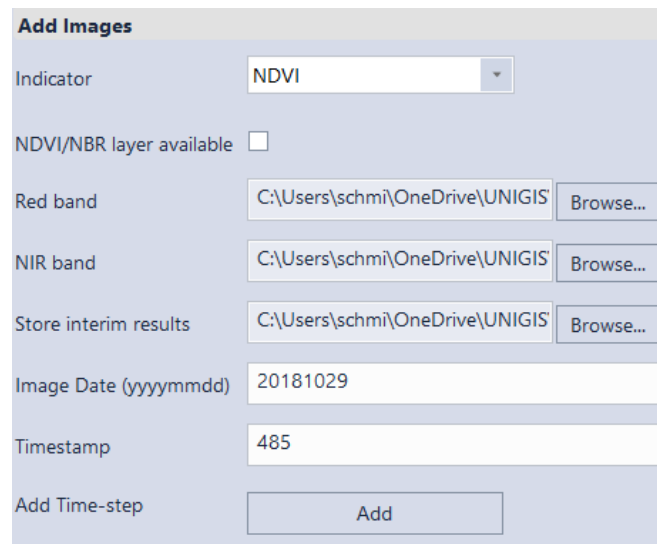


Figure 22: Updated "Add images" group for NDVI and NBR calculation in LIVID application

A dropdown menu lets the user choose between NRI, NDVI, or NBR. The process for the NRI calculation has not been changed. If pre-calculated NDVI or NBR layers exist, the user can tick the “NDVI/NBR layer available” checkbox and the process is the same as for the NRI. The user now also has the option to calculate NDVI or NBR layers within the application. For this, two satellite bands per indicator are needed. For the NDVI calculation, the red and the near-infrared bands are needed, whereas, for the NBR calculation, the near-infrared and the short-wave infrared bands are needed. The formula for calculating the NDVI and NBR are the following:

$$NDVI = \frac{NIR - red}{NIR + red}$$

Source: Anyamba and Tucker, 2005

NIR = Near InfraRed

$$NBR = \frac{NIR - SWIR}{NIR + SWIR}$$

Source: Key and Benson, 2006

SWIR = Short-Wavelength InfraRed

Furthermore, the user must specify a place to store the interim results, in the form of the pixel-based NDVI or NBR layers. The bands are being loaded into the LIVID application and the chosen indicator gets calculated for each pixel. The “layer arithmetics” algorithm is used to carry out the calculations. Since eCognition does not allow to only have temporary layer open in a project, the resulting temporary layer gets exported into the export folder and is loaded again to change it into a permanent layer. The

last step is to delete the band layers and the temporary indicator layer from the project, leaving us with the permanent indicator layer, whether NDVI or NBR.

The “Calculate Variability” section and its processes had to be adjusted too. When the NDVI or NBR indicator is selected by the user, the index per reporting unit needs to be calculated in a different way as for the NRI. The user can, therefore, choose between assigning the value of the reporting unit by calculating the mean or the median of the values within it. The variability calculation itself does not differ from the NRI calculation. The sections “Define Classe Aggregations” and “Preview Class Aggregations” are disabled for these indicators. An updated LIVID workflow is showcased in Figure 23.

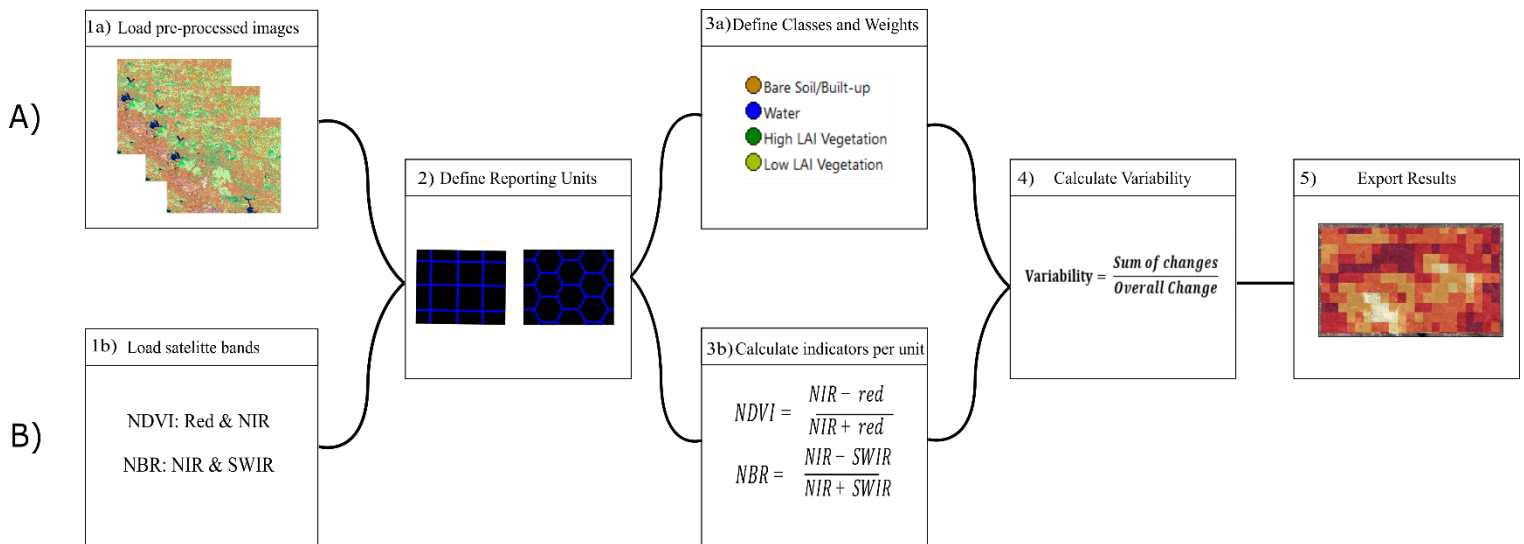


Figure 23: Updated LIVID workflow, where A is the process for NRI, and B for NDVI and NBR

In Figure 23, the LIVID workflow shows both the process for the NRI (A) and the NDVI/NBR calculation (B). The user can now calculate NDVI and NBR values within the LIVID application by loading the appropriate satellite bands, as depicted in step 1b. However, it is, if calculated before, also possible to directly load an NDVI or NBR file. As a second step, the reporting unit is defined in the two processes. When for the NRI process, step 3a means defining classes and their weights, step 3b lets the user choose between calculating the mean or the median of the NDVI and NBR of the pixels inside the individual reporting units as the overall value for them. For both processes, the workflow ends with the calculation of variability values and their export.

The two integrated indicators were implemented as they are beneficial for the specific case study of a forest fire. When analysing other scenarios, other spectral indicators might prove even more useful. With the current composition of the LIVID application, it would be easy to add more spectral indicators to it. It is conceivable that the list of indicators could be expanded upon so that the application can be utilized for other scenarios. After having focused on the LIVID approach and its application within eCognition, it is time to test its functions on a specific case. The following chapter will, therefore, focus

on a case study of two forest fires in Spain in the year 2017, which aims to offer a more practical view on the approach and its results.

4 Case Study: Forest Fires in the Huelva Province, Andalusia, Spain (2017)

Forest fires are a recurrent phenomenon in Spain and the Mediterranean. According to the Spanish “Ministry of Agriculture, Fisheries and Food” (MAPA), 13793 forest fire incidents were counted in Spain in 2017. A total area of 1782 square kilometers of the forest was affected by these fires in that year. 15.81% of the cases occurred in the “Mediterráneo” region, to which Andalusia belongs. The absolute number of cases in Andalusia was 968 and the area affected accumulated to 15608 hectares (MAPA, 2018). Vallejo-Villalta et al. report that in Spain, in 96% of the cases, humans are causing the fires, either intentional or unintentional (Vallejo-Villalta et al., 2019).

According to the updated “Köppen-Geiger” climate classification system by Peel et al., West-Andalusia is classified as “Csa” or “Temperate dry and hot summer” type (Peel et al., 2007, p. 471). In the “Köppen-Geiger” system, the “C” stands for temperate zones, which are described as regions with average temperatures of more than 10°C in the hottest and between -3°C and 18°C in the coldest month of the year. The “s” means that the summer is the dry season, which entails that there is three times more precipitation in the wettest month of winter than in the driest month of summer. Further, the rain in the driest month must be less than 40 mm. The “a” finally stands for hot summer, where the average temperature of the warmest month has to be over 22°C (Peel et al., 2007). These properties can be verified in the climograph of Huelva in Figure 24.

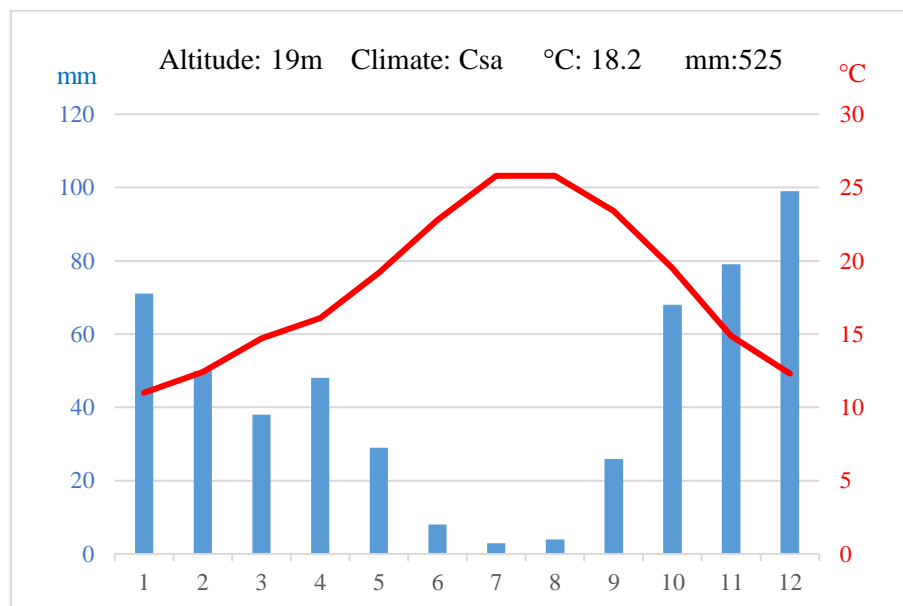


Figure 24: Climograph of Huelva (1984-2010) (source: AEMET, 2015, own depiction)

The region has very dry summers, with less than 5 mm of precipitation in July and August. Moreover, mean temperatures in these months are around 25°C, while mean maximal temperatures reach 32°C. The winter months of January and December bring lower mean temperatures of around 12°C and far more precipitation of 71 and 99mm respectively (AEMET, 2015). These weather conditions create favourable conditions for forest fires in the summer months.

To examine the performance of the LIVID application in cases of abrupt change, the example of two forest fires in roughly the same area and time frame in the Huelva province, in West-Andalusia, Spain in 2017 was chosen. This event was also chosen for a case study, as the “Emergency Management Service – Mapping” of the European Union (EU) published a detailed account on it in its “EMSN-060”-report. Two areas of interest (AOI) were defined in the manner as in the EMSN-060 report. As the EMSN-060 report is an important indicator for the case study, it will be analysed in the following sub-chapter. These can be seen in Figure 25.

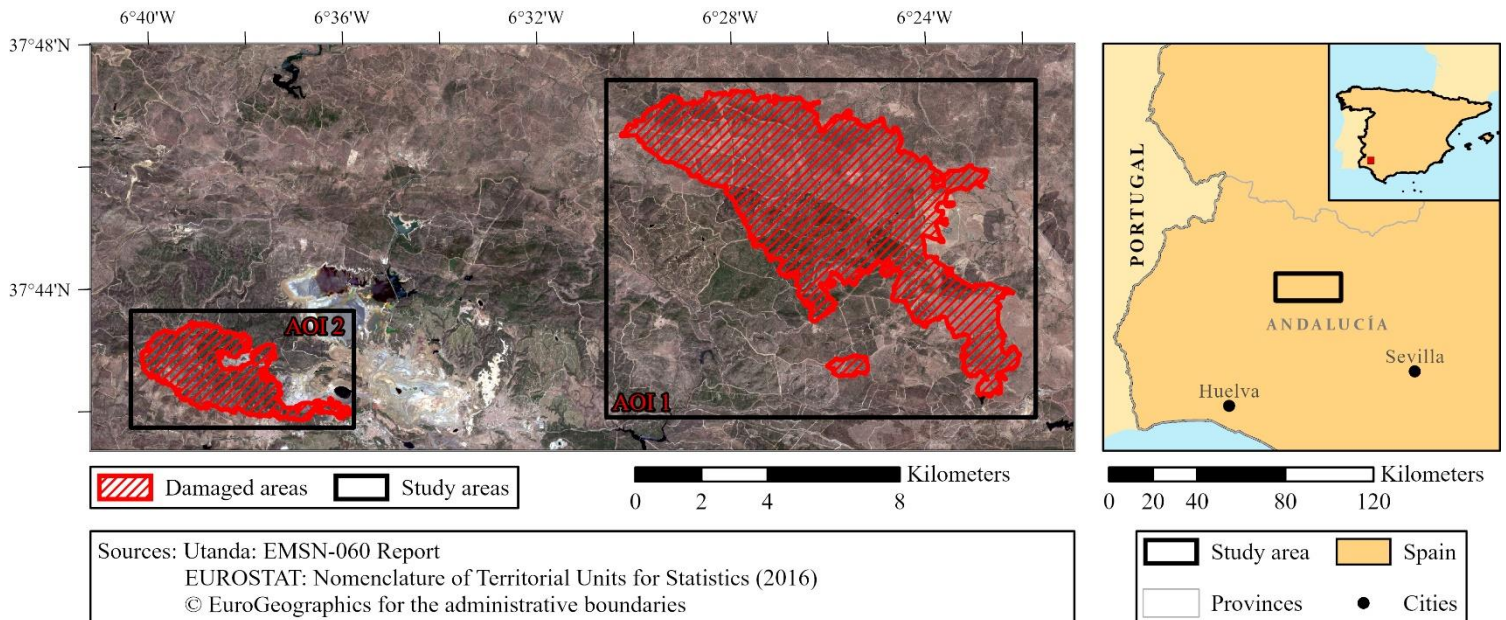


Figure 25: Study area with damaged areas (scale: 1: 200,000, sources: damaged areas: EMSN-060 report (Utanda, 2019), base map: Copernicus Sentinel data from 01.07.2017), administrative boundaries: (EuroGeographics, 2016))

AOI1 is named “*La Granada de Río Tinto*” and has ecological and environmental significance as it was classified as “Red Natura 2000” being part of the “*Sierra de Aracena and Picos de Aroche*” natural park. The fire in this area raged from the 8th of September to the 10th of September 2017. AOI2 bears the name “*El Campillo*” and is smaller than AOI 1. The fire in this area occurred a bit earlier, from the 3rd of July to the 5th of July 2017. A mine in the east of the second AOI is easily distinguishable in Figure 25. Mining here began around 1200 b.C, shaping the landscape entirely. In absolute terms, AOI1 has an area of 132 km² and AOI2 an area of 23 km². Of this, 42 km² are affected by the forest fires in AOI1 and 8 km² in AOI2 (Utanda, 2019). The *Regional Government of Andalusia* (“*Junta de Andalucía*”) lists in the appendix of their “*Andalusian Forest Fire Emergency Plan*” (“*Plan de Emergencia por Incendios Forestales de Andalucía*”, short Plan INFOCA) all of the municipalities in the affected areas as vulnerable to forest fires (Salas Trujillo et al., 2003). For AOI1 the municipalities are *La Granada de Río-Tinto*, *Zufre*, and *El Castillo des la Guardas*, for AOI2 they are *El Campillo* and *Minas de Riotinto*.

4.1 Results of EMSN-060

The EMSN-060 report served not only as a reliable source for additional information on the fire itself (providing a geodatabase with their results and useful shapefiles) but also as for comparing it to the results of this study. The report was developed by a collaboration of Indra, Gisat, and Z_GIS. The database consisted of Sentinel-2 imagery (same timepoints as used in the thesis), a digital surface model (DSM), a digital elevation model (DEM) from LiDAR data, an orthophoto from 2016 and of a land occupation data set from Spain (SIOSE 2013).

The initial product of the report was the “fire severity assessment”. The first part of this product was the most important one for this thesis. It included the calculation of the NDVI (Normalized Differential Vegetation Index) and the NBR (Normalized Burn Ratio) for both AOIs, divided into affected and unaffected areas, based on the Sentinel-2 data. The formulas for calculating the NDVI and the NBR were the same as the ones used in this thesis (see chapter 3.3.4). They found that the NDVI and the NBR values halved after the fire events for the affected areas in both AOIs (AOI 1: from 0.5 to 0.2, AOI 2: 0.4 to 0.2), while only dropping slightly for the unaffected areas. For the time after the fires, the values of the affected areas behave like the unaffected ones, increasing over time. The NBR values showed a similar trend, as the affected areas' values dropped under zero after fires, indicating that they were burned. After the sharp drop in the affected regions, the values tended to increase similarly as in the unaffected areas (Utanda, 2019).

The authors then proceeded to classify vegetation heights based on a DSM. Three classes were defined: low vegetation (under 1 meter), shrubby vegetation (from 1 to 3 meters), and trees (over 3 meters). Data from 2015 (pre-event) and 2018 (after the event) was compared in this step. In the case of AOI1, the area of the classes shrubby vegetation and trees declined, while the area of the class low vegetation increased in the affected areas. In the unaffected regions, the classes of low vegetation and trees decreased, while an increase in shrubby vegetation was attested. The decrease of the class “trees” in affected areas was however higher (-784.3ha) than in unaffected areas (-457.4ha). The difference in low vegetation area between affected and unaffected was immense: while the class' area decreased by 13.6ha in unaffected regions, it increased by 1065.3ha in affected ones (Utanda, 2019, p. 18). For the smaller AOI2, the area of the classes shrub and trees decreased in affected areas (-102.8ha and -183.9ha), while low vegetation increased (286.7ha). In the unaffected areas, shrub and tree areas increased slightly, the low vegetation surface area decreased slightly (Utanda, 2019, p. 17). While the areas of the shrub and trees classes decreased in affected areas, the low vegetation class expanded in them.

Product 2 assesses vegetation recovery. Vegetation was once again classified, but this time, not only the height classes from product one was considered, but also other factors like height difference and NDVI value change. The authors hence created a recovery matrix (see Utanda, 2019, p. 23) which was visualized in a map for both AOIs. The resulting product offers an overview of the areas in which the fires did the most damage and is visualized in Figure 26.

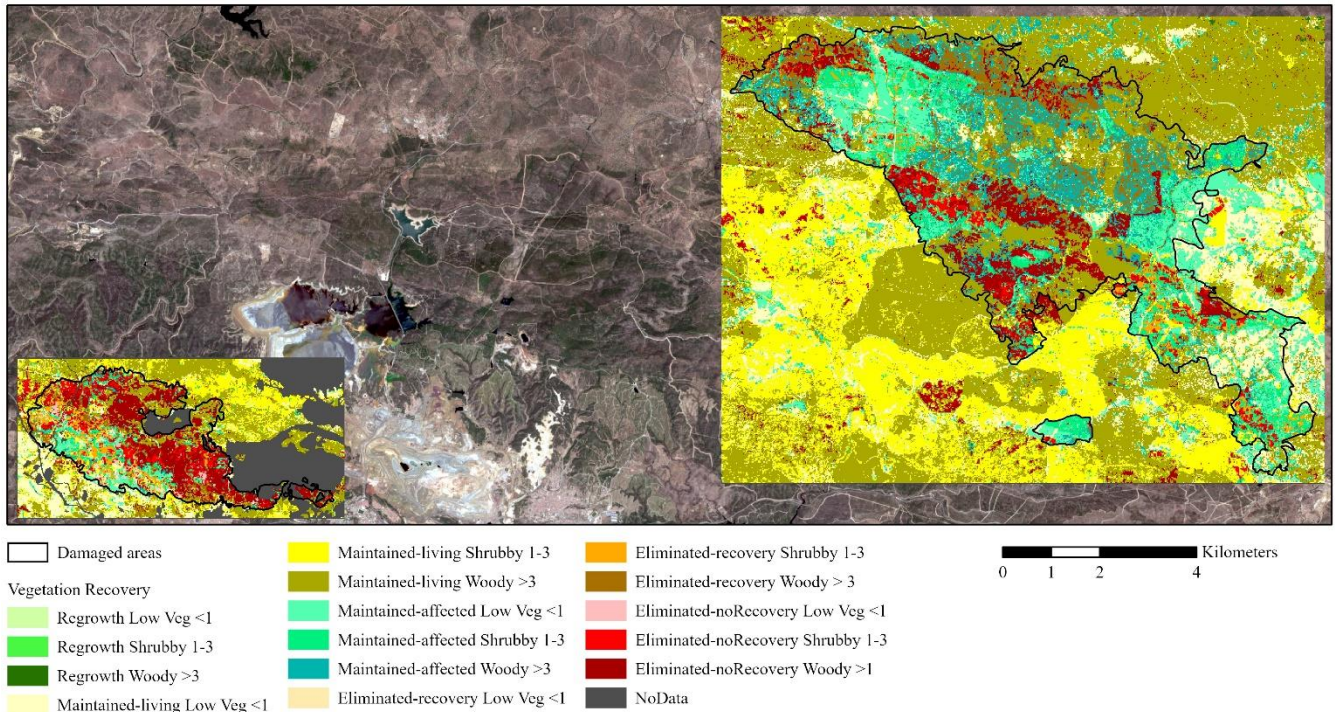


Figure 26: Assessment of vegetation recovery (Source: Utanda 2019) (base map: Copernicus Sentinel data 2017, scale: 1:100,000)

The third product was an analysis of the vegetation volume change between 2015 and 2018. The AOIs were again divided between affected and unaffected areas and the classes from product 1 were again applied (trees, shrub, low vegetation). For AOI1 the vegetation volume dropped for all three classes in affected areas, while it only dropped for trees in unaffected areas. For AOI2 the same can be said for the affected areas, but for unaffected areas, only the low vegetation volume decreased (Utanda, 2019, p. 25). Product 4 centered around the observed soil loss, product 5 assessed the road network status and product 6 the erosion and landslide risks. The authors then started with a quality control chapter on all 6 products.

4.2 Data

The data used in this thesis consisted of six “Sentinel-2” images. The “Sentinel-2” mission is conducted by the European Space Agency (ESA) and part of the Copernicus observation program of the European Union (EU). The start date was the 23rd of June 2015. It consists of two identical, polar-orbiting satellites, rotating in the same orbit, shifted by 180 degrees. With this constellation, specific places can be recorded with a temporal interval of five days. The sensors of the satellites sample altogether 13 spectral bands with differing spatial resolutions: four at 10m, six at 20m, and three at 60m. The “Multi-

Spectral Instrument” (MSI) serves as a sensor on the satellites. The data acquired by them can be used in different areas, such as environmental monitoring and crisis management (for more information on the mission see ESA, 2015 and Drusch et al., 2012). The imagery is available for free on the website of the Copernicus project (Copernicus Sentinel Hub), registration is, however, required. The dates of the “Sentinel-2” imagery used in this thesis are the same as in the EMSN-060 report: 01.07.2017, 20.08.2017, 19.09.2017, 17.01.2018, 11.07.2018, and 29.10.2018. As the number of days passed between each picture and the beginning of the analysis plays a role in the variability calculation, these numbers are noted in Table 1. The pictures originate from the “Sentinel-2” tile “T29SBQ”.

DATE OF PICTURE	DAYS SINCE BEGINNING OF ANALYSIS
01.07.2017	0
20.08.2017	50
19.09.2017	80
17.01.2018	200
11.07.2018	375
29.10.2018	485

Table 1: Sentinel-2 imagery with number of days since the beginning of the analysis

These images were, as already mentioned in chapter 3, pre-classified via the “Satellite Image Automatic Mapper™” (SIAM™) software by the supervisor team. The “SIAM™” software is developed by Andrea Baraldi. It has the advantage of running fully automatic, not needing any human interaction, in the form of user-defined parameters or training data. The “SIAM™” process can translate multi-spectral (MS) reflectance data into a set of predefined classes. In total, the MS data is translated into 33 classes (for detailed classes, see Appendix I, Table 5), with 6 parental spatial categories: clouds, either snow or ice, either water or shadow, vegetation, either bare soil or built-up and outliers (Baraldi, 2019). For more information on the SIAM™ software see Baraldi et al., 2018a, 2018b.

4.3 Applying the LIVID approach

With all images loaded into the application and the selected subset, the reporting unit had to be defined. For this experiment, squares with a scale of 25 pixels were chosen. The size of one reporting unit equals hereby 62,500 m². With these dimensions, the area of AOI1 consists of 2132 cells, the one of AOI2 of 405 cells. On the eastern and southern edges of the imagery, these cells are smaller due to space constraints.

Next, the classes were defined. In this experiment, the pre-defined classes, mentioned in chapter 3.3, were used to group the classes resulting from the SIAM classification. Table 2 shows the groupings and attributed weights.

CLASS IN LIVID APPLICATION	SIAM-CLASS(ES)	WEIGHT
HIGH LAI VEGETATION	1 to 6	0.7
LOW LAI VEGETATION	7 to 12	0.5
BARE SOIL/BUILT-UP	13 to 19	0.1
WATER	21 to 24	0.2

Table 2: Classes for experiment together with weightings

The weights were higher for the two vegetation classes, since the focus of the project laid on changes in vegetation. A change from or to the vegetation classes had far more effect on the NRI values than changes between the vegetation classes themselves, or between the other classes. With the weights and the reporting units, the “natural resource index” (NRI) could now be calculated for every unit. However, before the calculation was started, the newly implemented NoData-threshold was set to 100%, so that every level was accepted in the process. The percentage of area one class made up per reporting unit was multiplied by its corresponding weight. These weights and class composition lack expert knowledge on the topic of forest fires and the case study area analysed. With more knowledge in these specific fields, the later results might have been enhanced significantly. More differentiated classes could have been created, with more fitting weights. In a second step, the different classes were added up, thus forming the NRI of the individual cells. The NRI formula hence went as follows:

$$NRI_{cell} = \sum (\% \text{ Area of Class in cell} * \text{Weight of class})$$

The NRI results for every timestep were exported and loaded into the “ArcGIS Pro” software. Besides, NDVI and NBR values were calculated. All the resulting layers were exported as shapefiles with index values per reporting units. Before any of these shapefiles could be compared, the individual index values per reporting unit had to be standardized, as the results of the three indicators were on different scales and had different distributions. The so-called “z-scores” of the original values were calculated per reporting unit and indicator layer. A “z-score” expresses a value’s distance in standard deviations from the mean of its corresponding data set. The transformed values have a mean of 0 and a standard deviation of 1 (Hervé, 2007). To calculate these “z-scores”, the following formula was applied:

$$Z - score = \frac{Value - Mean}{Standard Deviation}$$

Source: Hervé, 2007, p. 1057

The subtraction of the mean per value centred the distribution, while the division by the standard deviation normalized it (Hervé, 2007). To facilitate this step, a Python script was written, which was then used in a custom ArcGIS Pro tool. The script had a table with the “z-scores” as output, which was then joined with the corresponding shapefile, all through the model builder. Figure 28 and Figure 29 show compilations of the 36 shapefiles generated in total for both AOIs.

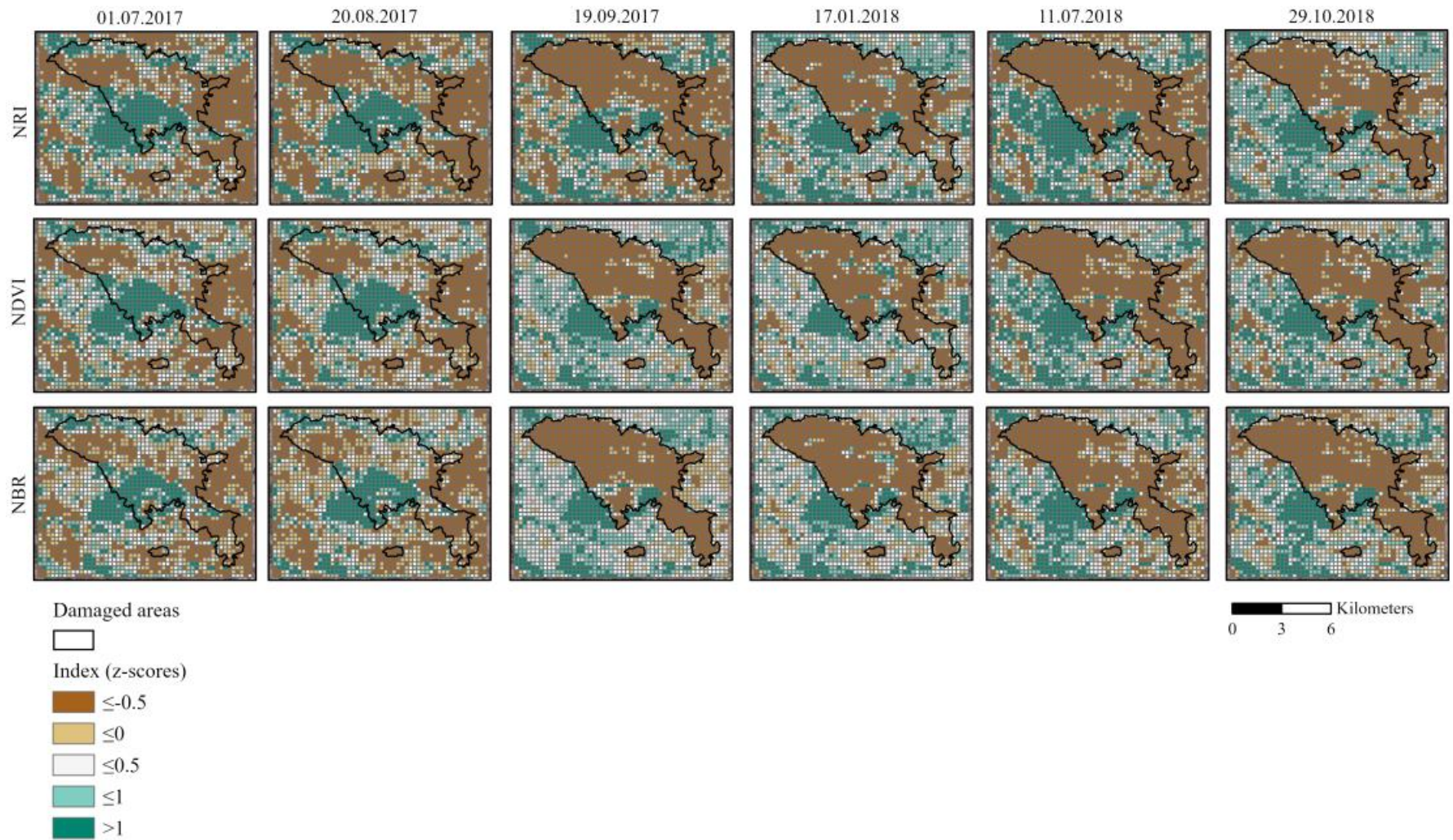


Figure 28: NRI, NDVI and NBR z-scores for AOII (contains modified Copernicus Sentinel data 2017, 2018, scale: 1:300,000)

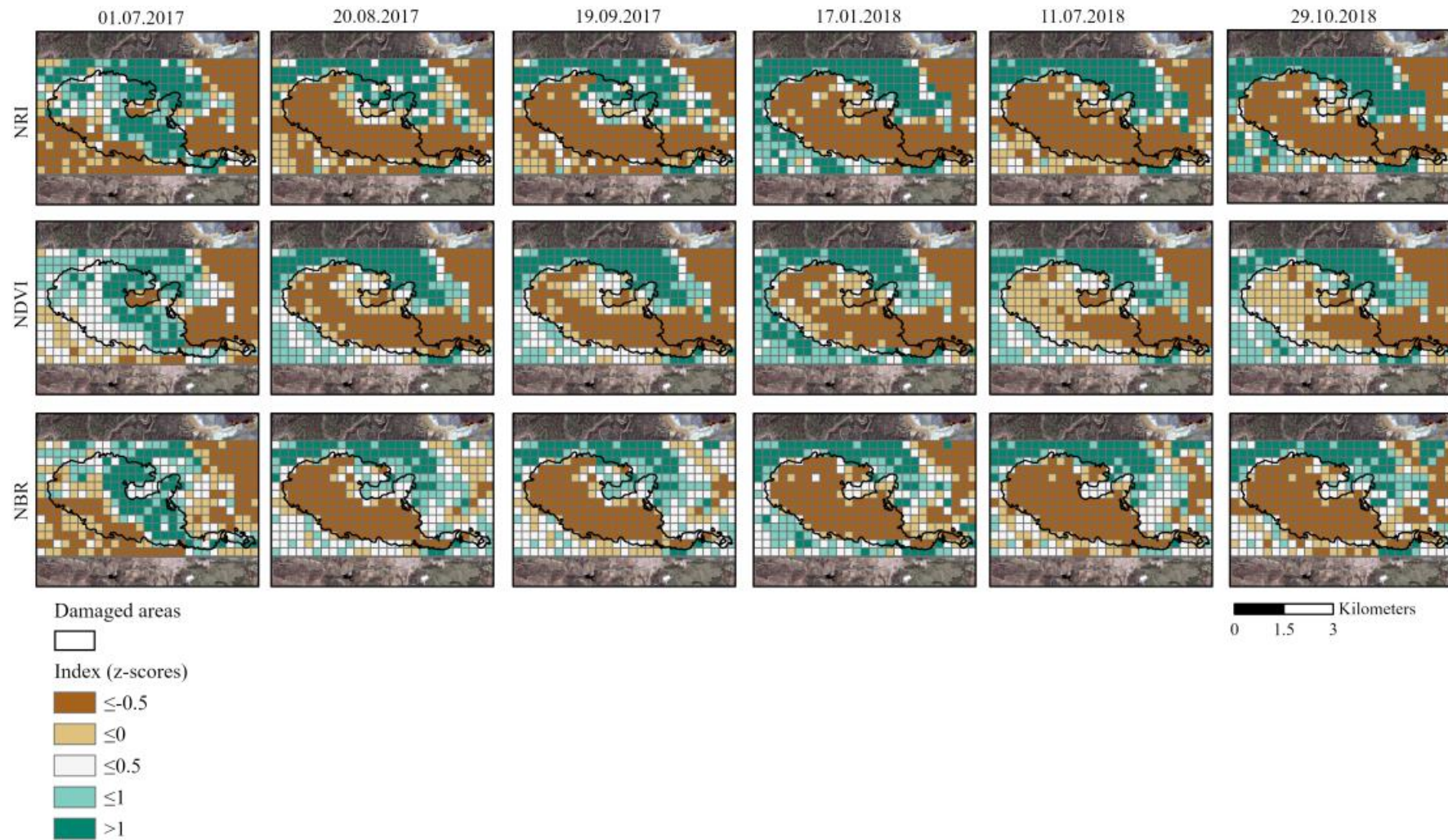


Figure 29: NRI, NDVI and NBR z-scores for AOI2 (contains modified Copernicus Sentinel data 2017, 2018, scale: 1:150,000)

A decline in the three index values immediately after the burn events for both AOIs (AOI1: after 20.08.2017, AOI2: after 01.07.2017) was observable. The NDVI values dropped within both AOIs after the fires inside the affected areas but were increasing within the AOIs again in the later pictures. The regions outside the damaged areas retained higher values throughout the investigation period. The drop in NBR values confirmed an occurrence of fires in the affected regions. The NRI values also showed a decreasing trend in those areas, in contrast to the areas which were not affected by the forest fires. It must be noted, however, that some cells in the affected areas in AOI1 managed to retain high values for all three indicators. All in all, a similar trend between the three indicators was observable when visually analysing the AOIs. In addition, a strong reduction of seasonal effects within the damaged areas is noticeable after the fires when compared to the trends in the unaffected areas.

The cells inside of the damaged areas must be analysed separately from the ones outside of them. In analogy to the “ESMN-060”-report both AOIs were split into affected and unaffected areas. This was again accomplished utilizing the “damaged areas” shapefile from the “EMSN-060”-GDB (Utanda, 2019). In “ArcGIS Pro” the affected and unaffected datasets were compiled using the “Clip” and “Erase” tools based on the NRI, NDVI, and NBR shapefiles, and with the aid of the “damaged areas” shapefile from the EMSN-060-report. To avoid that the cells on the border of the “damaged areas” shapefile are counted in both areas, these were selected with the “Select Layer By Location”-tool and deleted in the unaffected datasets. The “Model Builder” helped to design a process to automate this workflow. Figure 30 shows the extent of both areas in both AOIs.

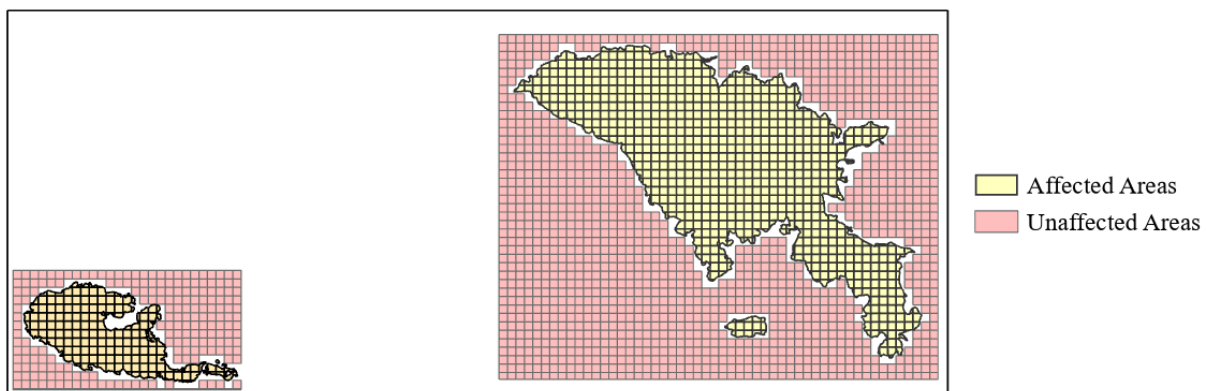


Figure 30: Affected and unaffected areas (scale 1:150,000)

By splitting up these shapefiles, the number of datasets doubles to 72. For further statistical evaluation, the “Table to Table”-tool was used to generate tables of all shapefiles. These tables were subsequently exported via the “Table to Excel” tool. This step could have been partly skipped by merging all shapefiles for one area and indicator via the “Union”-tool. The results would have been one “super shapefile” per area and indicator, including all timestamps, which could then have been exported into Excel.

To round off the visual interpretation of the indicator's development over the analysis, a quantitative analysis followed. The idea behind this was to follow the approach of the EMSN-060 report in its comparison of the mean values of the indicators per timestep divided into affected and unaffected areas (Utanda, 2019, p. 16). The goal is to assess if there are differences between affected and unaffected areas in the development of the indicators over time. To do this, the mean of all original cell values per timestamp and indicator was taken. As the indices were on different scales, the percentage change from their starting values were calculated. Therefore, the indices' means of the following timesteps were divided by the mean value of the first timestamp and multiplied by 100. The results, split between affected and unaffected areas, are depicted in Figure 31 and Figure 32 for AOI1 and in Figure 33 and Figure 34 for AOI2.

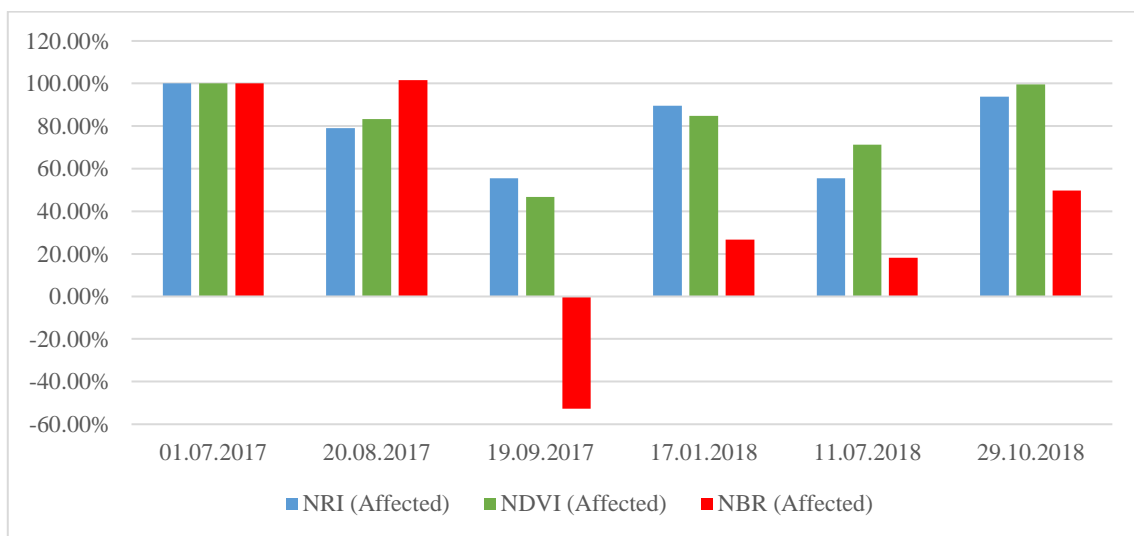


Figure 31: AOI1 - affected areas: percental change of mean indices (base: 01.07.2017)

Considering the affected areas of AOI1 depicted in Figure 31, the development of the three indicators is similar: after the fire events between the 8th of September and the 10th of September 2017, a drop in all indicator values was noticeable. The sharpest drop was observable for the NBR index, with a decrease of 150%. The index dropping below zero served as an indication for a fire in the area. The NRI dropped to 55% and the NDVI to 46%. After this, all indices began to grow again. Additionally, seasonal variations were noticeable for all indices in the form of higher values in winter and autumn, and lower values in summer. NRI and NDVI even almost managed to reach their starting values before the fire of 01.07.2017, on the 29th of October 2018 (NRI: 93.11%, NDVI: 99.71%). It must be noted that the trend of the NRI and the NDVI indices were similar. One cause of this was the high weighting of vegetation classes when calculating the NRI.

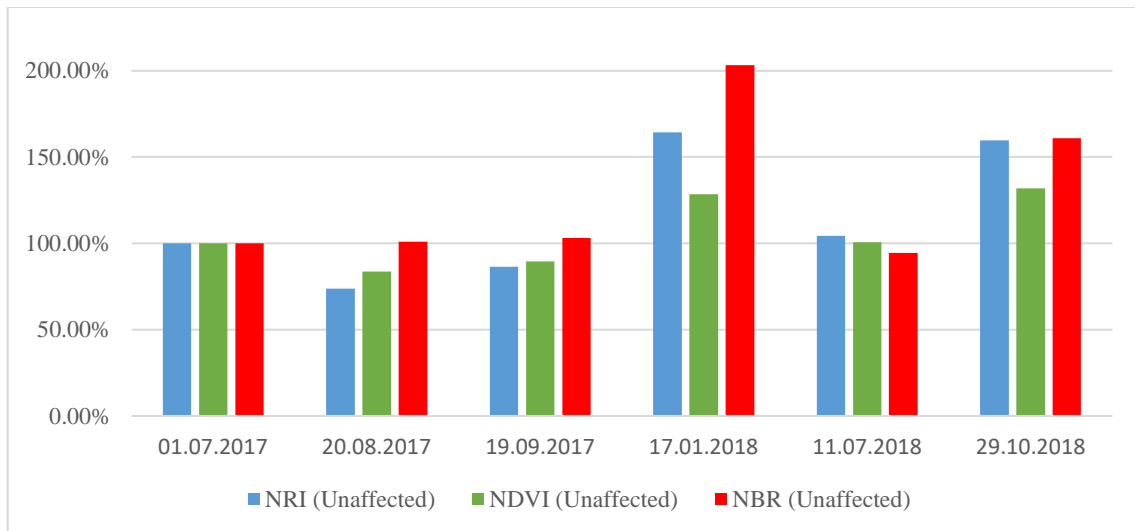


Figure 32: AOI1 - unaffected areas: percental change of mean indices (base: 01.07.2017)

Seasonal activity was noticeable in the unaffected areas of AOI1 (see Figure 32). NRI and NDVI slightly decreased on the imagery taken in the summer months of 20.08.2017 and 19.09.2017, characterized by low participation and high temperatures (see Figure 24), while the NBR grew slightly. The January imagery, 17.01.2018, showed a growth in all indices, due to higher participation and lower average temperatures (see Figure 24). The NBR had the strongest increase compared to the first picture with 103%, NRI grew by 64% and NDVI by 28%. The indices declined to their initial values in the 11.07.2018 imagery, before exceeding them again for the final timestamp. Figure 32 gave an adequate picture of the seasonal changes in the AOI without the interruptions a fire event causes. Especially the 17.01.2018 and 29.10.2018 imagery showed high growth in all indices, which also applied to the affected areas.

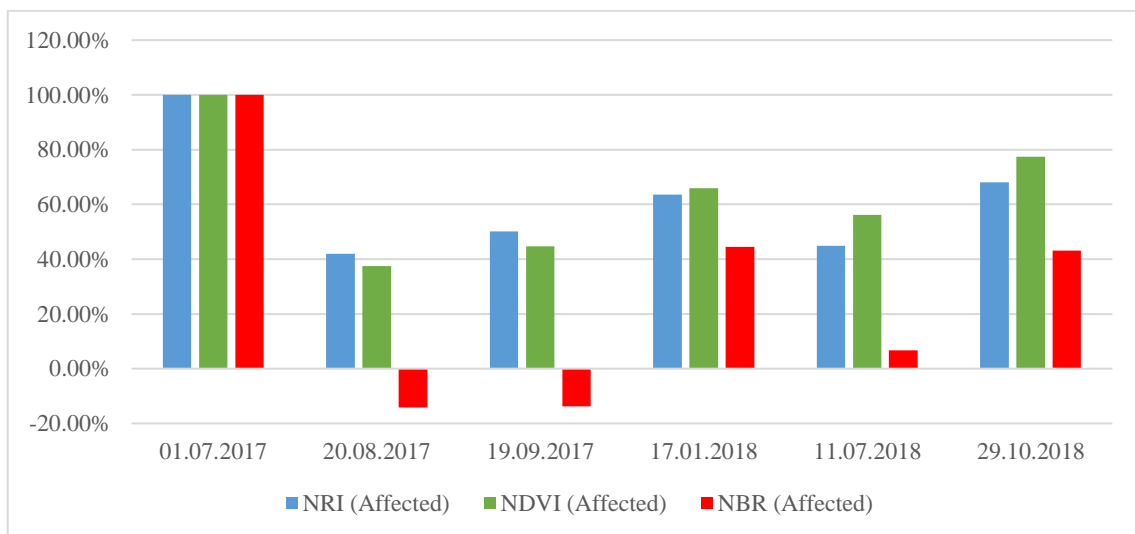


Figure 33: AOI2 - affected areas: percental change mean indices (base: 01.07.2017)

Figure 33 shows the development of the indices for the affected areas. The fires raged a bit earlier in this AOI, from the 3rd of July to the 5th of July 2017. A drop in all indices was therefore seen in the

20.08.2017 timestamp. The NBR values again had the sharpest drop with 114%, followed by NDVI with 72% and the NRI with 58%. Unlike the development of the indices in the affected areas of AOI1, the growth after the fire was weaker here. The NBR values even stagnated at their lowest value, growing again in the 17.01.2018 imagery. Moreover, none of the indices reached their initial values in this case: in the imagery of the 29.10.2018, the NDVI reaches 77%, the NRI 68%, and NBR 47% of their values of the 01.07.2017.

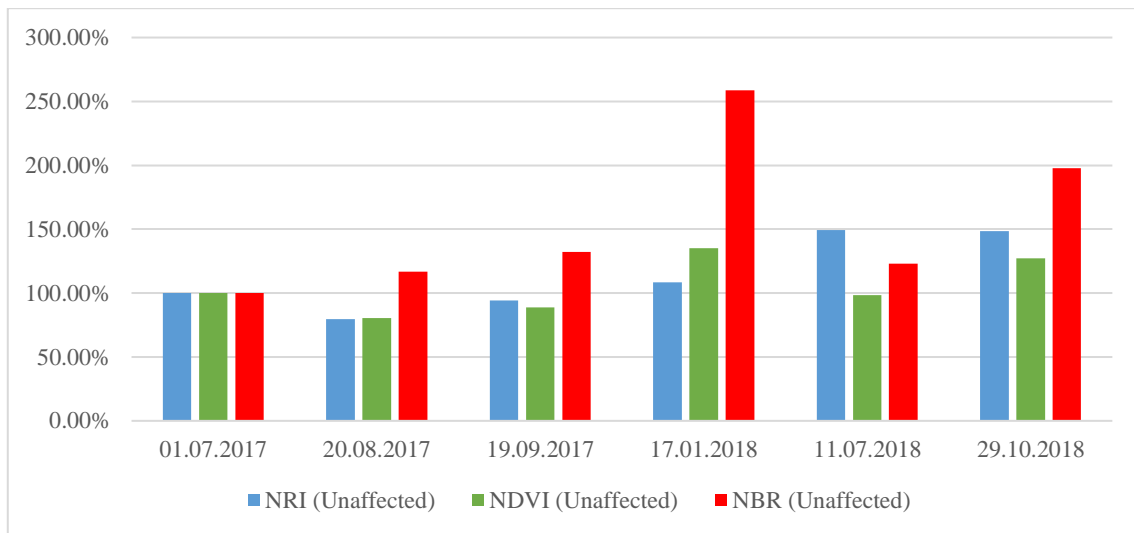


Figure 34: AOI2 - unaffected areas: percental change mean indices (base: 01.07.2017)

The trends of the indices in the unaffected areas of AOI2 are depicted in Figure 34. Like in AOI1, the NRI and NDVI values declined on the 20.08.2017 and 19.09.2017 images, while the NBR grew. All indices can register growth over their initial values in 17.01.2018 picture, though, the NBR had by far the highest growth with over 150% in this AOI. Again, weather conditions could have led to these occurrences. Compared to AOI1, the trend changed after these images for AOI2: instead of declining in the Summer of 2018, the NRI continued to grow and the NDVI fell back to its initial value, while the NBR declined compared to the value of the previous picture, but was still higher than its initial value. The processes behind these occurrences were not examined in this work. Then again in the 29.10.2018 image, we saw a similar picture as in AOI1: the indices were higher than their initial values, presumably due to more favorable weather conditions for vegetation growth in Autumn. In AOI2, the affected areas had slower growth in the indices compared to AOI1. In the unaffected areas, however, the 17.01.2018, 11.07.2018, and 29.10.2018 images are characterized by high values in all indicators.

The AOIs have similar trends in both affected and unaffected areas. While the graphs on the affected areas lead to a better understanding of how the indices develop after a fire, the unaffected areas' graphs showed the seasonality of the region and offered a basis for comparison. Combining the trends of the indices in affected and unaffected areas, showed how the fire disrupts the seasonal trends in an AOI. Figure 35 shows all indices in AOI1.

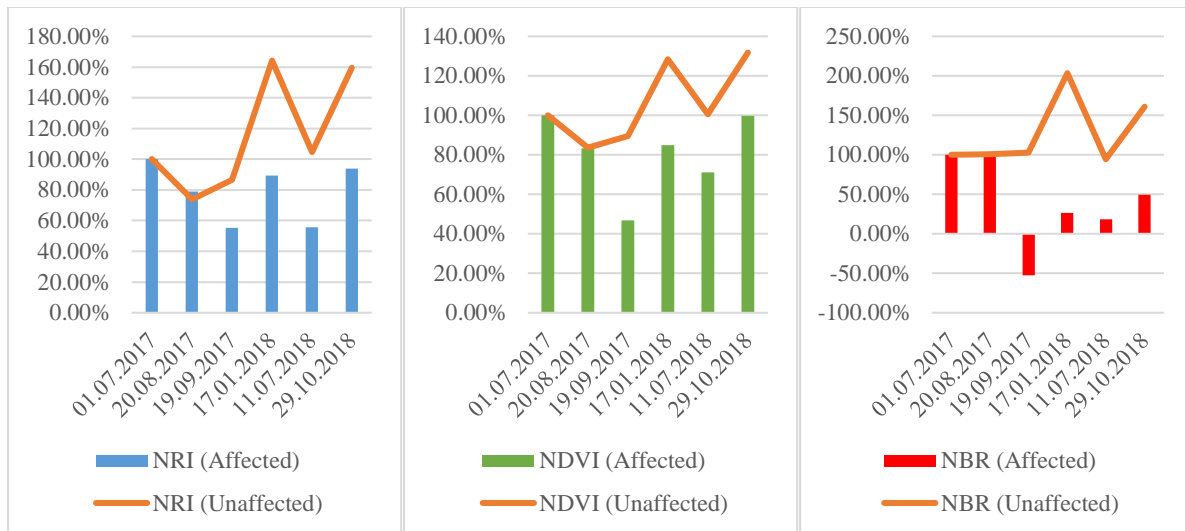


Figure 35: AOI1 - percentage change of all indices in affected and unaffected (base date: 01.07.2017)

Comparing the curves of the unaffected areas and the bar charts of the affected areas, the same trends were identifiable for AOI1, if the fire events are excluded. This similarity speaks for the occurrence of seasonal fluctuations, which not only exist in those areas unaffected by the fires but also continued to play a role after the fire events in the areas affected by them. To complete this overview, the same charts are given for AOI2 in Figure 36.

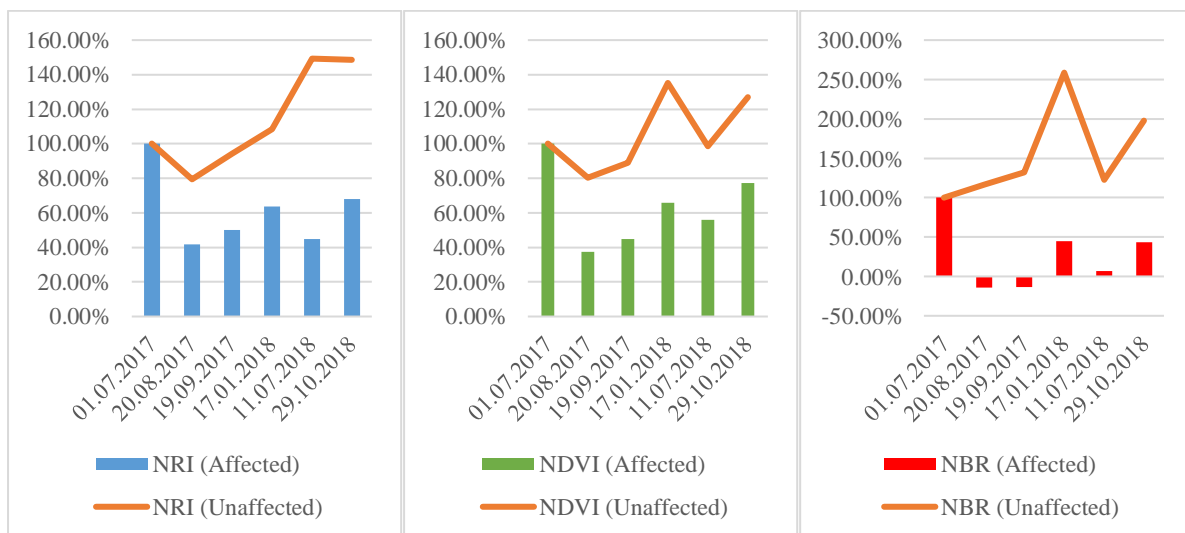


Figure 36: AOI2 - percentage change of all indices in affected and unaffected (base date: 01.07.2017)

For AOI2, similarly to AOI1, a resembling development between affected and unaffected areas for all indicators can be observed. While in the summer months values went down, they tended to go up in the autumn and winter months. As this was both noticeable for affected and unaffected areas, seasonal fluctuations on the indices were possible reasons.

A further insight given by this comparison is, as one could have expected, that the indices were developing quite similar in both AOIs for the unaffected areas. The NDVI and NBR almost had the

same course of the curve, while the NRI showed some differences between the AOIs in the second half of the time series.

Figure 37 illustrates the mean “z-score difference” between image pairs, for all indices per cell. This is done in analogy to the methodology of the “depletion index” by Braun and Hochschild (see Braun and Hochschild, 2017, p. 9). The following formula is applied with the help of the raster calculator in ArcGIS Pro:

$$\text{Mean } z - \text{score difference} = \frac{1}{n} \left(\sum_{n=1}^i z_i - z_{i-1} \right)$$

Where n is the number of timestamps and z_i is the z-score at the timestamp i.

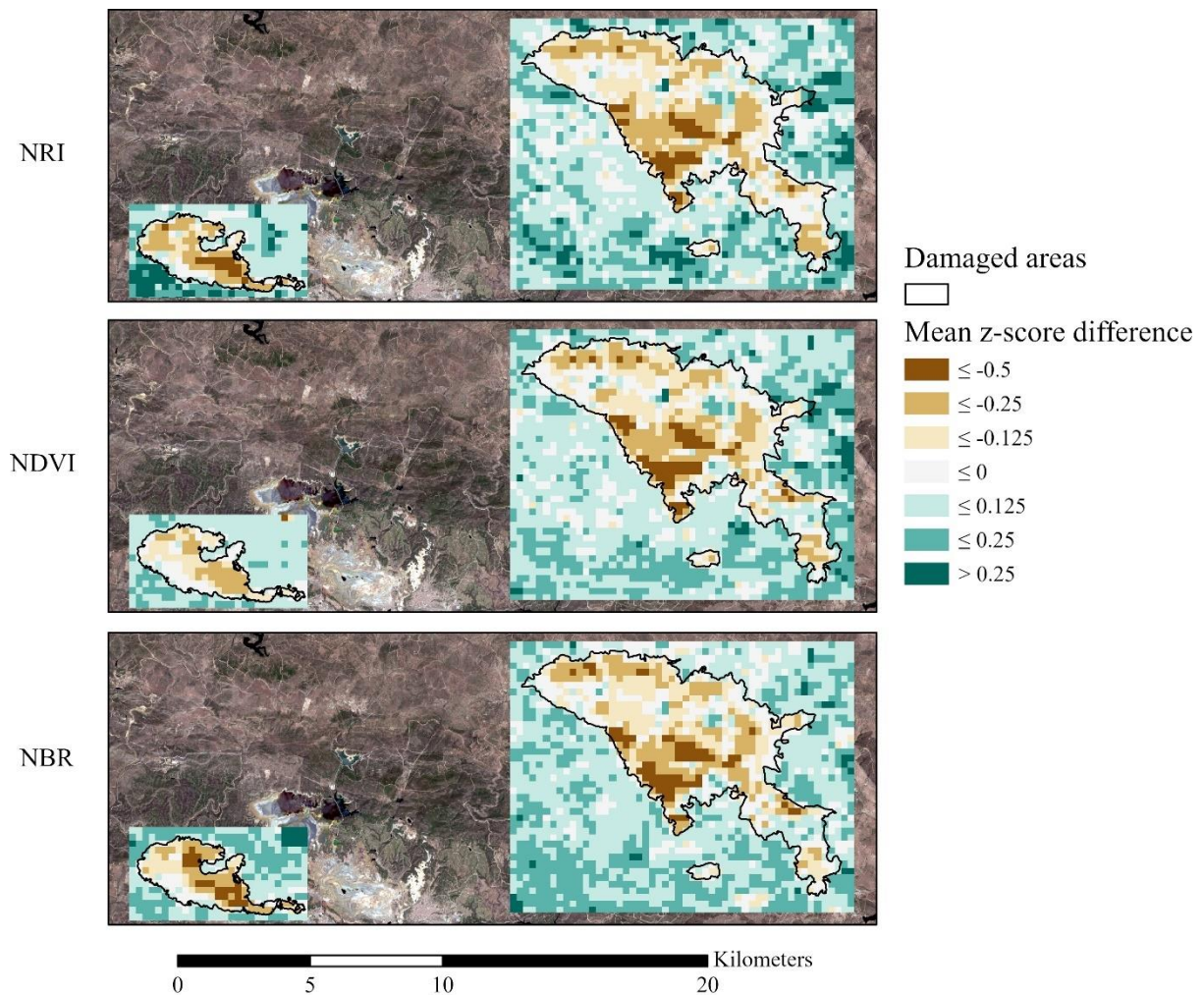


Figure 37: Mean difference in z-score values for all indices (base map: Copernicus Sentinel data 2017, contains modified Copernicus Sentinel data 2017, 2018, scale: 1:200,000)

Even if some discrepancies exist between the different indices, it can be said that on the one hand, cells with a negative mean z-score change were concentrated in the damaged areas, while on the other hand, cells with a positive mean change were mostly detectable outside of these areas. These overview maps thus combined the index value maps (Figure 28 and Figure 29) with the index change graphs and give

at last a concluding overview over the change occurring in the individual cells, before moving on to the next chapter, in which the variability results are analysed.

4.4 Variability

After having analysed the individual results of the indices per timestamp in-depth, their overall variability is discussed. Besides the separate index values per cell and timestamp, the LIVID application is also capable of calculating the variability value for the three indicators over the time frame of the analysis. The variability values were calculated per cell, resulting in a single dataset per AOI. The variability was calculated with the following formula, already referred to in the methodology chapter:

$$Variability (NRI) = \frac{\sum \sqrt{(NRI_t - NRI_{t-1})^2 + \left(\frac{T_t - T_{t-1}}{T_n}\right)^2}}{\sqrt{(NRI_n - NRI_0)^2 + \left(\frac{T_n - T_0}{T_n}\right)^2}}$$

The resulting shapefiles were exported and visualized within ArcGIS Pro. The areas affected by the forest fires were overlaid over the variability raster in Figure 38. The shapefile depicting the damaged areas was again taken from the EMSN-060 report (Utanda, 2019).

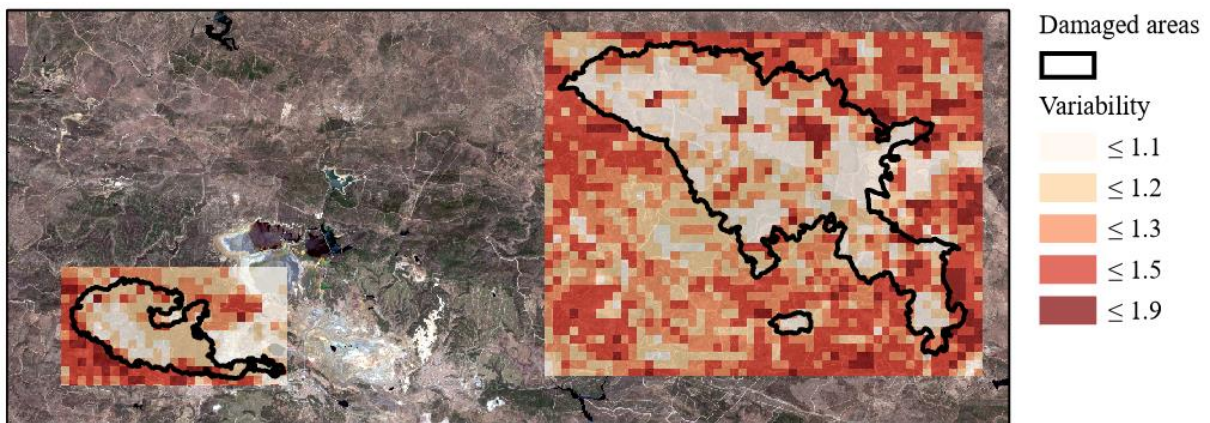


Figure 38: NRI variability raster with damaged areas overlaid (base map: Copernicus Sentinel data 2017, scale: 1:200,000)

For both AOIs, the variability was on a first look higher in the unaffected areas than in the affected ones. Still, some hotspots with higher variability existed in the affected areas, especially in AOI1. This strict difference between affected and unaffected variability zones spoke against a random distribution. The next step was the calculation of variability values of NDVI and NBR. With the advancement of the LIVID application, these values were calculated in the same fashion as the NRI values. The results are visualized in comparison to the original NRI variability in Figure 39.

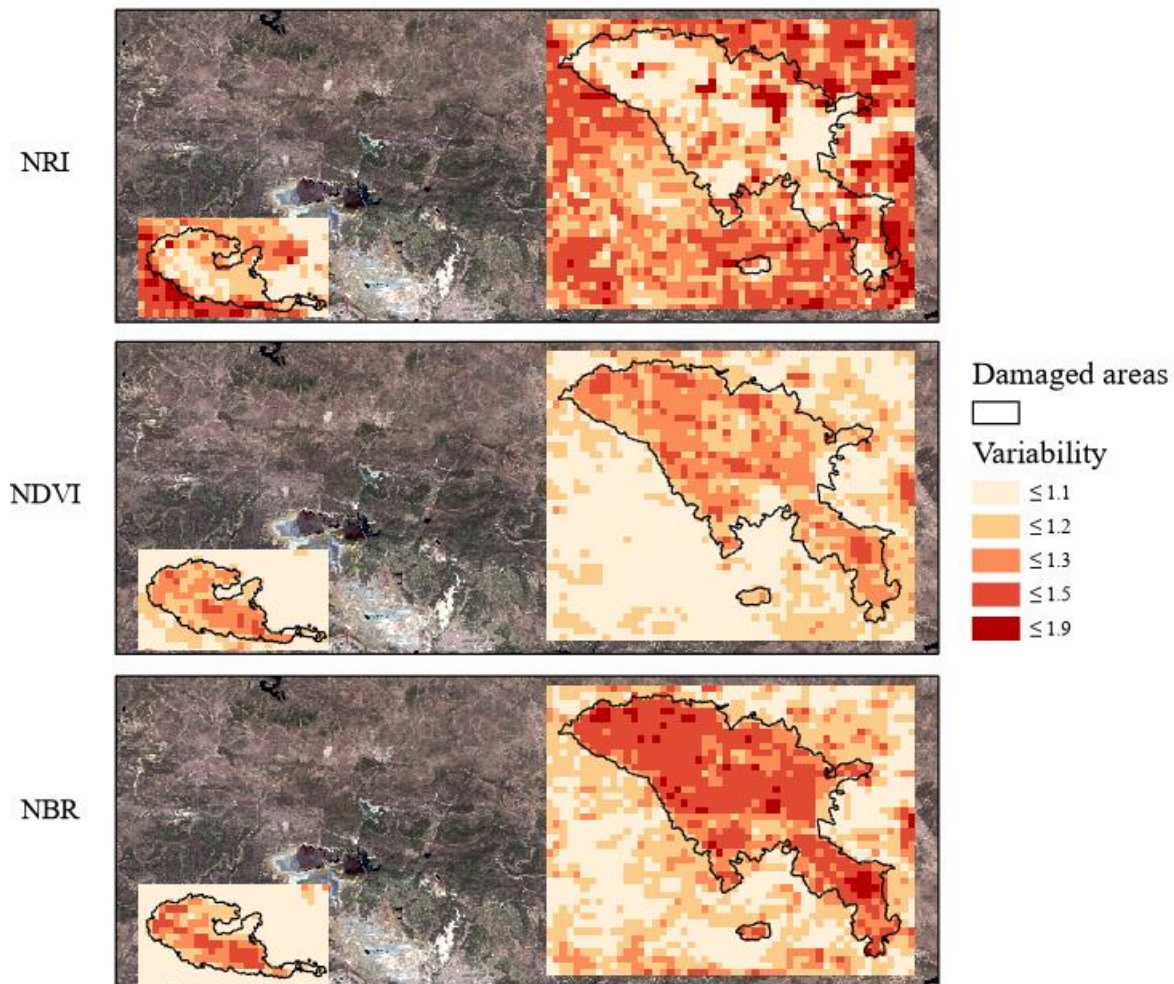


Figure 39: Variability rasters for NRI, NDVI, and NBR (base map: Copernicus Sentinel data 2017, contains modified Copernicus Sentinel 2 data 2017, 2018, scale: 1:200,000)

A visual interpretation of the graphs in Figure 39 made it apparent, that the higher variability values for the NDVI and the NBR were confined within the damaged areas. Whereas, the unaffected areas showed a lower amount of reporting units with high variability values. This was striking in comparison to the NRI variability, which showed a different picture, as explained above. We must keep in mind, that the NRI indicator, different from the NDVI and NBR, included a weighting process. The high weights for “High LAI vegetation” and “Low LAI vegetation” in this test run meant that conversion for example from a “bare soil/built-up” object (weigh 0.1) to a “High LAI vegetation” object (weigh 0.7) caused a difference in weighting of either +0.6 or -0.6. This had a considerable effect on the NRI index values, and therefore on the variability value of a cell. Change effects from and to vegetation classes may, therefore, had a stronger effect on the NRI values than on those of the other indicators.

To supplement this first qualitative analysis with a quantitative one, the different tables were exported, and the cells were grouped via Excel in the same variability classes as in Figure 39 above (class 1: variability lower or equal to 1.1, etc.). Then, the number of cells corresponding to the individual classes was determined per AOI, again split by unaffected and affected areas. The relative representation of these numbers can be found in a stacked column chart in Figure 40.

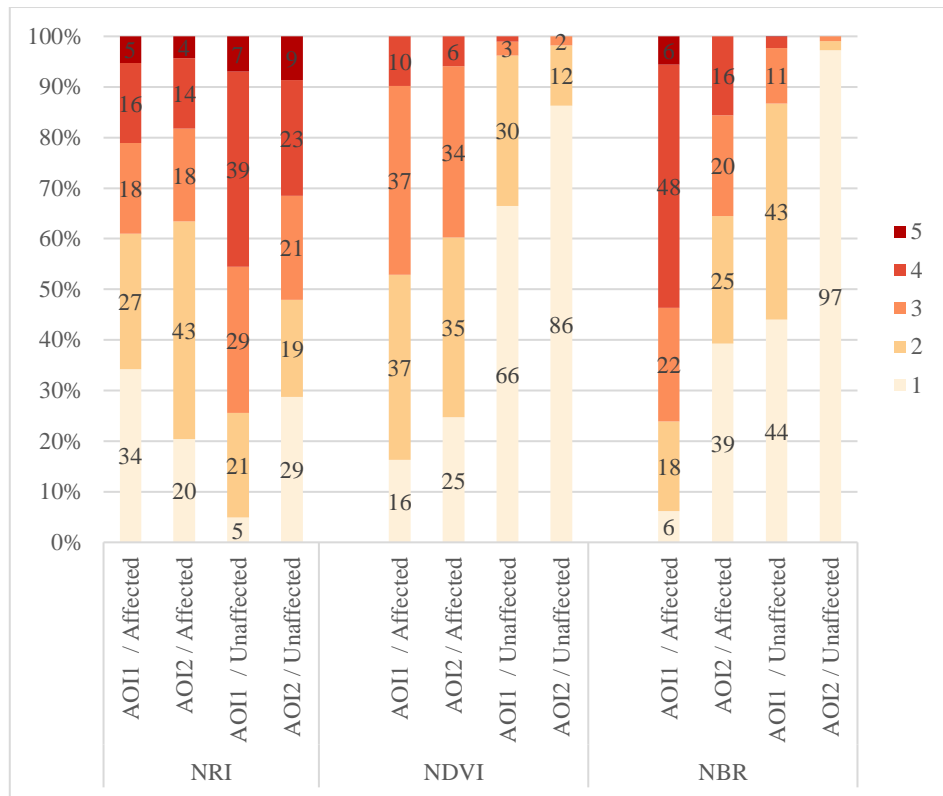


Figure 40: Stacked column chart of the relative spread of variability classes over AOIs and areas, with data labels

The earlier visual analysis was confirmed by these numbers. For the NDVI and NBR indicators, the percentage of low variability cells was higher in unaffected areas than in affected ones. For the NBR, the percentage of cells corresponding to variability class 1 in the unaffected areas was 44% for AOI1 and even 97% for AOI2. These percentages were much lower in the affected areas, where their percentage is 6% for AOI1 and 39% for AOI2. The NDVI drew a similar picture: here the percentage of class 1 cells is 66% in AOI1 and 86% for AOI2 in unaffected areas, while 16% for AOI1 and 25% for AOI2 in affected areas.

While the low variability cells had a higher portion in unaffected areas compared to the affected ones for these indicators, the high variability cells' share showed the opposite development: if variability classes 4 and 5 are the counted as the high variability cases, their shares in unaffected areas for the NBR are at 2% for AOI1 and 0% in AOI2, while in affected areas they are at 54% in AOI1 and 16% in AOI2. For the NDVI indicator, these results were less conclusive but still: while the shares of high variability cells are at 1% for AOI1 and 0% for AOI2 in unaffected areas, they were at 10% for AOI1 and 6% for AOI2 in affected areas.

For the NRI the picture was not as clear-cut. For AOI1, the share of cells in variability class 1 was higher in the affected areas (34%), than in the unaffected areas (5%). At the same time, the share of cells in the high variability classes of 4 and 5 was higher in the unaffected areas (46%), than in the affected ones (21%). For AOI2, the share of cells in class 1 was this time lower in the affected areas

(20%), than in unaffected ones (29%). The share of cells in classes 4 and 5, was higher in unaffected areas (32%), than in affected ones (18%).

After having compared the variability values per index, the causes behind the differing distributions between NRI on the one side, and NDVI and NBR on the other, were investigated. The previous subchapter concluded with an overview of the mean z-score difference of each cell. Combining this overview with the raster of variability values per cell, offered a way of gaining new insights, concerning the different distributions. Figure 41 illustrates the results of this procedure.

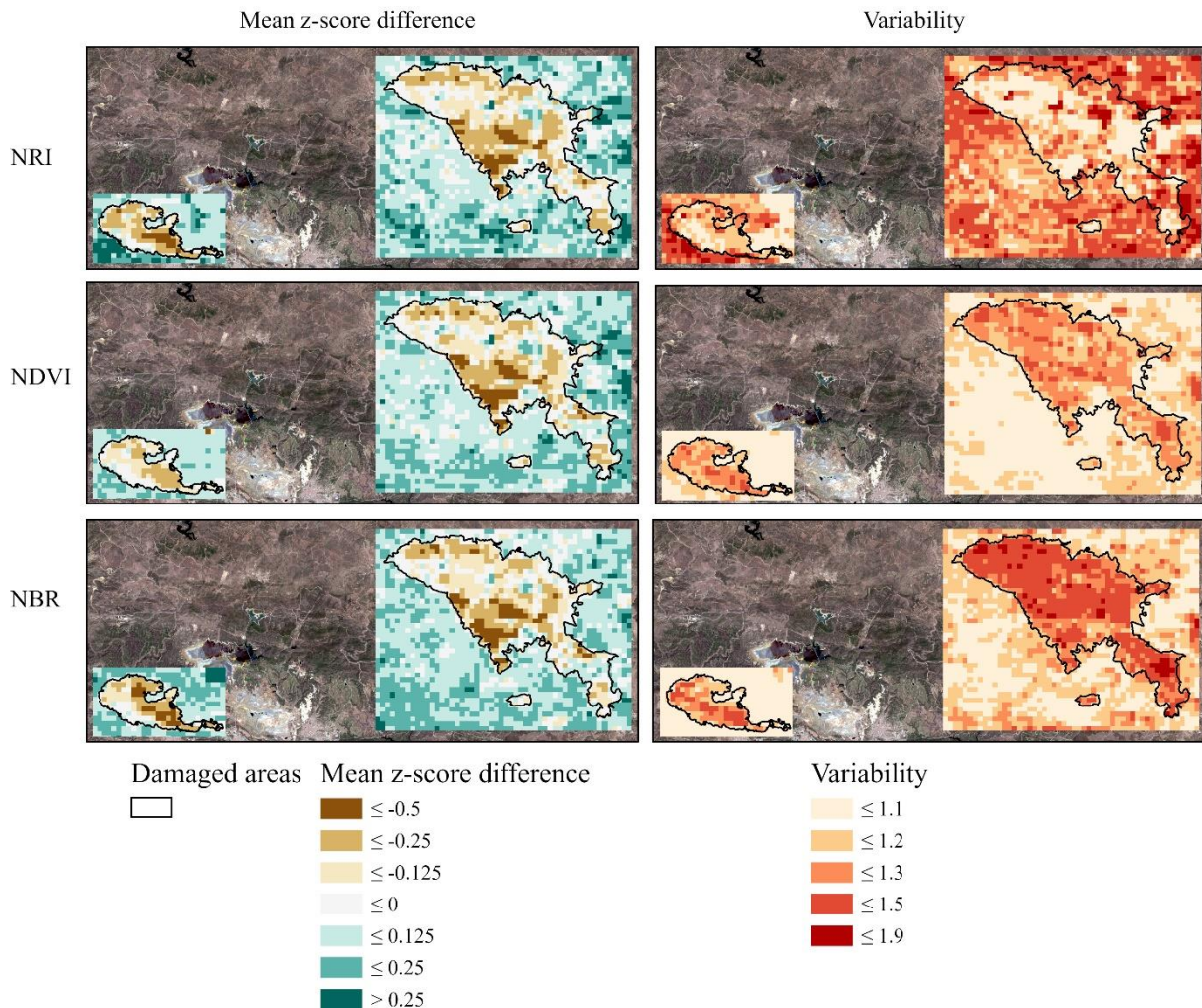


Figure 41: Comparison of mean z-score difference and index variability (base map: Copernicus Sentinel data 2017, contains modified Copernicus Sentinel data 2017, 2018, scale: 1:250,000)

For the NDVI and especially for the NBR index, cells within the damaged areas tended to have high variability values and negative z-score differences. In the case of the NRI index, this trend was reversed: here, cells with high variability values were outside of the damaged areas and tended to have a positive z-score difference. To analyse these distributions further, both rasters were overlaid. Variability and z-score difference classes were applied once again. This resulted in five variability classes and seven z-score classes, grouped in the same way as the mean z-score difference and variability values were grouped in the legends of the maps depicted in Figure 41. Via the “Tabulate intersection”-tool in ArcGIS

Pro, the percentage of the z-score difference classes per variability class was calculated for both AOIs. The results are the graphs depicted in Figure 42 and Figure 43.

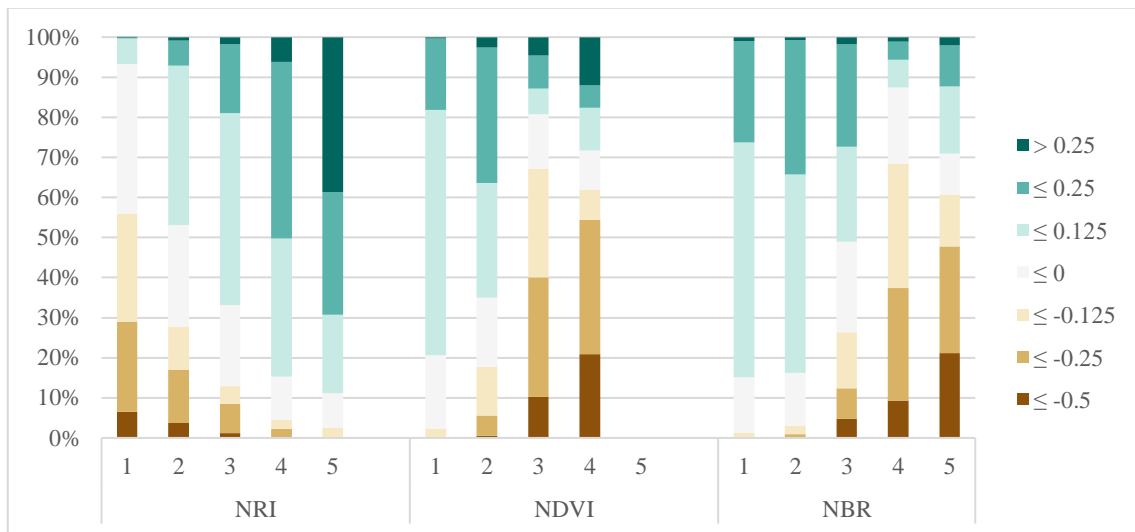


Figure 42: AOII - Stacked bar chart of distribution of mean z-score difference per variability class

In the case of the NRI, a higher variability class entailed a larger share of cells with a higher positive z-score difference. The share of cells with a mean growth in NRI z-score higher than 0.25, was at only 0.06% for variability class 1 and at 38% for variability class 5. At the same time, the share of cells with a mean NRI z-score decrease of -0.5 dropped from 6% for variability class 1 to 0% in variability class 5. These trends were likewise noticeable for the other positive or negative z-score differences.

For the NDVI and NBR, the inverse development was noted: here the share of highly negative z-score difference values grew with the variability class. For the NDVI, the share of cells with a mean z-score difference of -0.5 was at 0% for variability class 1, while it was at 20% for variability class 4. As the variability values were generally a bit lower as for the other indices, no cells are classified into the fifth variability class. It must be stressed, that the development of the NDVI was not as clear-cut as it was for the NRI. Still the overall share of cells with a negative z-score difference grew with an increasing variability class, growing from 20% in variability class 1 to 70% for variability class 5. NBR offered a similar picture: while there were no cells with a negative z-score difference below -0.5 in variability class 1, 21% of the cells had such a z-score difference in variability class 5. The overall share of cells with negative mean z-score difference grew from around 15% in variability class 1 to around 70% in variability class 5.

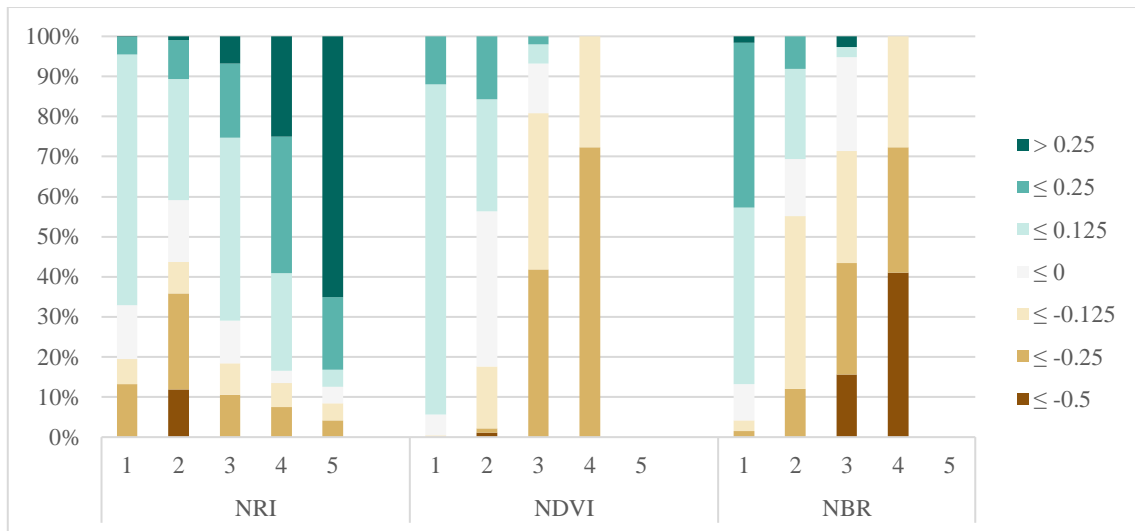


Figure 43: AOI2 - Stacked bar chart of distribution of mean z-score difference per variability class

The same trend already identified in AOI1 was also recognizable in AOI2 for the NRI: the share of positive difference values grew with a higher variability class, at the same time as the share of decreasing index values sank. The marginal share of 0.1% of the highest increasing z-score differences in variability class 1 grows to 65% in variability class 5. The developments for the other two indices were even more pronounced compared to AOI1: the share of cells of negative z-score differences was growing with the variability of these cells, reaching 100% for the NDVI at variability class 4 and the NBR at variability class 5.

Thus, the same trends are observed in the two AOIs for all indices. Two general conclusions can be drawn from this: first, increasing variability went hand in hand with a growth of z-scores in the case of the NRI. Second, increasing variability for the NDVI and NBR indices meant a decrease in z-scores. The next point is to find the cause behind these reversed variability trends.

The first assumption would be, that the fire event did not have such a strong impact on the NRI values, as it had on the values of the other indices. A second assumption was that the drop in NRI values through the abrupt change event of the forest fire, created less variability relative to the seasonal vegetation change through the high weighting of the vegetation classes in our experiment.

To verify the first assumption, the raster calculator was used to calculate the difference of z-scores between the images before and directly after the fire events. For AOI1 the last date before the fire was 20.08.2017 and the one directly after the fire was 19.09.2017. For AOI2, the first image, 01.07.2017, was the one before, and the 20.08.2017 the one after the fire. Figure 44 depicts the addressed z-score differences per cell for all indices.

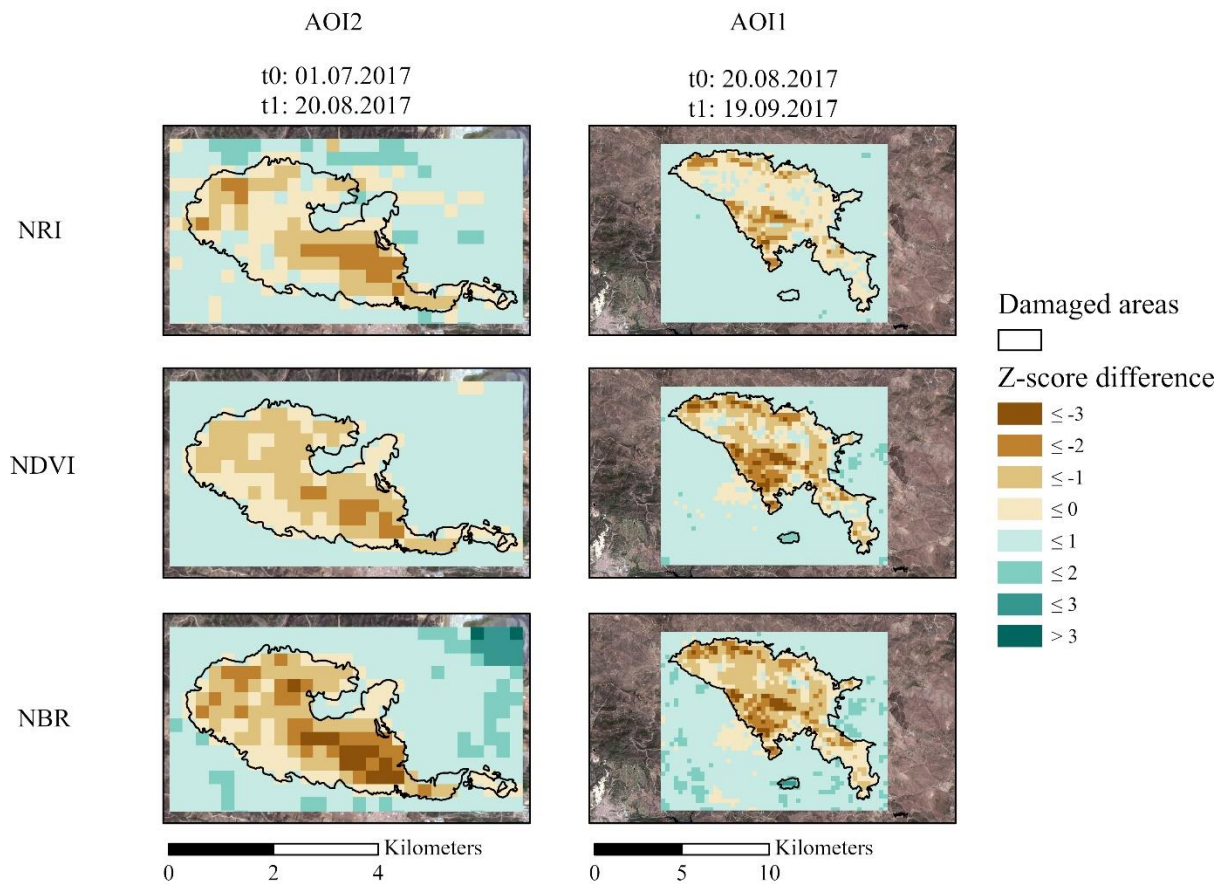


Figure 44: Z-score differences ($t_1 - t_0$) of all indices for both AOIs (base map: Copernicus Sentinel data 2017, contains modified Copernicus Sentinel data 2017)

For the NBR and NDVI indices, a more comprehensive distribution of cells with negative differences was noticeable in comparison to the NRI. For AOI2 the disparity was more obvious: inside of the damaged areas, no cells with a positive z-score difference were detectable for NDVI and NBR, while for the NRI at least some cells still showed growth in z-score values. For AOI1, the NRI z-scores differences were not as strongly negative as they were for the other two indices. In both AOIs, the NBR showed the highest number of cells with strongly negative z-score differences. These facts advocated for an overall milder impact of the fire on the NRI values. To verify these claims made by visual interpretation, the “Tabulate Intersection” tool was once again applied to find the shares of cells with increasing and decreasing z-scores directly after the fire event. Figure 45 shows these values, divided by affected and unaffected areas, for AOI1 and AOI2.

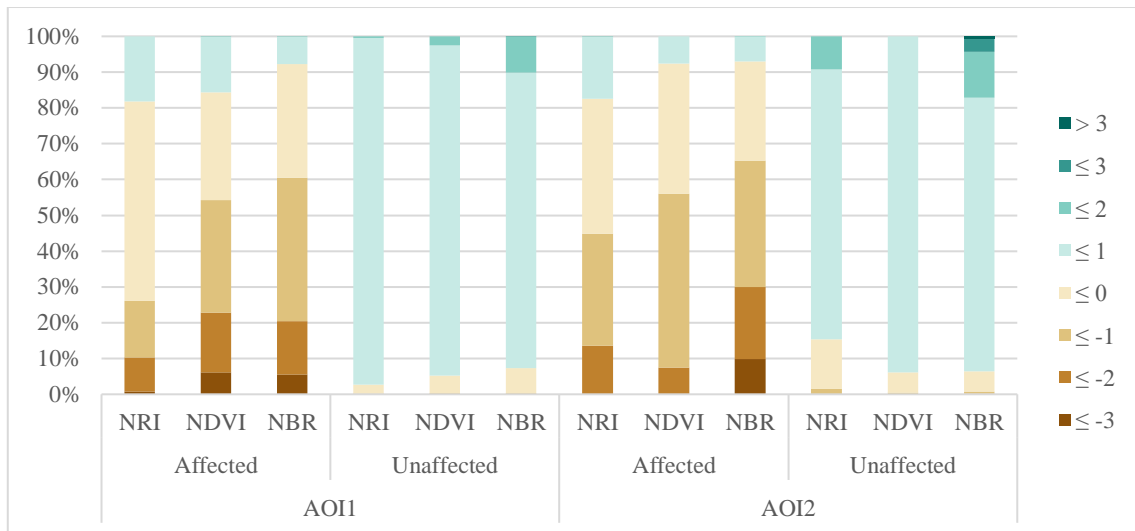


Figure 45: Intersection of z-score differences of the fire events and damaged areas for both AOIs

The values of Figure 45 corresponded with the first impressions of the visual interpretation of the share of negative z-score differences in the affected parts of the AOIs. In the affected area of AOI1, the share of negative z-scores for the NRI was 81% directly after the fire. For NDVI it is 84% and for the NBR 92%. The composition of this share differed between the NRI and the other two indicators: while the NRI had a share of 55% of cells that have a z-score difference between 0 and -1, less than 1% of its cells have a z-score difference below -3. For the NDVI and the NBR, the class between 0 and -1 was around 30% and therefore smaller than for the NRI. All other negative classes, however, had bigger shares compared to the NRI ones. The class grouping the cells below -3, was around 5% for both indices. The unaffected parts of this AOI are dominated by cells with a z-score difference between 0 and 1 for all indices.

AOI2 shows similar results: the share of cells with negative z-score differences in affected areas was 82% for the NRI, and 92% for NDVI and NBR. This time, the shares of cells between 0 and -1 were a bit closer together: 37% for NRI, 36% for NDVI, and 27% for NBR. The NRI and NDVI had no cells with values below -3. The NBR, however, has a share of 9% of such cells. The shares in the unaffected areas of this AOI were again dominated by cells with z-score differences between 0 and 1 for all indices. The NRI had a slightly lower share of negative z-score differences (around 10%) after the fire for both AOIs. For AOI1, the share of cells with a lower negative effect (values between 0 and -1) was 20% bigger than for the other indices. These abrupt change events had a considerable impact on the variability of the cells. After looking at these results, the overall significance of the events turned out to be somehow milder on the NRI values than on the values of the other indices.

Calculating the intersection between affected and unaffected areas proved to be a helpful tool in understanding how changes occur in the AOIs. Earlier in this chapter, Figure 28 and Figure 29 gave an idea of the development of the indices over time in the form of z-scores. These were visually interpreted, but the quantitative investigation could lead us to new insights on the second assumption. The “Tabulated intersection” tool was thus applied once again, to see the share of z-scores within affected

and unaffected areas. One more class was added to further differentiate between the values of the cells. Furthermore, the point of transition between negative and positive values was integrated for every timestamp as “0-point”. As explained above, a z-score describes the number of standard deviations a value is deviating from the mean of the data series (Hervé, 2007). Since the values were represented as such z-scores, this “0-point” represented the original mean of the integral AOI. This allowed a further interpretation of the distribution of values around this point. Figure 46 and Figure 47 show the results for affected and unaffected areas for AOI1, while Figure 48 and Figure 49 show them for AOI2.

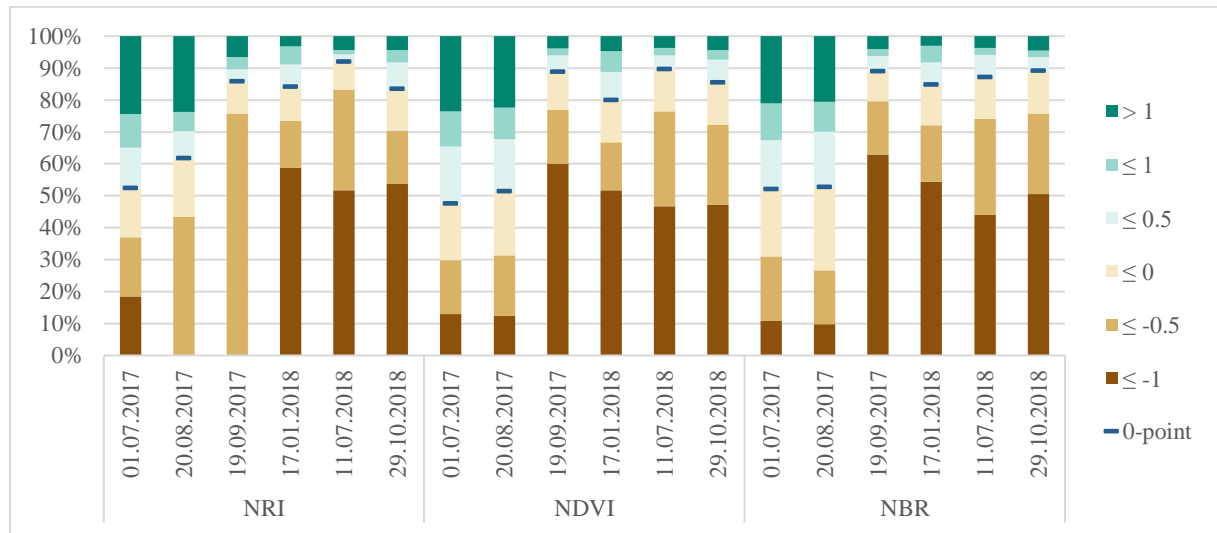


Figure 46: AOI1: Percentage of z-score class per index in affected areas (stacked bar chart)

Since the developments of the NDVI and NBR shares were quite similar and the processes behind were already analysed before (fire event, the return of seasonal fluctuations), they will not be discussed in detail at this point. The NRI development of the shares was, as expected from our previous analysis, differing from the ones of the other indices. The most obvious and for our analysis most interesting differences were: first, an increasing share of cells with negative z-scores before the fire event: from the first to the second timestamp, the share of reporting units with negative z-scores grew from 52% to 61%, all while their share for the other two indices stayed almost the same. At the same time, the share of cells with a z-score below -1 dropped from 18% to 0% for the NRI. This is especially interesting, as their share stayed at 0% on the timestamp after the fire (19.09.2017), while the overall share of negative z-score cells grew again to 85%. The shares of overall negative z-score cells of the other indices also grew to around 88% after the fire. However, here the share of cells with a score below -1 grow to around 60%. This difference between NRI and the other indices was striking and suggested the overall lower impact of the fire on the NRI values already examined in Figure 45. Interestingly, the below -1 share jumped up to 58% for the NRI on the 17.01.2018 timestamp, reaching a slightly higher share as for the NDVI (51%) and NBR (54%). The overall share of negative z-score cells followed a similar development for all indices after the fire event. Figure 47 will give an identical analysis of the unaffected areas of this AOI.

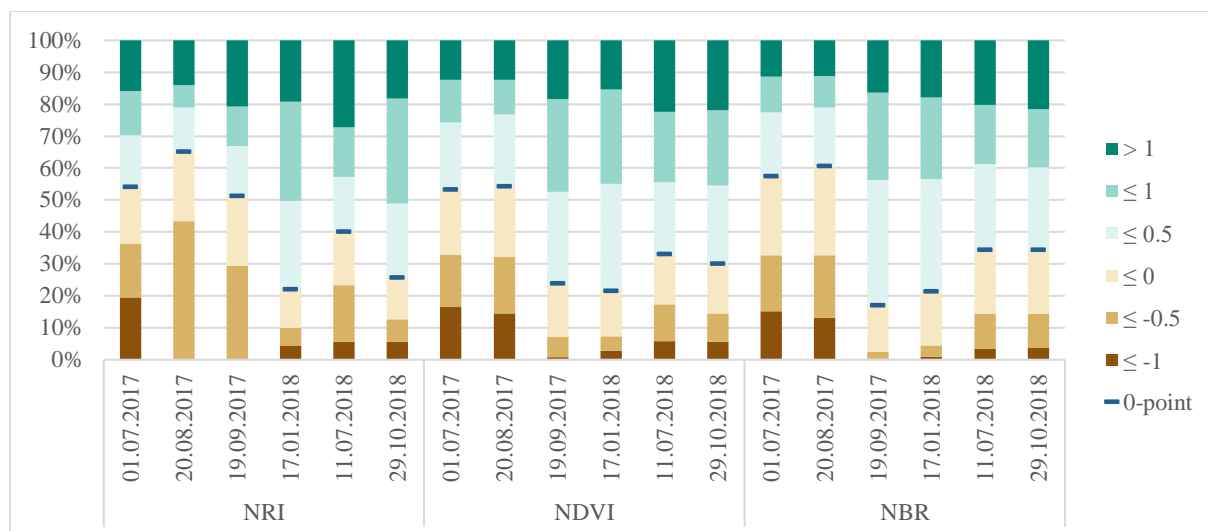


Figure 47: AOI1: Percentage of z-score class per index in unaffected areas (stacked bar chart)

For the unaffected areas, the developments of the NDVI and NBR indices were similar. After documenting more than 50% of cells with negative z-score during the summer months in the first two timestamps (NDVI: 53% and 54%, NBR: 57% and 60%), the share of cells with positive z-scores climbed to around 80% for the 19.09.2017 and 17.01.2018 timestamps, before decreasing again to around 70% for the last two timestamps. The NRI's trend was a bit more uneven: while the share of negative z-scores was also at 54% for the first timestamp, it showed the highest growth of all indices, with 11% to 65% on the second timestamp. However, on the third image, the share of positive z-scores was 49% much lower than for the other two indices. Nonetheless, it further grew to 78% in the fourth picture, before decreasing again to 60% in the fifth. The share of cells with positive z-scores then again reached 75% in the last pictures, which is analogous to the other two indices. These trends and fluctuations pointed to higher variability in the unaffected areas for NRI values, compared to NDVI and NBR values. Figure 48 and Figure 49 will now give a similar overview of the second AOI.

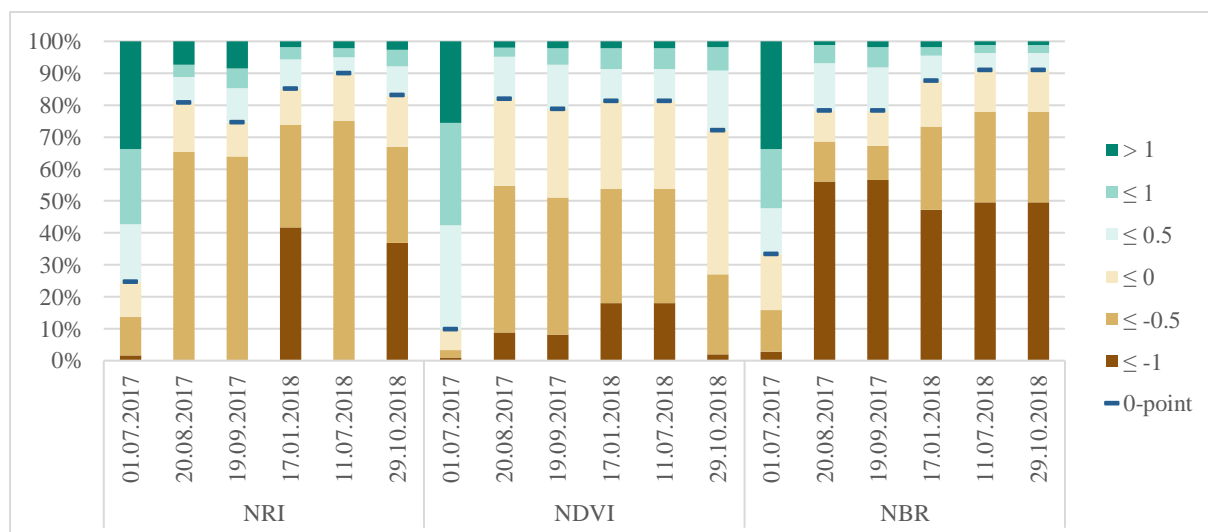


Figure 48: AOI2: Percentage of z-score class per index in affected areas (stacked bar chart)

For AOI2, the fire event took place after the first timestamp. Due to this fact, the percentage of negative z-score cells increased drastically for all indices after this date: from 24% to 80% for the NRI, from 9% to 81% for the NDVI and from 33% to 78% for the NBR. Identical to AOI1, the share of cells with z-scores below -1 again dropped to 0% for the NRI, while it grows to 8% for the NDVI and 56% for NBR. The proportion of this class and of the overall negative z-score for all indices stagnated over the next image. The fourth timestamp brought a surge of cells with z-scores below -1 for the NRI, as its percentage grew to 41%, which dropped again to 0% in the fifth timestamp, before growing again to 36% for the last image. The overall share of negative z-score cells, stayed high, reaching a maximum of 89% in picture 5. For the NDVI and NBR, the values also stayed high after the fire event: the NDVI reached its maximum at 81% in picture 4 and 5, before dropping to 72% in picture 6, while the NBR's max was 91% for the last two pictures. For this AOI, the NRI's trend showed a more inconsistent character, as it did for AOI1. Still, a striking phenomenon in the form of the absence of cells with z-scores below -1 was also observable here.

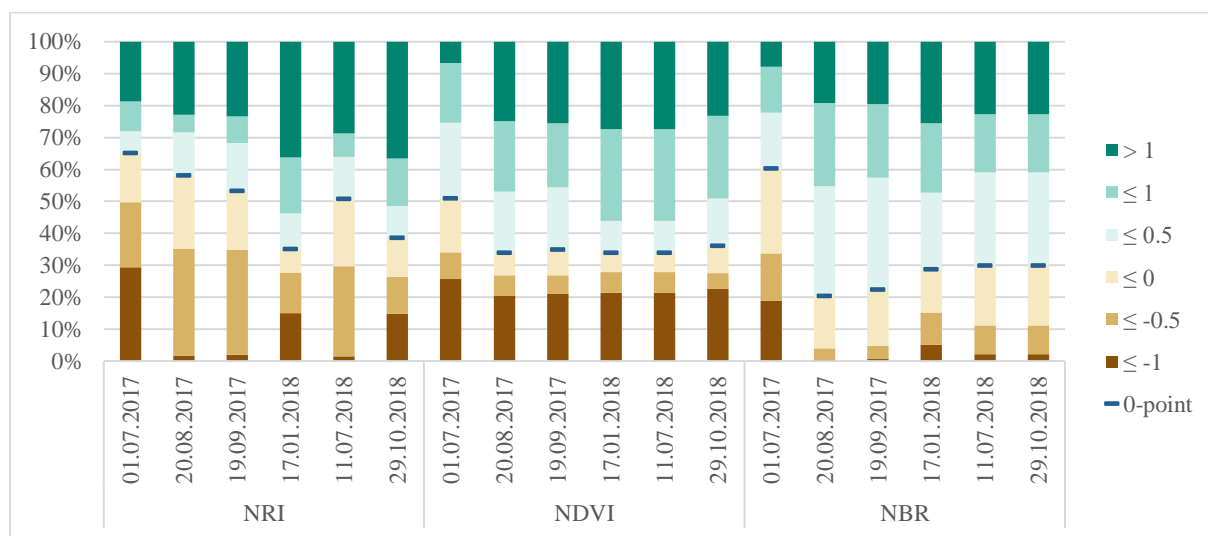


Figure 49: AOI2: Percentage of z-score class per index in unaffected areas (stacked bar chart)

For the unaffected areas of AOI2, the trends are summarized in Figure 49. All indices showed high percentages of negative z-scores at first: 64% for NRI, 50% for NDVI, and 60% for NBR. These overall values only slightly decreased to 56%, with the percentage of the z-scores below -1 dropping from 29% to 1%, for the NRI. In contrast, the overall negative values dropped more significantly to 32% for the NDVI and even harsher to 20% for NBR. Especially for the NDVI, but also the NBR, the shares stayed at a similar level for the next timesteps. The NRI shares again showed a more unsteady development: the share of negative z-score dropped to 35% in the fourth timestep, growing again to 50% on the fifth and dropping again to 38% in the last data point. This again underlined the slightly more volatile character of the NRI values in the unaffected zones and offers a similar picture to the values in AOI1. Through the intersection of the damaged areas and the AOIs, we found that, while NDVI and NBR z-score are relatively stable in the unaffected areas, the NRI ones have in comparison a more volatile

character between the analysed timepoints. Furthermore, while the share of negative z-score values increased for all indices directly after the fire in the damaged areas, the share of the lowest negative values was zero for the NRI.

4.4.1 Processes behind the differing variability distribution of the indices

An inherent factor that was cushioning the fall of the NRI values was the weighting. The class “bare soil/built-up” had, on the one hand, with 0.1 the lowest weighting of the 4 classes included in the NRI calculation. The class “High LAI vegetation” on the other hand, had the highest weighting with 0.7. In case a reporting unit consisted solely of objects belonging to the lowest class (and potentially unclassified objects, which had a weighting of 0 in our case), it reached a value of 0.1, which represented the overall bottom floor of NRI values. Likewise, if a cell consisted of only objects belonging to the “High LAI vegetation” class, its value was fixed at 0.7 and the cell could not surpass this value. This was important, as it limited the NRI scale from 0 to 1, to 0.1 to 0.7, which had implications on the variability values, especially when comparing them to the values of the other indices. Table 3 shows the example of a cell inside of the affected areas of AOI1.

CELL 173 (AOI1)	T1: 20.08.2017	T2: 19.09.2017	T2 – T1	VARIABILITY
NRI	0.404	0.101	-0.303	1.306
NDVI	0.384	0.013	-0.371	1.441
NBR	0.300	-0.280	-0.580	1.634

Table 3: Comparing the values of all three indices of cell 173 in the affected areas of AOI1

The addressed cell was situated in the north of the damaged areas of AOI1. It was chosen, as it had high differences between index values before and after the forest fire. This resulted in high variability values for all three indices. The index development of the cell shows very well, how the NRI values were cushioned at the bottom, which in turn, led to lower variability values. We have seen this before when looking at the general development of NRI and NDVI values in affected areas (see Figure 35 and Figure 36). While the trends were similar, the NRI values did not fall as much as the NDVI values directly after the fire. It must be noted, however, that this was not true in every case, as in numerous cells registered higher NRI values than for the other index values before the fire events, thus leading to higher differences between t2 and t1.

Comparing NRI, NDVI and NBR values for a single cell brings us on another significant difference between the NRI and the other two indices: while for the NDVI and NBR values were calculated per pixel through a formula using spectral bands, the NRI value of a reporting unit is based on its composition of SIAM classes. This meant in practice, that the NRI value of an object, on the inside of a reporting unit, belonging to a certain class can potentially stay the same throughout the analysis, while the NDVI and NBR values of the same pixel can differ through time. This circumstance was intensified, as in the case of the NRI, superclasses were defined, which were composed of several SIAM-classes,

thus assigning them the same weighting. If these SIAM-classes had highly different NDVI and NBR values from each other but were now grouped in the same NRI superclass, results can be deceptive. Grouping the SIAM classes in a correct way is therefore crucial and needs to be conducted with care, before continuing with the analysis.

The last paragraph described two major differences between the NRI and the other two indices: first, the NRI is grouping different landcover types into superclasses with specific weightings, while the NDVI and NBR values for these grouped landcover types can vary between each other. Second, the NDVI and NBR values for a landcover type varied over time. To show these circumstances in numbers, Table 4 was created. It shows the NRI values of the SIAM classes present in the study areas, compared to their mean NDVI and NBR values in AOI2. Three timesteps were chosen, one before the fire (01.07.2017), one directly after the fire (20.08.2017), and a later one (29.10.2018), to show the differences of the indices values between the timestamps compared to the NRI. To get the mean values of NDVI and NBR per SIAM class, pixel NDVI and NBR raster of the timestamps in AOI2 were calculated. Then, with the help of the “Zonal Statistics as Table”-tool in ArcGIS Pro, the SIAM classified raster was overlaid with the NDVI and NBR raster, to calculate the mean value of both indices per SIAM class.

CLASS #	NRI	01.07.2017		20.08.2017		29.10.2018	
		NDVI	NBR	NDVI	NBR	NDVI	NBR
1	0.7	0.585	0.594	/	/	0.716	0.642
2	0.7	/	/	/	/	0.701	0.680
3	0.7	0.489	0.495	0.527	0.498	0.620	0.533
4	0.7	0.416	0.476	0.467	0.503	0.556	0.544
5	0.7	0.133	0.459	0.171	0.420	0.278	0.447
6	0.7	-0.195	0.116	-0.020	0.207	0.324	0.393
7	0.5	0.408	0.287	0.422	0.291	0.476	0.260
8	0.5	0.358	0.272	0.398	0.322	0.446	0.277
9	0.5	0.308	0.114	0.368	0.146	0.387	0.087
10	0.5	0.270	0.207	0.281	0.225	0.288	0.175
11	0.5	0.416	0.495	0.491	0.489	0.521	0.411
13	0.1	0.150	0.079	0.059	0.068	0.053	0.103
14	0.1	0.194	0.075	0.161	0.093	0.150	0.090
15	0.1	0.143	0.018	0.115	-0.042	0.172	-0.039
16	0.1	0.176	0.129	0.162	0.142	0.162	0.091
17	0.1	-0.003	0.055	0.068	-0.091	0.178	-0.008
18	0.1	0.145	0.040	-0.052	0.064	0.109	0.015
19	0.1	0.162	0.183	0.098	0.159	0.104	0.142
21	0.2	-0.434	0.404	/	/	-0.366	0.546
22	0.2	-0.310	0.244	-0.187	0.309	-0.129	0.244
23	0.2	0.007	0.294	-0.170	0.346	0.134	0.256

Table 4: NRI and mean NDVI and NBR values for SIAM classes (01.07.2017, 20.08.2017 and 29.01.2018 (AOI2))

It immediately became apparent, when looking at the values of Table 4, that while the NRI had the same value for an individual class over all timestamps, these values changed over time for the other indices. If we take the example of class 6 (“Shadow area with vegetation”), we see how much the NDVI value fluctuated between the timestamps, and stayed the same for the NRI: SIAM class 6 was grouped with the “High LAI vegetation”-class in the NRI calculation, of which the NRI weight is 0.7. For the NDVI, however, the mean values of this class were fluctuating heavily: with an initial value of -0.195 on the first timestamp, its value dropped again to -0.020 directly after the fire and managed to increase to 0.324 on the last timestamp. For most classes, the NDVI’s mean value fluctuations were stronger than they were for the NBR. In contrast to the NRI, there was not only a difference between each of the SIAM classes but also in the values of these individual classes per timestamp for NDVI and NBR values. Looking at the range of values of some classes gave even more insights into this problem: class 17 (“Dark barren land or built-up”) had on the last timestamp a range of 0.771 for the NDVI, which placed its values between -0.368 and 0.403. Comparing this circumstance with the class having a weighting of 0.1 in every instance, for every single object and timestamp for the NRI. When after the fire event, “bare soil” pixels made up for most pixels in the affected areas, that more variability was possible for NDVI values than for NRI ones. The same goes for NBR values. Grouping these, already individually variable classes together into superclasses, as it was done in the NRI calculation, promoted the generalization even more. To further analyse the outcome of these practices on our example, the composition of the AOIs based on the superclasses used in the NRI calculation, split by affected and unaffected areas, is shown in Figure 50.

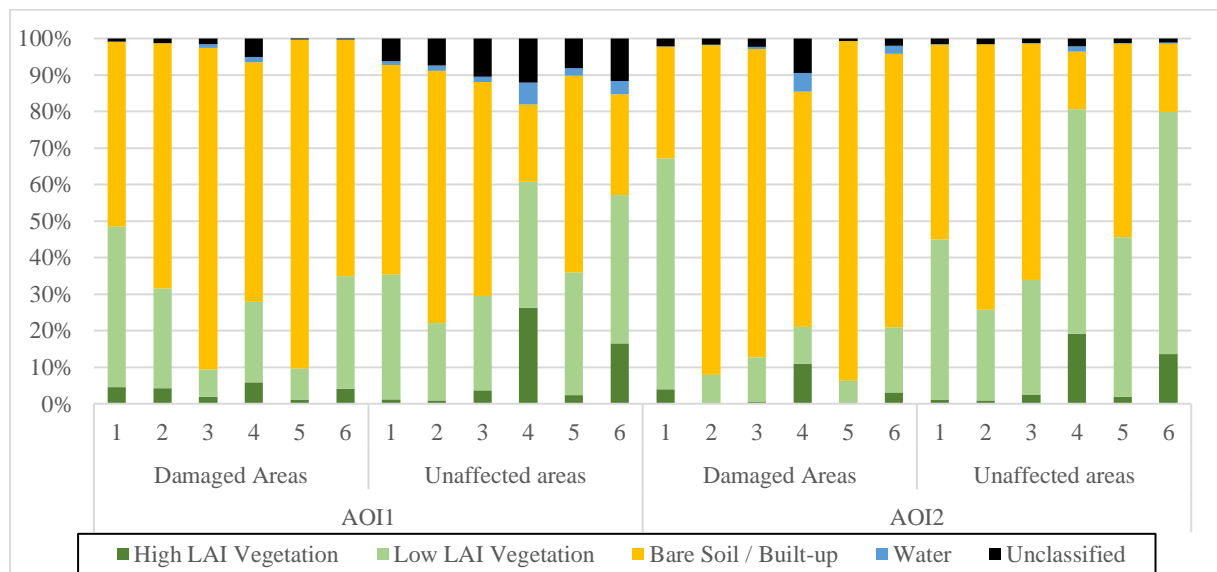


Figure 50: Composition of AOIs by SIAM superclasses (of NRI calculation), 1 to 6 on the y-axis represent the timestamps

As already suggested in the last paragraph, the share of the area belonging to the “Bare Soil / Built-up” class grew sharply immediately after the fires in the damaged areas (AOI1: 88%, AOI2: 90%). For an object classified as vegetation in the NRI calculation, this event could have had four possible outcomes

between the images: in the least likely case, it transferred from the “Low LAI Vegetation” (0.5 weighting) to the “High LAI Vegetation” class (0.7 weighting), thus increasing its “value”. It was also possible that it stayed in the same class. In most cases, the object was likely to be transferred into the “Base Soil/Built-up” superclass, losing up to 0.6 in weighting. It was, however, also possible that the object was recognized as “Unclassified” after the burn, changing its weighting to 0. Even if four possible outcomes existed in the NRI calculation's case, the value changed on a beforehand, through the classification and weighting, fixed rate. This had its effect on the variability: after the initial, one time, change event due to the fire, a share of the damaged area remained classified as “bare soil”, thus not changing back to any vegetation class. Seasonal fluctuations also turned out lower in the affected areas, which resulted in lower variability in these areas in the case of the NRI. For the unaffected areas, however, we see that seasonal fluctuations remained intact. This resulted in sharp increases in the area classified as vegetation in the timestamps four (from 28% to 50%) and six (from 35% to 56%), which corresponded with the winter and autumn months, leaving the summer months with lower vegetation shares. Objects, previously weighing 0.1, increased their weighting to 0.5 or 0.7, just to fall back to 0.1 the timestamp after. This resulted in higher variability values compared to the ones of the damaged areas.

Before moving on to the other indices, the NRI variability was once again calculated, but this time with equalized weightings of 0.5 for the two vegetation classes. The results of this calculation, with the original NRI variability raster for comparison, are seen in Figure 51.

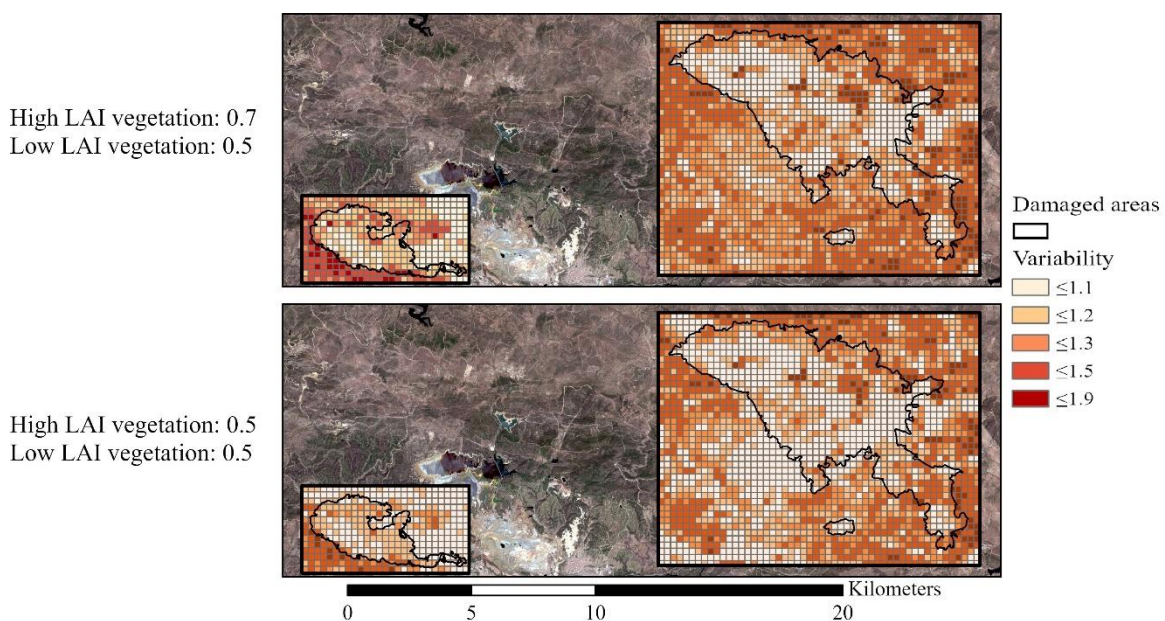


Figure 51: Comparison between NRI variability raster with a differing and equalized weighting of vegetation classes (base map: Copernicus Sentinel data 2017)

With the equalized weighting between the vegetation classes, less variability outside and inside of the damaged zones was observable. The decrease in variability through the change in weighting was

stronger in the unaffected zones than in the affected ones. Changing or equalizing the weightings of classes can have a measurable impact on the NRI variability values.

For the NDVI and the NBR, where technically no predefined classes existed, the indices were calculated per individual pixel. Yet, it can prove beneficial to examine NDVI and NBR values for the individual SIAM classes, to compare them to the NRI weightings (as seen in Table 4). When doing so, some correlations between NDVI/NBR values and SIAM classes can be found. Areas falling into classes 13 to 19 (NRI superclass “Bare Soil/Built-up”) had mean NDVI and NBR values roughly between 0 and 0.2, while some NBR values are very close to 0 and even drop below 0. SIAM classes 1 to 12 (NRI superclasses (“High” & “Low LAI Vegetation”), apart from the classes 5 and 6, showed mean values of over 0.2 for NDVI and NBR, ranging to 0.7, with values generally increasing between timestamps. The water classes, 21 to 24, generally had negative NDVI values, while their mean NBR values range between 0.2 and 0.5. Other studies also compiled general NDVI values for different landcover classes in other regions, and we see that these largely corresponded with these findings (see for example Koppad and Janagoudar, 2017, p. 211 or Aquino et al., 2018).

With these findings, it was possible to directly compare the share of the landcover classes over time, and what their conversion to another class means for the individual indicators. If the SIAM classification raster of AOI2 of the 01.07.2017 is analysed, the classes 8 (“Shrub Rangeland with Low NIR”) and 15 (“Strong barren land or built-up”) both separately accounted for 33% of the area, were not only the most important vegetation and bare-soil classes but also took up together two-thirds of the area. One timestamp later, after the fire event of AOI2, the share of class 8 shrunk to only 7%, while the share of class 15 grew to 52%. In the affected areas, these differences were even more striking: class 8 fell from 50% to only 0.5%, while class 15 increased its share from 22% to 63%. Even if class 8 managed to slowly increase its share to 10% on the last timestamp in the affected areas, these areas were still dominated by classes of the “bare soil” category with class 15 taking up 46% and class 17, namely “Dark barren land or built-up”, with 22%.

The indices reacted differently to these events. The NRI allocated fixed weights to these classes, which made its reaction easier to follow compared to the other indices. When the percentage of class 8 falls from 50% to 0.5% in the affected areas, most of these cells change their weighting from 0.5 to 0.1, as they transitioned from the “Low LAI Vegetation” to the “Bare Soil/Built-Up” superclass.

This forest fire represented a one-time change event that left a major part of former vegetation cells in the “bare soil” super-category, as already explained in the previous paragraph. This was especially observable in Figure 50 since the “Bare Soil/Built-Up” superclass captured between 64% and 90% after the fire in the damaged areas. The superclasses grouping up different classes of bare soil categories, the staleness between these superclasses after the fire, and their fixed weighting, thus lowered the variability in the damaged areas. Referring again to Figure 50, we see that in the unaffected areas of AOI2, the exchange between “bare soil” and “vegetation” cells was far more pronounced. In the summer months, the shares of the vegetation classes fell to below 30%, while they climbed to up to 79% in the winter

and autumn. These fluctuations, causing a fixed value change of 0.4 or 0.6, between the vegetation classes and the bare soil class, boosted the variability in the unaffected areas. AOI1 showed roughly the same pattern.

The picture for the other indices was far more complicated. The general trends between the superclasses of the NRI also applied to the NDVI and the NBR (effects of fire in affected areas, seasonality). However, there existed no fixed values for them. This meant for example, that a pixel falling in the SIAM class 15, can have an NDVI value of 0.26 on the 01.17.2017 picture, while it had an NDVI value of 0.05 on the 20.08.2017 picture while remaining in the same SIAM class. We have already seen this phenomenon in Table 4. Moreover, no real classes existed for these indices, which meant, that they cannot be grouped to superclasses as it was for the NRI calculation. This took away the generalization, which the NRI calculation undertook, allowing far more fluctuations between individual pixel values. A pixel categorized within a specific SIAM class can, therefore, show a certain variability in its NDVI and NBR values, even if it stayed in the same class for the NRI calculation over the whole analysis.

To explain, why the variability values were higher inside of the affected areas for NDVI and NBR, rather than in the unaffected areas, as in the case of the NRI, the sum of the absolute differences between all image pairs for these two indices was calculated. In a first step, via the “raster calculator” tool in ArcGIS Pro, the absolute differences for all cells were calculated, by taking the absolute value of the subtraction of a cell's value by its value in the former timestamp. The second step consisted then in summarizing the results of the first step by individual AOI and index. The resulting raster, showcased in Figure 52, were transformed into polygons to use the “tabulate intersection” tool to quantify the intersection between the affected and unaffected zones and the absolute differences in cell values.

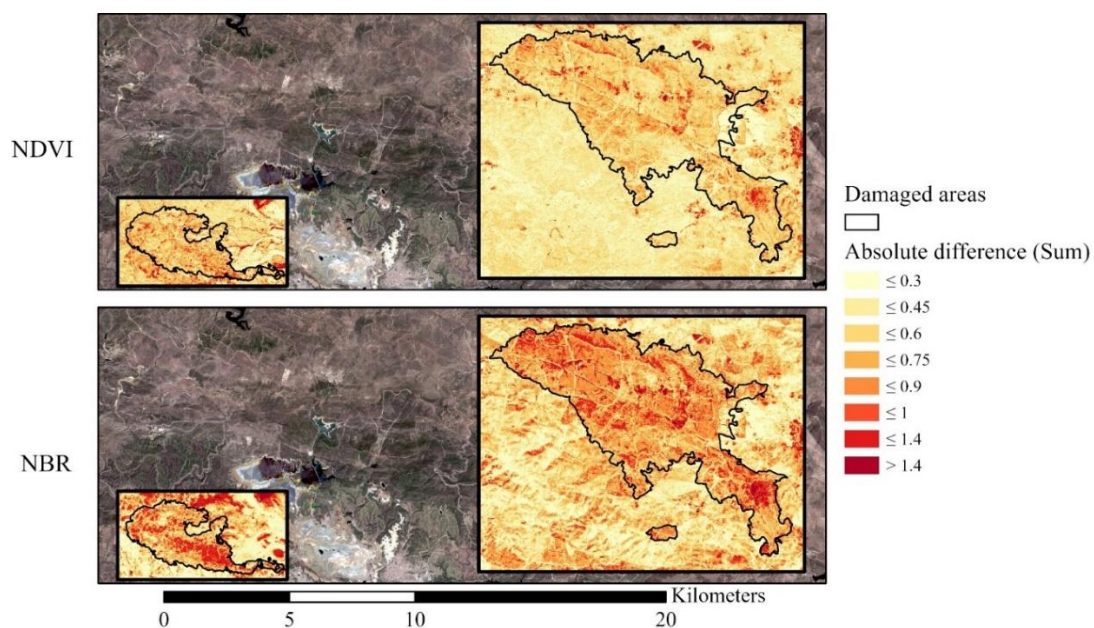


Figure 52: Sum of absolute differences between all image pairs for NDVI and NBR (both AOIs, base map: Copernicus Sentinel data 2017, contains modified Copernicus Sentinel data 2017, 2018)

The results of the intersections are shown in Figure 53 in the form of bar charts. The raster in Figure 52 shows a higher concentration of cells with high values within the damaged areas of both AOIs. The values were also overall higher for the NBR than for the NDVI. For both indices, we saw patches of areas with high absolute difference values outside of the damaged regions. It was, therefore, necessary, to round off the visual interpretation with a quantitative analysis of the shares of cells in the different absolute classes and to compare affected and unaffected areas in this regard. This practice was already applied numerous times throughout the thesis. Figure 53 finally shows the distribution in the form of a bar chart.

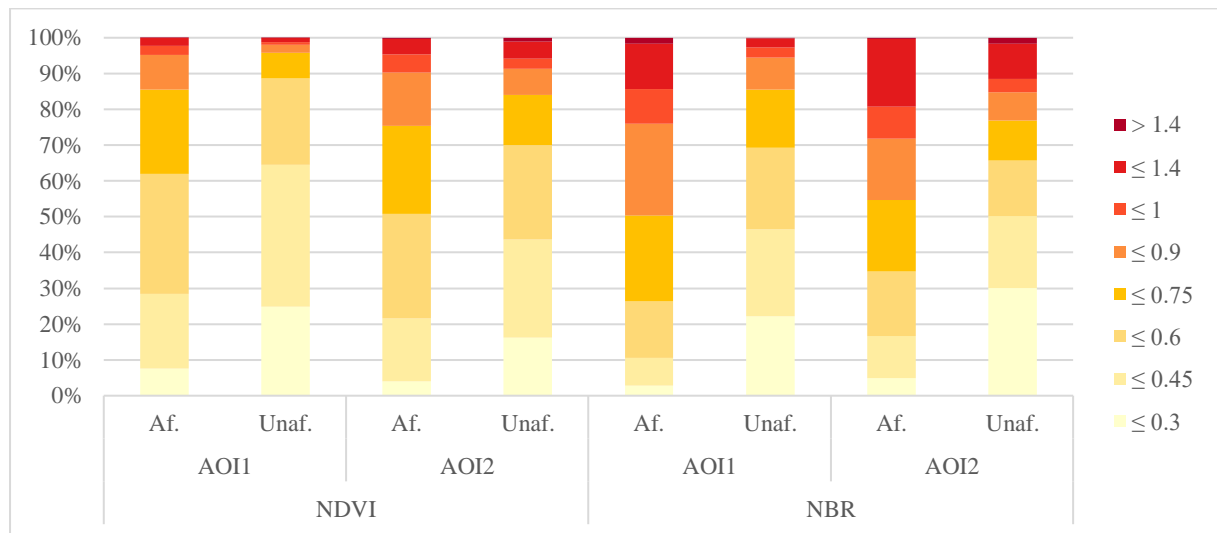


Figure 53: Distribution of cells regarding the sum of the absolute differences between image pairs

For the NDVI, we see how the share of cells with higher absolute differences is higher in the affected areas than in the unaffected ones for both AOIs. While the share of cells for which the sum of absolute NDVI differences was over 0.6 is at 12% for the unaffected areas of AOI1, it was 38% for the affected areas. For AOI2 the picture was similar: with 30% in the unaffected areas and 50% in the affected ones. This showed that for the NDVI more change can be observed in the affected areas, thus causing higher variability values. The NBR index showed an even more pronounced picture: here the share of cells with a value of over 0.6 was at 73% in the affected and only 30% for the unaffected areas for AOI1. For AOI2, the share was at 65% in the affected, and at 34% in the unaffected areas. Same as for the NDVI, more change can be reported in the affected areas for the NBR, which explains the higher variability values.

5 Discussion

Having explained the methodological and technical properties behind a time-series variability approach, namely LIVID, and its application on a specific scenario, a discussion of the results follows in this chapter, ahead of concluding the thesis in the last chapter. Before going over the results of the test run, the technical improvements of the LIVID application in eCognition are discussed in the first subchapter. To see how the NRI indicator performs in comparison to the NDVI and NBR indicators, the three are evaluated together in the second subchapter. As already mentioned, the AOIs were split up into affected and unaffected areas, which will also be differentiated in this evaluation. The goal is an overview of the results of all indicators. With this overview, potential differences between the results can be identified and analysed.

5.1 Implemented features

The following part revolves around the functions which were implemented during this work. As their technical background was already discussed earlier, this part will focus on their contribution to the work. Adding the calculation of two other indicators to the LIVID application offered not only a possibility to compare the NRI output to that of the NDVI and NBR, but also to enhance the application's results and its versatility. A case study can now not only be analysed based on its NRI, but also from the viewpoint of the NDVI and NBR. The user can now calculate all these indicators within one application. These measures were primarily taken to investigate a forest fire. As mentioned above, other case studies might demand other indicators, which could be implemented similarly as the NDVI and NBR.

The reason for choosing NDVI and NBR have already been discussed in chapter 3: the NDVI, on the one hand, is an indicator for photosynthetic pigments in leaves and therefore gave a good picture of green vegetation in an area. The NBR, on the other hand, visualized the difference between burned and unburned areas. Whilst compiling this master's thesis, the results of the indicators first provided a means of comparing the NRI results to them, where they were later used as part of the case study evaluation. Thereby their implementation into the application did not only help with the case study in one but in several ways: it opened the way for more indicators, it provided comparison and it enhanced the results. The other new features did not have such an impact on the analysis itself but still made the work with the application easier. This is even more important, as some tests had to be repeated several times.

On this occasion, some features must be mentioned which could have been implemented to improve the application even more. Besides other spectral indicators, the most obvious is an automated layer name extraction for pre-calculated NDVI and NBR layers, in the same fashion as it was implemented throughout this work for NRI layers. A limitation of the current LIVID application is that the user must re-initialize the process again if she or he wanted to calculate a different index. It would prove beneficial, if the user could load all the necessary data for the desired index calculations and then

process all of this in one go, providing results for multiple indices, without having to fix the same settings multiple times. Another improvement would be assigning classes and weights on NDVI/NBR values when calculating these indexes per reporting unit. The pixel values would be classified, and the calculations would follow a similar way as for the NRI. A more practical development would have been an overhaul of the export function, to make it possible to export a single shapefile per indicator, summarizing all values for the different timestamps and the variability values of the cells. This would make further processing of the data much easier. A custom algorithm might have been the right way to implement such a function.

5.2 Test-run of the LIVID application

After calculating the index values for all reporting units and converting them into z-scores, the resulting maps showed that the indices had the same developments over time, but also the large difference in all index values between the areas affected by the fires, and the unaffected ones. The author, therefore, decided to split the index shapefiles by affected and unaffected areas, doubling the number of shapefiles from 18 (6 per index) to 36. The percentage change from the first to the following five timestamps, showed the impact of the fire in the affected areas in the form of drops directly after the fire, in the respective AOI. The trends in the unaffected areas gave an appropriate indication of seasonal trends in the area under investigation. A direct comparison of trends in and outside of the damaged areas showed that seasonal trends still affected all indices inside of the burned areas after the fires. It also portrayed rather similar courses of the NRI and NDVI indices. An overview of the mean z-score differences for all indices for both AOIs showed the similarity of the development of the three indices throughout the analysis.

Finally, the variability results of the indices are compared. The distribution of variability values differed from the NRI to the NDVI and NBR: while the NDVI and NBR showed a strong concentration of high variability values inside of the damaged areas, the distribution of these values was not as clear-cut for the NRI. A direct comparison of variability raster and mean z-score difference raster, showed more clearly, how for the NDVI and NBR, high variability cells tended to overlap with negative mean z-score differences, while for the NRI they overlapped more with positive mean z-score differences. Two assumptions arose from these findings: the first one being that the fires did have a lesser impact on the NRI values, compared to the other two indices. The second one is that the forest fire itself created less variability, compared to the seasonal changes of the vegetation outside of the damaged areas, for the NRI. To verify the first assumption, the z-score difference between the images directly before and after the fires for both AOIs and all indices were calculated. For the NDVI and NBR, the damaged areas showed a higher share of strongly negative z-score differences than for the NRI, which was in turn interpreted as a stronger impact of fires on the NDVI and NBR values, compared to the NRI ones. For the second assumption, the previously generated z-scores per reporting unit and timestamp for all indices were used, and its intersection with affected and unaffected areas was calculated. This procedure

generated new insights: as opposed to the other indices, the share of NRI reporting units with negative z-scores increased in AOI1 even before the fire in the damaged areas. For the undamaged areas, more fluctuations exist between the shares of negative and positive z-scores over the different timestamps for the NRI, as for the other indices.

The inherent differences in the calculations of the indices were addressed, to further explain the differing variability distributions. Whereas the NRI calculation grouped several landcover classes to specific superclasses and assigned them a fixed weight, the NDVI, and NBR values were calculated per individual pixel. These pixel values can change over time, even if they are describing the same type of landcover at every timestep. This circumstance alone led to differing values per specific landcover type, creating variability without a change in landcover. Furthermore, while a change in landcover always results in a fixed value change for the NRI, a change for NDVI and NBR was far less predictable value-wise.

The changes in SIAM class shares over both AOIs showed how, after the fire events, the shares of the “bare soil” superclass stayed relatively high, while both vegetation superclasses had low shares in the damaged areas. With the stale character of the NRI calculation in this thesis, low variability values resulted. The undamaged areas have shown fluctuations between vegetation classes and the bare soil class, through seasonality, which in turn meant higher variability values, as objects increased and decreased their values by fixed rates of 0.4 and 0.6. For the other two indices, the sum of absolute differences between the image pairs was calculated per pixel. The goal was to discover, where the most change happened over the time of the analysis. It turned out that, for both the NDVI and the NBR, the damaged areas had a greater share of pixels with elevated sums of absolute differences. Thus meaning, that the fires increased the fluctuations in the affected areas over the seasonal effects of the unaffected areas, explaining the higher variability values.

The NDVI can be used to detect green vegetation in an area and the NBR serves as a means to spot if the vegetation in an area sustained damaged by fire. The settings of the LIVID application put a strong focus on the vegetation classes when calculating the NRI values. As we have seen, this meant for the results, that seasonal variations in vegetation, in the form of dehydration in the summer and more growth in autumn and winter, had more influence on the NRI variability results, than the one-time, abrupt change event of vegetation reduction, in form of the fire. The NRI can consequently not be seen as a replacement for the other indices but serve as a supplement while conducting research on natural resources.

In our case, the NRI values and their variability gave a comprehensive overview of the seasonal variations in the area and the effect the fires had on them. The NRI variability values hence showed how the seasonal variations in the affected areas turned out lower than in the unaffected ones.

NRI variability values were higher in unaffected areas than they were in the affected ones. These results complement the results of the NDVI and NBR values, which variability results focused on the effects of the fire in the areas. For these two indices, high variability values overlapped with areas that sustained

damage by the fire. The one-time abrupt change event caused more variability for them than the seasonal variation in the area. With more expert knowledge, the results could be refined further, with more superclasses, regrouping classes in a more specific way, and appropriate weightings per class. The LIVID approach and its eCognition application further have the advantage, that they can be easily applied to other test cases.

The approach, however, had its limitations. One that can be observed right from the start, was the needed database. To run the LIVID application and to calculate the NRI values, the user needed pre-classified images of their area of interest. In some cases, this step can be interconnected with far more time and effort, than simply using satellite bands to calculate spectral indices like the NDVI or NBR. A second limitation was already addressed when investigating the causes behind the differing variability values between the NRI and the other two indices. When forming superclasses for the NRI calculation, some sort of generalization was exerted, in the form of weighting. It is therefore important, to gather sufficient knowledge on the area of interest and the different landcover classes so that the grouping and weighting are done adequately. This grouping, however, also meant that whatever the season if classified in the same superclass, a certain landcover class had the same weighting. As we have learned in our test run, other indices have differing values, depending on the time of the year through seasonality. This circumstance was so far not reflected in the NRI calculation, which resulted in a certain staleness for the NRI values and the changes between them. In the cases of NDVI and NBR, the values were calculated per individual pixel, which led to more variability within the landcover classes.

Additional research could focus on how the variability values change if different superclasses and weights are defined. In this work, this topic was touched upon only briefly when equalizing the vegetation superclasses weights in the variability subchapter. The focus would lie here more on testing different settings for the NRI calculation and on then comparing the variability results between several test runs of the same area of interest. These settings would hence require more background knowledge as already mentioned throughout the later chapters of this thesis. Further steps in the development of the LIVID approach and its application could tackle the issue of the staleness of weights in the case of seasonal fluctuations. Seasonal weights could be applied to certain classes, in which dry seasons have their impact. This would then better reflect variability in areas, in which no direct class changes occur. Working with different land cover classification systems and comparing their results would be another task that could generate new insights into future research projects. Finally, we see that both the execution and the development of the LIVID approach and its technical application, offer prospects for improvement.

6 Conclusion

The first part of the thesis discussed the technical implementation of the LIVID approach in the form of an application in eCognition, while the second part was a test run of the said application on a specific test case, namely a forest fire in Spain. The reasoning behind this division was to fulfil two separate, but still interconnected research purposes: Firstly, additions to the existing LIVID application were sought after and implemented. Secondly, the enhanced application was tested on an abrupt change event to see its results and then, to compare them to the results of established indices, namely NDVI and NBR. The implemented features are on the focus of the first research question. Besides the quality of life additions, in the form of an automated filename extraction for specific formats, and the configuration of the “NoData” slider for the variability calculation, the functions added got selected by their usefulness for the upcoming case study. Adding an export function to the application made it easier to process its results in ArcGIS Pro and other software. The most important part was, however, the implementation of the capability of calculating the spectral indices NDVI and NBR inside of the LIVID application. This step made it possible to easily generate NDVI and NBR values of the same reporting units and then compare them to the NRI results. The NDVI and NBR indices were useful in this project, as they indicated the vegetation and the burning activity in the area. Furthermore, they gave a base for comparison for NRI values, which was important for the second research question. As already mentioned throughout the study, many more functions could have been added.

The second research question was directed at testing the LIVID approach on a specific case study. A forest fire, as an abrupt, one-time change event, presented an interesting subject for the test run of the LIVID approach and its application. After having calculated the NRI values, the NDVI and NBR ones followed. At first glance, all index values pointed in the same direction. When, after all, the variability values for the indices were compared, the NRI values differed greatly from the other two indices. While for the NDVI and NBR high variability values were concentrated inside of the damaged areas, the values were higher in the unaffected areas for the NRI. Furthermore, high variability values overlapped with positive mean change for the NRI values when they overlapped with negative mean change for the other indices. On the one hand, the fire had less impact on the NRI values, than it had on the other index values. Seasonal vegetation growth and decline, on the other hand, influenced the NRI values more than the other values.

The next step was to concentrate on the causes of these differences. Possible explanations were found in the staleness of NRI values, as multiple landcover classes are generalized within superclasses with fixed weight values. The NDVI and the NBR values do not underlie strict classification, as they are calculated per pixel and therefore show more fluctuating values. When focusing on the indices themselves, it was observable that for the NRI, the fires reduced the seasonal activity in the affected zones, when in the unaffected zones an exchange in shares between vegetation and bare soil classes occurred which made for greater variability. For the NDVI and NBR indices, the overall absolute

change was calculated, which indicated, that the index values in the affected areas undergo the greatest changes, resulting in the highest variability values.

Concluding, it can be said that the NRI variability results focused on seasonality and its disruption in the affected areas, while the NDVI and NBR results focused on the abrupt change caused by the fire, inside of the damaged areas. The deviation of the NRI outcomes from the results of the other indices should not be treated as errors, but rather as an alternate description of the same event. The NRI results, and their focus on seasonality and its disruption, can thus support the results of the well-established indicators and show the incident from another point of view. The LIVID approach is thereby no substitute for the other indices, but rather a further highly customizable instrument in the tool kit of remote sensing.

7 Sources

- AEMET, 2015. Valores climatológicos normales. Huelva, Ronda Este [WWW Document]. Valores Clim. Norm. Huelva Ronda Este. URL <http://www.aemet.es/es/serviciosclimaticos/datosclimatologicos/valoresclimatologicos?l=4642E&k=undefined> (accessed 4.18.20).
- Anyamba, A., Tucker, C.J., 2005. Analysis of Sahelian vegetation dynamics using NOAA-AVHRR NDVI data from 1981–2003. *J. Arid Environ.* 63, 596–614. <https://doi.org/10.1016/j.jaridenv.2005.03.007>
- Aquino, D. do N., Rocha Neto, O.C. da, Moreira, M.A., Teixeira, A. dos S., Andrade, E.M. de, 2018. Use of remote sensing to identify areas at risk of degradation in the semi-arid region. *Rev. Ciênc. AGRONÔMICA* 49. <https://doi.org/10.5935/1806-6690.20180047>
- Baraldi, A., 2019. SIAM™ (Satellite Image Automatic Mapper™). Interdisciplinary Centre of Competence for Geoinformatics, Z-GIS, University of Salzburg.
- Baraldi, A., Humber, M.L., Tiede, D., Lang, S., 2018a. GEO-CEOS stage 4 validation of the Satellite Image Automatic Mapper lightweight computer program for ESA Earth observation level 2 product generation - Part 1: Theory. *Cogent Geosci.* 4. <https://doi.org/10.1080/23312041.2018.1467357>
- Baraldi, A., Humber, M.L., Tiede, D., Lang, S., 2018b. GEO-CEOS stage 4 validation of the Satellite Image Automatic Mapper lightweight computer program for ESA Earth observation level 2 product generation – Part 2: Validation. *Cogent Geosci.* 4. <https://doi.org/10.1080/23312041.2018.1467254>
- Blaschke, T., 2010. Object based image analysis for remote sensing. *ISPRS J. Photogramm. Remote Sens.* 65, 2–16. <https://doi.org/10.1016/j.isprsjprs.2009.06.004>
- Braun, A., Hochschild, V., 2017. A SAR-Based Index for Landscape Changes in African Savannas. *Remote Sens.* 9, 359. <https://doi.org/10.3390/rs9040359>
- Drusch, M., Del Bello, U., Carlier, S., Colin, O., Fernandez, V., Gascon, F., Hoersch, B., Isola, C., Laberinti, P., Martimort, P., Meygret, A., Spoto, F., Sy, O., Marchese, F., Bargellini, P., 2012. Sentinel-2: ESA's Optical High-Resolution Mission for GMES Operational Services. *Remote Sens. Environ.* 120, 25–36. <https://doi.org/10.1016/j.rse.2011.11.026>
- ESA, 2015. Sentinel-2 User Handbook, 1st ed, ESA Standard Document. European Space Agency, Paris.
- EuroGeographics, 2016. Nomenclature of Territorial Units for Statistics (nuts).
- Hagenlocher, M., Lang, S., Tiede, D., 2012. Integrated assessment of the environmental impact of an IDP camp in Sudan based on very high resolution multi-temporal satellite imagery. *Remote Sens. Environ.* 126, 27–38. <https://doi.org/10.1016/j.rse.2012.08.010>
- Hervé, A., 2007. Z-scores, in: Salkind, N.J., Rasmussen, K. (Eds.), *Encyclopedia of Measurement and Statistics*. SAGE Publications, Thousand Oaks, Calif, pp. 1057–1058.
- Hussain, M., Chen, D., Cheng, A., Wei, H., Stanley, D., 2013. Change detection from remotely sensed images: From pixel-based to object-based approaches. *ISPRS J. Photogramm. Remote Sens.* 80, 91–106. <https://doi.org/10.1016/j.isprsjprs.2013.03.006>
- Key, C.H., Benson, N.C., 2006. Landscape Assessment, in: FIREMON: Fire Effects Monitoring and Inventory System, General Technical Report. United States Department of Agriculture, Fort Collins, pp. LA1–LA51.
- Koppad, A.G., Janagoudar, B.S., 2017. VEGETATION ANALYSIS AND LAND USE LAND COVER CLASSIFICATION OF FOREST IN UTTARA KANNADA DISTRICT INDIA THROUGH GEO-INFORMATICS APPROACH. *ISPRS - Int. Arch. Photogramm. Remote Sens. Spat. Inf. Sci.* XLII-1/W1, 219–223. <https://doi.org/10.5194/isprs-archives-XLII-1-W1-219-2017>
- MAPA, 2018. Los Incendios Forestales en España. Ministerio de Agricultura y Pesca, Alimentación y Medio Ambiente, Madrid.
- Peel, M.C., Finlayson, B.L., McMahon, T.A., 2007. Updated world map of the Köppen-Geiger climate classification. *Hydrol. Earth Syst. Sci.* 11, 1633–1644. <https://doi.org/10.5194/hess-11-1633-2007>

- Robinson, N., Allred, B., Jones, M., Moreno, A., Kimball, J., Naugle, D., Erickson, T., Richardson, A., 2017. A Dynamic Landsat Derived Normalized Difference Vegetation Index (NDVI) Product for the Conterminous United States. *Remote Sens.* 9, 863. <https://doi.org/10.3390/rs9080863>
- Rouse, J.W., Jr., Haas, R.H., Schell, J.A., Deering, D.W., 1973. Monitoring vegetation systems in the Great Plains with ERTS. *Proc. Third Earth Resour. Technol. Satell.-1 Symp.* 1, 309–317.
- Salas Trujillo, F., Estesó Victorio, E., Andalucía, Consejería de Medio Ambiente, 2003. Plan Infoca: un plan de acción al servicio del monte mediterráneo andaluz. Junta de Andalucía, Consejería de Medio Ambiente, Sevilla.
- Singh, A., 1989. Review Article Digital change detection techniques using remotely-sensed data. *Int. J. Remote Sens.* 10, 989–1003. <https://doi.org/10.1080/01431168908903939>
- Sudmanns, M., Augustin, H., Tiede, D., Baraldi, A., 2019. An object-based indicator to describe variability in time series of remote sensing images: the LIVID approach.
- Trimble, 2017. eCognition Developer User Guide. Trimble Germany GmbH, Munich.
- Utanda, A., 2019. EMSN-060: Monitoring areas damaged by forest fires in Andalusia, Spain, EMERGENCY MANAGEMENT SERVICE - RISK AND RECOVERY MAPPING. General Directorate of Civil Protection in Spain (CENEM), Spain.
- Vallejo-Villalta, I., Rodríguez-Navas, E., Márquez-Pérez, J., 2019. Mapping Forest Fire Risk at a Local Scale—A Case Study in Andalusia (Spain). *Environments* 6, 30. <https://doi.org/10.3390/environments6030030>

8 Table of figures

Figure 1: Segmentation of agricultural land in Andalusia, Spain (eCognition, contains Copernicus Sentinel data 2017)	9
Figure 2: Example of a basic ruleset in eCognition	10
Figure 3: The communication between action and ruleset is organized by algorithms (Source: Trimble, 2017, p. 239)	11
Figure 4: Example of action definition	11
Figure 5: Parameter set example	12
Figure 6: Ruleset example	12
Figure 7: Natural Resource Index (NRI) calculation for one grid cell (based on Braun and Hochschild, 2017, p. 9)	13
Figure 8: Calculation of the variability of a reporting unit (own depiction, based on Braun and Hochschild, 2017, p. 11)	14
Figure 9: Variability calculation by reporting unit (based on Hagenlocher et al., 2012, p. 32)	15
Figure 10: LIVID application GUI	15
Figure 11: “Create Time-Series Project” group in the LIVID application	16
Figure 12: Reporting units (blue lines) overlaid on an image (left: squares, right: hexagons, scale 25)	16
Figure 13: “Define class aggregations” group in the LIVID application	17
Figure 14: Classified hexagon units (scale: 25)	18
Figure 15: classified reporting units (hexagons), based on NRI values (red: NIR < 0.3, yellow: NIR < 0.7) (Andalusia 01.07.2017)	18
Figure 16: Simplified workflow of LIVID application	19
Figure 17: Updated GUI with file name format tick box	20
Figure 18: Updated process tree with file name extraction	20
Figure 19: Implemented export GUI in LIVID application	21
Figure 20: Altered variability calculation process with implemented "No Data"-threshold	22
Figure 21: Variability values at differing NoData-treshold (scale: 1:150000)	22
Figure 22: Updated "Add images" group for NDVI and NBR calculation in LIVID application	24
Figure 23: Updated LIVID workflow, where A is the process for NRI, and B for NDVI and NBR	25
Figure 24: Climograph of Huelva (1984-2010) (source: AEMET, 2015, own depiction)	27
Figure 25: Study area with damaged areas (scale: 1: 200,000, sources: damaged areas: EMSN-060 report (Utanda, 2019), base map: Copernicus Sentinel data from 01.07.2017), administrative boundaries: (EuroGeographics, 2016))	28
Figure 26: Assessment of vegetation recovery (Source: Utanda 2019) (base map: Copernicus Sentinel data 2017, scale: 1:100,000)	30

Figure 27: Comparison of Sentinel-2 and SIAM-classified image of the study area, with damaged areas in red (Copernicus Sentinel data: 01.07.2017 and 19.09.2017, scale: 1:250,000, source of damaged areas: Utanda, 2019, source of SIAM legend: Baraldi 2019)	32
Figure 28: NRI, NDVI and NBR z-scores for AOI1 (contains modified Copernicus Sentinel data 2017, 2018, scale: 1:300,000)	35
Figure 29: NRI, NDVI and NBR z-scores for AOI2 (contains modified Copernicus Sentinel data 2017, 2018, scale: 1:150,000)	36
Figure 30: Affected and unaffected areas (scale 1:150,000)	37
Figure 31: AOI1 - affected areas: percental change of mean indices (base: 01.07.2017)	38
Figure 32: AOI1 - unaffected areas: percental change of mean indices (base: 01.07.2017)	39
Figure 33: AOI2 - affected areas: percental change mean indices (base: 01.07.2017)	39
Figure 34: AOI2 - unaffected areas: percental change mean indices (base: 01.07.2017)	40
Figure 35: AOI1 - percentage change of all indices in affected and unaffected (base date: 01.07.2017)	41
Figure 36: AOI2 - percentage change of all indices in affected and unaffected (base date: 01.07.2017)	41
Figure 37: Mean difference in z-score values for all indices (base map: Copernicus Sentinel data 2017, contains modified Copernicus Sentinel data 2017, 2018, scale: 1:200,000)	42
Figure 38: NRI variability raster with damaged areas overlaid (base map: Copernicus Sentinel data 2017, scale: 1:200,000)	43
Figure 39: Variability rasters for NRI, NDVI, and NBR (base map: Copernicus Sentinel data 2017, contains modified Copernicus Sentinel 2 data 2017, 2018, scale: 1:200,000)	44
Figure 40: Stacked column chart of the relative spread of variability classes over AOIs and areas, with data labels	45
Figure 41: Comparison of mean z-score difference and index variability (base map: Copernicus Sentinel data 2017, contains modified Copernicus Sentinel data 2017, 2018, scale: 1:250,000)	46
Figure 42: AOI1 - Stacked bar chart of distribution of mean z-score difference per variability class	47
Figure 43: AOI2 - Stacked bar chart of distribution of mean z-score difference per variability class	48
Figure 44: Z-score differences (t1 - t0) of all indices for both AOIs (base map: Copernicus Sentinel data 2017, contains modified Copernicus Sentinel data 2017)	49
Figure 45: Intersection of z-score differences of the fire events and damaged areas for both AOIs	50
Figure 46: AOI1: Percentage of z-score class per index in affected areas (stacked bar chart)	51
Figure 47: AOI1: Percentage of z-score class per index in unaffected areas (stacked bar chart)	52
Figure 48: AOI2: Percentage of z-score class per index in affected areas (stacked bar chart)	52
Figure 49: AOI2: Percentage of z-score class per index in unaffected areas (stacked bar chart)	53
Figure 50: Composition of AOIs by SIAM superclasses (of NRI calculation), 1 to 6 on the y-axis represent the timestamps	56

Figure 51: Comparison between NRI variability raster with a differing and equalized weighting of vegetation classes (base map: Copernicus Sentinel data 2017)	57
Figure 52: Sum of absolute differences between all image pairs for NDVI and NBR (both AOIs, base map: Copernicus Sentinel data 2017, contains modified Copernicus Sentinel data 2017, 2018)	59
Figure 53: Distribution of cells regarding the sum of the absolute differences between image pairs	60
Table 1: Sentinel-2 imagery with number of days since the beginning of the analysis	31
Table 2: Classes for experiment together with weightings	33
Table 3: Comparing the values of all three indices of cell 173 in the affected areas of AOI1	54
Table 4: NRI and mean NDVI and NBR values for SIAM classes (01.07.2017, 20.08.2017 and 29.01.2018 (AOI2))	55
Table 5: SIAM classes (Baraldi, 2019)	72
Table 6: Statistical evaluation of indicators for AOI1 (based on modified Copernicus Sentinel data 2017, 2018)	73
Table 7: Statistical evaluation of indicators for AOI2 (based on modified Copernicus Sentinel data 2017, 2018)	74

Appendix I – SIAM Classes

CLASS NR	NAME	CLASS NR	NAME
1	Strong vegetation with high NIR	18	Weak barren land or Shadow area with Barren Land
2	Strong vegetation with low NIR	19	Near InfraRed-Peaked Barren land or Built-up
3	Average vegetation with high NIR	20	Burned area
4	Average vegetation with low NIR	21	Deep water or shadow
5	Weak vegetation	22	Shallow water or shadow
6	Shadow area with vegetation	23	Turbid water or shadow
7	Shrub Rangeland with High NIR	24	Salty Shallow Water
8	Shrub Rangeland with Low NIR	25	Cloud
9	Herbaceous Rangeland	26	Smoke Plume
10	Weak Rangeland	27	Thin clouds over vegetation
11	Pit bog Leaf SC	28	Thin clouds over water area or Barren land or Built-up areas
12	Greenhouse Leaf SC	29	Snow or water ice
13	Very bright barren land or built-up	30	Shadow Snow
14	Bright barren land or built-up	31	Shadow areas
15	Strong barren land or built-up	32	Flame
16	Average barren land or built-up	33	Unknown
17	Dark barren land or built-up	255	No Data

Table 5: SIAM classes (Baraldi, 2019)

Appendix II – Statistical Evaluation of NRI, NDVI and NBR

AOII		01.07.2017	20.08.2017	19.09.2017	17.01.2018	11.07.2018	29.10.2018
NRI (AFFECTED)	Mean	0.294	0.233	0.163	0.263	0.163	0.276
	Median	0.270	0.167	0.111	0.221	0.120	0.242
	Max	0.692	0.693	0.660	0.698	0.666	0.691
	Min	0.100	0.100	0.100	0.100	0.100	0.100
	Sum	241.357	190.852	133.834	215.935	133.975	226.425
	5% Percentile	0.112	0.100	0.100	0.100	0.100	0.108
	95% Percentile	0.544	0.545	0.447	0.542	0.413	0.556
NRI (UNAFFECTED)	Mean	0.283	0.209	0.245	0.465	0.296	0.451
	Median	0.278	0.171	0.216	0.473	0.291	0.466
	Max	0.634	0.643	0.678	0.700	0.665	0.698
	Min	0.093	0.098	0.100	0.100	0.098	0.101
	Sum	371.110	273.981	321.179	609.463	387.813	592.210
	5% Percentile	0.114	0.101	0.105	0.255	0.116	0.247
	95% Percentile	0.474	0.449	0.493	0.642	0.495	0.621
NDVI (AFFECTED)	Mean	0.346	0.289	0.162	0.293	0.247	0.345
	Median	0.338	0.277	0.141	0.284	0.231	0.330
	Max	0.569	0.530	0.500	0.609	0.538	0.621
	Min	0.151	0.052	-0.008	0.036	0.110	0.156
	Sum	283.810	236.620	132.945	240.608	202.157	282.979
	5% Percentile	0.219	0.176	0.036	0.114	0.172	0.243
	95% Percentile	0.498	0.448	0.367	0.501	0.387	0.504
NDVI (UNAFFECTED)	Mean	0.333	0.279	0.299	0.428	0.335	0.439
	Median	0.334	0.278	0.298	0.427	0.336	0.442
	Max	0.558	0.518	0.551	0.654	0.561	0.642
	Min	0.095	0.092	0.100	0.118	0.085	0.122
	Sum	437.121	365.488	391.707	561.459	439.417	576.080
	5% Percentile	0.219	0.179	0.189	0.312	0.218	0.320
	95% Percentile	0.452	0.394	0.424	0.560	0.460	0.558
NBR (AFFECTED)	Mean	0.170	0.173	-0.089	0.045	0.031	0.085
	Median	0.146	0.151	-0.129	0.025	0.015	0.047
	Max	0.540	0.579	0.531	0.698	0.478	0.644
	Min	-0.025	-0.255	-0.365	-0.354	-0.169	-0.126
	Sum	139.546	141.754	-73.385	37.224	25.415	69.350
	5% Percentile	0.033	0.040	-0.302	-0.262	-0.091	-0.061
	95% Percentile	0.384	0.396	0.267	0.396	0.224	0.367
NBR (UNAFFECTED)	Mean	0.152	0.153	0.156	0.309	0.143	0.244
	Median	0.147	0.142	0.144	0.292	0.136	0.231
	Max	0.478	0.510	0.569	0.745	0.501	0.677
	Min	-0.126	-0.088	-0.098	-0.058	-0.079	-0.068
	Sum	199.133	201.121	205.277	405.011	187.967	320.503
	5% Percentile	0.032	0.040	0.022	0.133	0.008	0.064
	95% Percentile	0.298	0.307	0.339	0.531	0.309	0.463

Table 6: Statistical evaluation of indicators for AOII (based on modified Copernicus Sentinel data 2017, 2018)

AOI2		01.07.2017	20.08.2017	19.09.2017	17.01.2018	11.07.2018	29.10.2018
NRI (AFFECTED)	Mean	0.424	0.178	0.212	0.270	0.190	0.289
	Median	0.442	0.124	0.150	0.219	0.132	0.246
	Max	0.698	0.530	0.578	0.652	0.586	0.675
	Min	0.099	0.079	0.080	0.080	0.078	0.081
	Sum	78.894	33.064	39.505	50.202	35.374	53.698
	5% Percentile	0.171	0.100	0.100	0.101	0.100	0.107
	95% Percentile	0.662	0.461	0.511	0.596	0.516	0.612
NRI (UNAFFECTED)	Mean	0.288	0.229	0.271	0.312	0.430	0.428
	Median	0.234	0.175	0.220	0.252	0.477	0.485
	Max	0.696	0.669	0.686	0.695	0.689	0.700
	Min	0.033	0.045	0.048	0.053	0.051	0.057
	Sum	63.040	50.075	59.373	68.413	94.120	93.678
	5% Percentile	0.084	0.096	0.097	0.100	0.100	0.100
	95% Percentile	0.620	0.552	0.601	0.659	0.672	0.688
NDVI (AFFECTED)	Mean	0.338	0.127	0.151	0.223	0.189	0.261
	Median	0.347	0.110	0.135	0.194	0.178	0.247
	Max	0.512	0.329	0.363	0.494	0.398	0.504
	Min	0.026	0.004	0.012	-0.004	0.005	0.012
	Sum	62.827	23.550	28.103	41.417	35.243	48.636
	5% Percentile	0.142	0.032	0.043	0.043	0.081	0.115
	95% Percentile	0.465	0.289	0.319	0.461	0.355	0.448
NDVI (UNAFFECTED)	Mean	0.228	0.184	0.203	0.309	0.225	0.290
	Median	0.268	0.214	0.233	0.390	0.272	0.358
	Max	0.478	0.412	0.454	0.586	0.487	0.572
	Min	-0.110	-0.207	-0.201	-0.377	-0.510	-0.588
	Sum	50.035	40.197	44.458	67.650	49.276	63.599
	5% Percentile	-0.051	-0.047	-0.037	-0.052	-0.060	-0.048
	95% Percentile	0.432	0.358	0.398	0.532	0.453	0.519
NBR (AFFECTED)	Mean	0.197	-0.028	-0.027	0.088	0.013	0.085
	Median	0.195	-0.018	-0.017	0.073	-0.012	0.059
	Max	0.426	0.266	0.313	0.512	0.284	0.449
	Min	0.026	-0.292	-0.318	-0.254	-0.153	-0.108
	Sum	36.597	-5.203	-5.026	16.350	2.438	15.802
	5% Percentile	0.058	-0.255	-0.282	-0.217	-0.132	-0.084
	95% Percentile	0.352	0.205	0.246	0.414	0.211	0.351
NBR (UNAFFECTED)	Mean	0.111	0.130	0.147	0.288	0.137	0.220
	Median	0.117	0.123	0.136	0.299	0.123	0.210
	Max	0.377	0.405	0.502	0.665	0.456	0.728
	Min	-0.117	-0.073	-0.090	-0.131	-0.081	-0.073
	Sum	24.352	28.434	32.239	63.007	29.943	48.197
	5% Percentile	-0.074	-0.010	-0.012	-0.030	-0.020	-0.004
	95% Percentile	0.296	0.317	0.373	0.538	0.350	0.504

Table 7: Statistical evaluation of indicators for AOI2 (based on modified Copernicus Sentinel data 2017, 2018)